COMPRESSIBLE TURBULENCE MEASUREMENT IN LOW-ANGLE INJECTION INTO A SUPERSONIC FLOW

THESIS
Gregory Joseph McCann
Captain, USAF

AFIT/GAE/ENY/95M

19950503 130

The views expressed in this thesis are those of the author and do not reflect the official policy or position of the Department of Defense or the U.S. Government.

Accesion For		
NTIS CRA&I		☒
DTIC TAB		☐
Unannounced		☐
Justification		
By		
Dist ibution /		
Availability Codes		
Dist	Avail and / or Special	
A-1		

COMPRESSIBLE TURBULENCE MEASUREMENTS
IN LOW-ANGLE INJECTION INTO A SUPERSONIC FLOW

THESIS

Presented to the Faculty of the School of Engineering
of the Air Force Institute of Technology
Air University
In Partial Fulfillment of the
Requirements for the Degree of
Master of Science in Aeronautical Engineering

Gregory Joseph McCann, B.S.
Captain, USAF

March 1995

Acknowledgments

First, I would like to thank my thesis advisor, Dr. Rodney Bowersox, for his unending enthusiasm and support for this research.

I would also like to thank Maj. John Doty and Lt.Col. Jerry Bowman for their excellent instruction, demand for excellence, and extreme patience with questions both academic and otherwise.

A million thanks are due Jennifer Wedekind for her guidance through the rocky shoals of part-time student status.

Thank you, Lisa, for your love and understanding.

Most of all, I would like to thank my parents for their love and support and their emphasis on a good education.

<div align="right">Gregory Joseph McCann</div>

Table of Contents

List of Figures

Multiple Overheat

List of Tables

List of Symbols

a, b	Hot-wire calibration constants
d	Injector exit diameter
f, g	Hot-wire sensitivities
k	Thermal conductivities
M	Local Mach number
Nu	Nusselt number
P, p	Pressure
Pr	Prandtl number
PR	Pressure ratio
q	Heat flux
Re	Reynolds number
T	Temperature
u, v, w	Velocity components
x, y, z	Cartesian coordinates
α, β	Hot-wire functions of Mach number
β	Injector yaw angle
γ	Ratio of specific heats
δ	Boundary layer thickness
θ	Injection angle
μ	Viscosity
ρ	Local density
ϕ	Hot-wire incidence angle
τ	Shear stress

Subscripts

e	Effective
eb	Effective back (pressure)
c	Cone-static

j	Jet
n	Normal component
s	Static
T	Turbulent
t	Total condition or tangential component
w	Wire or wall
0	Reference condition
1	Property upstream of normal shock
2	Property downstream of normal shock
∞	Freestream property

Superscripts

T	Turbulent
$()'$	Fluctuating component
$\overline{()}$	Mean component

Abstract

Mean flow and compressible turbulence measurements have been obtained at two stations downstream of low-angle supersonic injection into a Mach 3.0 flow (Re/m = 15 × 10^6). Data were collected using conventional Pitot and cone-static probes, single and multiple overheat cross-wire anemometry, and flow visualization techniques (shadowgraphs and schlierens). A direct measure of total Reynolds shear stress was accomplished using a turbulence transformation of the Reynolds-averaged Navier-Stokes equations. Results show compressibility effects, indicated by density fluctuations, to be large relative to the velocity fluctuations and on the same order in all three components. Compressibility appears to account for as much as 75% of the total Reynolds shear. The results of the present study suggest turbulent compressibility effects are very important for this class of flows.

Compressible Turbulence Measurement in Low-Angle Injection into a Supersonic Flow

I. Background

1.1 Introduction

One of the linchpins of the once (and future?) National AeroSpace Plane is its supersonic combustion ramjet (SCRAMjet) engines. These engines require fuel to be injected into a supersonic flow, rapidly mixed, and burned. Because of the expense and difficulty in operating such an engine, accurate computer models of the engine and associated flow physics are required to optimize the design.

Some types of high-energy gas lasers contain flowfields similar to that of a SCRAMjet engine. One such laser is the chemical oxygen-iodine laser (COIL) being developed as the heart of the Airborne Laser (ABL) theater missile defense platform under development by the Air Force.

Whether a SCRAMjet engine or a high-power gas laser, the complex flowfield within these devices must be understood for the concepts to reach fruition. Building models and mockups and testing them in wind tunnels is time consuming, expensive, and, for the extreme temperature cases, not feasible. Thus, researchers and engineers are relying more heavily on computational techniques to develop and optimize these concepts. However, these techniques are hindered by inaccurate turbulence models which require accurate compressible turbulence data for verification and improvement. Presently, accurate compressible turbulence data is scarce.

1.2 Requirements for Turbulence Modeling

Large supersonic, high temperature wind tunnels are expensive and have, in the last

thirty years, become more scarce. Since 1963, fully two-thirds of these types of wind tunnels have been dismantled or abandoned.[1] At the same time, the cost of computing power has decreased several orders of magnitude. But computers are not a panacea. Computers, it should be noted, do exactly what they are programmed to do: a code that executes successfully does not necessarily produce accurate answers.

In the field of high speed turbulence modeling, the complete solution of the unsteady Navier-Stokes equations is the ultimate goal. Today's computers, though powerful, still lack the speed and memory required for such a complete solution. Although estimates vary, it is commonly held that 10 grid points are necessary for adequate resolution of the motion of a turbulent eddy.[2] The relative size of large scale and small scale flow structures is commonly given by[3]

$$\frac{Large\ scale}{Small\ scale} \sim Re_\delta^{3/4} \tag{1.1}$$

For the current work, $Re/m = 15 \times 10^6$ and $\delta \approx 1$ cm $\therefore Re_\delta = 15 \times 10^4$. The ratio between size of large and small scale structures for the present work is 7600:1. This would require approximately 76,000 points across the boundary layer and $(76,000)^3$ points for 1 cm^3 of flow. This enormous grid requirement must be coupled with an equally challenging temporal resolution. It is unlikely the direct numerical simulation of a high Reynolds number, compressible, turbulent flow field will yield completely to computational methods in the near future.

Engineering efforts in the near term will have to focus on accurate modeling of the small-scale compressible turbulence. The two primary avenues to this end are the Reynolds (time)-averaged Navier-Stokes equations (RANS) and the Favre (mass-weighted)-averaged Navier-Stokes equations (FANS) (both will be discussed further in Chapter 2). Both methods require closure formulations.

The development of the needed closure formulations (turbulence models) rely heavily on both experimental data and physical intuition. The lack of compressible turbulence data[4] has lead to direct extensions of incompressible models and sometimes ad-hoc assumptions. These extensions and assumptions have generally shown to be invalid for

compressible flows.[5] The availability of experimental data has been hampered by the expense and difficulty of measuring the compressible components of the turbulence. In addition, it is necessary to employ experimental methods which can measure the needed compressible terms in the Navier-Stokes equations and to report the data in a form applicable to both theoretical and computational efforts. These issues have been addressed by Bowersox[6] and are employed in the present work.

1.3 Scope of Present Study

The present study seeks to expand upon the current understanding of mixing and turbulence in a low-angle supersonic injection into a supersonic flow. A simple injection model, based on parameters of similar experiments in the literature[7,8,9], is employed. Mean flow and single overheat cross-wire anemometry is taken at two downstream locations to provide data which will lead to a more accurate determination of relative importance of the terms in the RANS. Multiple overheat cross-wire anemometry is taken at a single location to validate assumptions made in the taking of single overheat data. The ultimate aim of the present work is to provide data which will aid the validation of CFD codes, improve compressible turbulence modeling, and enhance the understanding of the associated flow physics.

II. Mathematical Development

This chapter presents the development of the forms of the unsteady Navier-Stokes equations utilized in the present work. As stated in Chapter 1, the two most common forms implemented are the Reynolds (time)-averaged (RANS) and the Favre (mass-weighted)-averaged Navier-Stokes (FANS) equations.

2.1 Compressible Navier-Stokes Equations

The full unsteady, compressible Navier-Stokes equations[2] are presented below as a prelude the development of the RANS and FANS:

$$\frac{\partial \rho}{\partial t} + \frac{\partial}{\partial x_j}\left(\rho\, u_j\right) = 0 \tag{2.1}$$

$$\frac{\partial}{\partial t}(\rho\, u_i) + \frac{\partial}{\partial x_j}(\rho\, u_i\, u_i) = -\frac{\partial P}{\partial x_i} + \frac{\partial}{\partial x_j}(\tau_{ij}) \tag{2.2}$$

$$\frac{\partial}{\partial t}(\rho\, h_0) + \frac{\partial}{\partial x_j}(\rho\, u_j\, h_0) = \frac{\partial P}{\partial t} + \frac{\partial}{\partial x_j}(u\,\tau_{ij} - q_j) \tag{2.3}$$

where

$$h_0 = h + \frac{1}{2} u_i\, u_i \tag{2.4}$$

$$\tau_{ij} = \mu\left(\frac{\partial u_i}{\partial x_j} + \frac{\partial u_j}{\partial x_i}\right) + \delta_{ij}\,\lambda\,\frac{\partial u_k}{\partial x_k} \tag{2.5}$$

$$q_j = -k\,\frac{\partial T}{\partial x_j} \tag{2.6}$$

4

$$\lambda = -\frac{2}{3}\mu \quad (\textit{bulk viscosity}) \tag{2.7}$$

As stated in Chapter 1, numerical solutions to the above equations are not available at this time, therefore approximate methods must be utilized. Time averaging of the above equations leads to the RANS equations.

2.2 Reynolds-Averaged Navier-Stokes (RANS) Equations

A standard method of dealing with turbulent flows is to separate the instantaneous flow properties into mean and fluctuating components. The instantaneous flow properties become:

$$
\begin{array}{ll}
u_i = \bar{u}_i + u_i' & h_0 = \bar{h}_0 + h_0' \\
P = \bar{P} + P' & q_i = \bar{q}_i + q_i' \\
\rho = \bar{\rho} + \rho' & \tau_{ij} = \bar{\tau}_{ij} + \tau_{ij}'
\end{array}
\tag{2.8}
$$

The barred quantities are time averaged over a period longer than the longest fluctuation but shorter than any unsteadiness of the mean flow. The prime quantities are the deviations from the average.[10] The flow variables are time averaged according to

$$\bar{u} = \int_0^{t_0 + T} u(x, y, z, t)\, dt \tag{2.9}$$

By substituting the mean and fluctuating components (2.7) into the governing equations (2.1)-(2.3) and employing (2.9), the RANS equations are developed

$$\frac{\partial \bar{\rho}}{\partial t} + \frac{\partial}{\partial x_j}(\bar{\rho}\, \bar{u}_j + \overline{\rho' u_j'}) = 0 \tag{2.10}$$

5

$$\frac{\partial}{\partial t}(\overline{\rho}\,\overline{u}_j + \overline{\rho'u_j'}) + \frac{\partial}{\partial x_j}(\overline{\rho}\,\overline{u}_i\,\overline{u}_j) = -\frac{\partial \overline{P}}{\partial x_i} + \frac{\partial}{\partial x_j}(\tau_{ij} + \tau_{ij}^T) \qquad (2.11)$$

$$\frac{\partial}{\partial t}(\overline{\rho}\,\overline{e}_0 + \overline{\rho'h_0'}) + \frac{\partial}{\partial x_j}(\overline{\rho}\,\overline{h}_0\,\overline{u}_j) = -\frac{\partial}{\partial x_j}(\overline{u}_i\,\tau_{ij} + \overline{u_i'\tau_{ij}'} - q_j - q_j^T) \qquad (2.12)$$

The compressible terms in (2.10)-(2.12) can be written as

$$m_i^T = -\overline{\rho'u_i'} \qquad (2.13)$$

$$\tau_{ij}^T = -\overline{\rho}\,\overline{u_i'u_j'} - \overline{u}_i\,\overline{\rho'u_j'} - \overline{u}_j\,\overline{\rho'u_i'} - \overline{\rho'u_i'u_j'} \qquad (2.14)$$

$$q_i^T = -\overline{\rho}\,\overline{h_0'u_i'} + \overline{h}_0\,\overline{\rho'u_i'} + \overline{u}_i\,\overline{\rho'h_0'} + \overline{\rho'h_0'u_i'} \qquad (2.15)$$

where m^T is the turbulent apparent mass, τ^T is the turbulent compressible shear, and q^T is the turbulent compressible heat flux. The averaging process is notable in that it removes some flow information, in particular, its frequency, phase, and wavelength.

In incompressible flow, the apparent mass and the last three terms of both (2.14) and (2.15) are identically zero. In compressible flows, the last term of both (2.14) and (2.15) is a triple correlation and therefore assumed small and negligible. The second and third terms are significant, however, and their exclusion in incompressible extensions has led to the latter's failure to fully model the physics of compressible turbulence.

2.3 Favre-Averaged Navier-Stokes Equations

The second averaging method is the Favre-averaged (mass-weighted) Navier-Stokes equations. A thorough treatise on the development of the FANS can be found in Schetz.[11]

6

Like the RANS, FANS eliminates some flow information in addition to the phase, frequency, and wavelength, in this case, the explicit moments of the density fluctuation. The FANS has been applied to compressible flows, using extensions of incompressible turbulence models, with some success with wall shear layers, but generally with failure with free shear layers. The flow conditions in the present work include both wall shear and free shear, but with emphasis on the free shear.

2.4 Turbulence Transformation

As previously stated, different formulations of the Navier-Stokes equations lend themselves to different purposes. Thus, right-hand sides of equations (2.13)-(2.15) must be transformed into experimentally measurable terms. The turbulence transformation below follows from that developed by Bowersox.[12]

The following identity begins the transformation

$$\rho \phi = (\overline{\rho \phi}) + (\rho \phi)' \tag{2.16}$$

$$\rho \phi = (\overline{\rho} + \rho')(\overline{\phi} + \phi') \tag{2.17}$$

where ϕ is a generic variable. Setting the right-hand sides of (2.16) and (2.17) equal yields

$$\overline{\rho \phi} + (\rho \phi)' = (\overline{\rho} + \rho')(\overline{\phi} + \phi') \tag{2.18}$$

Time averaging (2.17) yields

$$\overline{\rho \phi} = \overline{\rho} \, \overline{\phi} + \overline{\rho' \phi'} \tag{2.19}$$

which is also a preliminary step in the FANS development. Subtracting (2.19) from (2.18) produces the fluctuation relation

$$(\rho \phi)' = \overline{\rho} \phi' + \overline{\phi} \rho' + \left(\rho' \phi' - \overline{\rho' \phi'}\right). \tag{2.20}$$

Substituting $\phi = u_i$ and $\phi = u_j$ into (2.20) and forming the products $(\rho u_i)'$ and $(\rho u_j)'$ one can collect the terms in the Reynolds shear (2.14) on one side of the equation to produce the

7

Reynolds shear transformation

$$\tau_{ij}^T = -\frac{\overline{(\rho\, u_i)'\,(\rho\, u_j)'}}{\overline{\rho}} + \overline{\rho}\,\overline{u}_i\,\overline{u}_j \overline{\left(\frac{\rho'}{\overline{\rho}}\right)^2}, \tag{2.21}$$

where the triple correlation $\overline{\rho'\,u_i'\,u_j'}$ and fourth order terms have been neglected. Similarly, the Reynolds heat flux terms can be shown to be

$$q_i^T = \overline{(\rho\, u_i)'\,h_0'} + \overline{h}_0\,\overline{\rho'\,u_i'} \tag{2.22}$$

All the terms appearing in (2.21) and (2.22) can be measured directly or estimated by separation of cross-wire variables. Chapter 4 contains a more detailed description of the process.

III. Facilities and Instrumentation

This chapter identifies the facilities and instrumentation utilized in the present study. The AFIT Mach 3 wind tunnel and injector model will be considered as will the flow visualization techniques and equipment. Data acquisition and instrumentation for both mean flow and turbulence (hot-wire) will also be covered.

3.1 Supersonic Wind Tunnel

The present experimental work was accomplished in the AFIT Mach 3 wind tunnel. The wind tunnel has a 6.35 cm x 6.35 cm test section and operates with a combination of pressure and vacuum. The tunnel has a replaceable Mach 3.0 nozzle section and a variable diffuser. The pressure side of the tunnel is a 0.69 MPa house air supply provided by two Atlas Copco GAU 807 compressors delivering 0.5 kg/sec. Two Pioneer Refrigerant Air Dryers dry the house air supply. The air is further dried and cleaned prior to its introduction into the tunnel via a cyclone separator and multiple layers of a cloth fiber filter paper.

The vacuum side of the wind tunnel is provided by sixteen storage tanks (~ 16 m^3 total volume) evacuated by three 7.5 hp, 230 V Stokes MicroVac pumps. This arrangement could provide a vacuum of approximately 2 mmHg, but runs were typically made at around 10 mmHg. The wind tunnel had a useful run time of approximately 20-25 seconds.

The tunnel settling chamber contains a multi-screen flow straightener with a thermocouple and Pitot probe downstream just prior to the convergent portion of the nozzle to account for any pressure drop across the straightener. An Endevco 0-690 kPag pressure transducer monitored chamber stagnation pressure through the Pitot probe. The thermocouple was used to measure total temperature of the flow. An Omega Engineering Type K (chromel-alumel) constructed of Type 316 stainless steel was employed.

3.2 Injector Model

As stated in Chapter 1, the purpose of the present study was to obtain three-dimensional turbulence for a supersonic, low angle flow injected into a supersonic
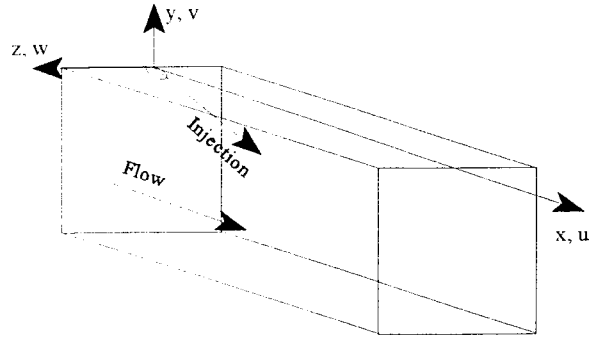
FIGURE 3.1: Tunnel Coordinates

freestream (see Figure 3.1).

3.2.1 Injector Model Considerations

There are several critical parameters to be considered for the injection model: injection angle, yaw angle, effective back pressure, and injector Mach number. For the present study, the injector parameters were also scaled to be compatible with existing equipment:

injection angle (θ)	25°
yaw angle (β)	0°
effective back pressure ratio (P_j/P_{eb})	3.25
injector Mach number (M_j)	1.8

3.2.2 Injector Model Design

The injector (Figure 3.2) was designed with ease of construction in mind. The upper portion of the air inlet is threaded to accept a 6.35 mm (inner diameter) pipe and expands conically to 19.05 mm diameter. The settling chamber is a 19.05 mm diameter spherical bottom cavity. A hole was tapped into the side of the settling chamber to accept an Endevco 0-690 kPag
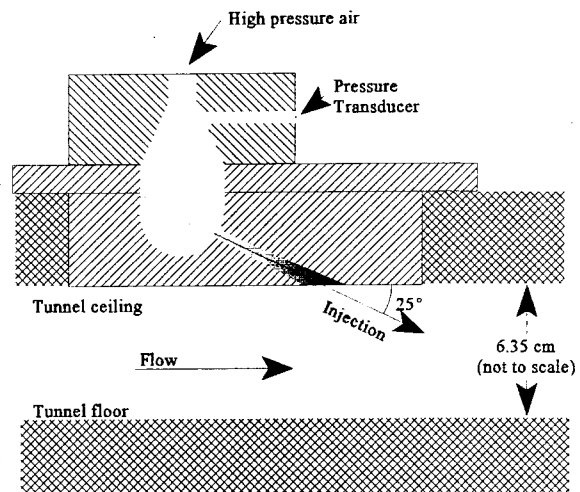
FIGURE 3.2: Injector Model

10

chamber to accept an Endevco 0-690 kPag pressure transducer. The lower portion of the injector block was machined to be perfectly flush with the ceiling of the test section to reduce edge shocks. The injector is conical with a throat diameter of 3.264 mm and an effective exit diameter (d) of 3.861 mm. The dimensions of the injector exit are 4.0 mm × 9.5 mm.

3.2.3 Effective Back Pressure

The concept of "effective back pressure"(P_{eb}) was first put forth by Schetz and Billig.[13] The initial model was based on treating the normally injected supersonic stream as a cylindrical object in the freestream. The P_{eb} was one-half the stagnation pressure on the surface of the cylinder based on the freestream conditions. A later work by Billig, et al.[14] set P_{eb} at two-thirds the freestream Pitot pressure. Additional work set P_{eb} equal to 80% of the static pressure behind a normal shock in the freestream.[15,16] There is little difference in the P_{eb} obtained for these different methods. More recent works[17,18] extended the models to angled injection (as opposed to the transverse injection of earlier works).

The new model assumes the low angle jet to behave like a cone whose half angle is the angle of the jet where P_{eb} becomes the surface pressure on the cone. Conical shock charts[19] indicate that for M=2.9 and θ=25°, the surface pressure coefficient

$$\frac{p_c - p_{sl}}{q_1} = 0.42 \tag{3.1}$$

where p_c is the surface pressure of the cone (therefore P_{eb}), p_{sl} is the freestream static pressure, and q_1 is the freestream dynamic pressure. Thus,

$$P_{eb} = \left(0.42 \frac{q_1}{p_{tl}} + \frac{p_{sl}}{p_{tl}} \right) p_{tl}. \tag{3.2}$$

To obtain the 3.25 pressure ratio, the static pressure of the jet must be 3.25 times P_{eb}. The pressure ratio (PR) becomes a function of tunnel stagnation pressure and injector stagnation pressure given by

11

$$PR = 1.68 \frac{p_{tj}}{p_{tl}} \, .$$

(3.3)

For the present study, $p_{tj} = 386$ kPa and $p_{tl} = 200$ kPa.

3.3 Data Acquisition Locations

Both mean flow and hot-wire data was acquired at two downstream locations in the wind tunnel: 20 and 40 jet exit diameters (x/d) downstream of the *upstream* edge of the injector nozzle.

3.3.1 Mean Flow Data

Mean flow data was taken at 11 cross-stream positions: z/d = -5...0...+5. At each z/d position (referred to from here on as stations), two vertical runs had to be made because of limited run-time, traverse speed, and speed limitations for accurate probe response. Each run covered 2.54 cm of the flow field, from y = -0.16 to -2.70 cm on the first run and from y = -2.70 to -5.24 cm on the second. This covered approximately 13 y/d stations. See Figure 3.3.
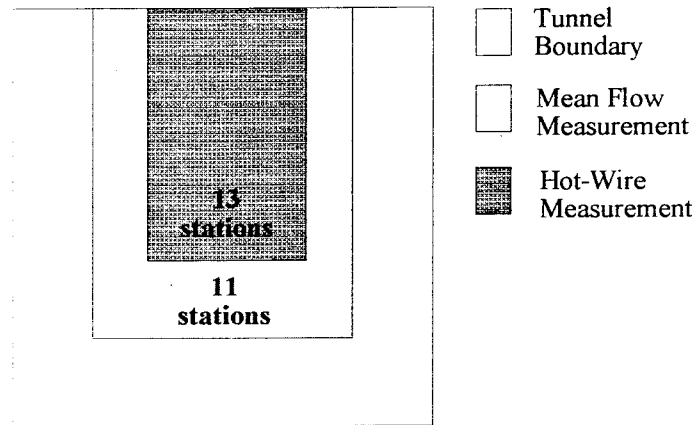
FIGURE 3.3: Data Acquisition Areas

12

3.3.2 Hot-Wire Data

Single overheat hot-wire data was taken at 13 cross-stream stations from z/d = -3...0...+3 at every half station. This was done to increase the resolution in the region around the core injector flow. A single vertical profile from y = -0.16 to -3.97 cm (10 y/d stations) was made. Multiple overheat data was taken only at the center (z/d = 0) downstream station (x/d = 40).

3.4 Flow Visualization

Both 600 nsec spark schlieren and shadowgraph photography were utilized for flow visualization.

3.4.1 Shadowgraph Setup

Shadowgraphs were taken of the entire flowfield encompassing the injector and both downstream measuring stations. The light source was a Cordin Model 5401 arc light, providing a 600 nanosecond spark. Powering the spark lamp was a Cordin Model 5205 power supply set at approximately 5000 V DC for both schlieren and shadowgraph photography. A mirror with a 100 cm focal length was used to collimate the light and pass it through the test section. All photographs were taken with Type 52 Polaroid film.

3.4.2 Schlieren Setup

The schlieren setup was essentially the same as the shadowgraph setup but with the addition of another 100 cm focal length mirror which was used to refocus the collimated beam and pass it through the knife edge.

3.5 Mean Flow Instrumentation

The wind tunnel was manually operated by first opening the valve to the vacuum tanks then the valve to the high pressure air supply. The tunnel was shut down in the reverse order. Tunnel run time was limited primarily by the available vacuum to 20-25 seconds.

3.5.1 Settling Chamber

The total pressure in the settling chamber was held constant at roughly 203 ± 4 kPa for all runs and was recorded on the data acquisition system (DAS). An Endevco 0-690 kPag pressure transducer supplied the pressure signal which was also used as the DAS trigger. A mechanical pressure regulation system, consisting of a Fairchild pneumatic pressure regulator and a Leslie pressure reducing valve, kept the tunnel pressure constant during the run (±4 kPa).

As indicated previously, total temperature was monitored by an Omega Engineering thermocouple. The temperature was not recorded during the run because it did not vary substantially during the run (298 ±3 K).

3.5.2 Traverse and LVDT System

The traverse was comprised of an Arrick Robotics MD-2 dual stepper motor driver package and a Size 23 Stepper Motor. The stepper motor was used to move the various probes through a vertical station in the flow. Translation across the flow was performed manually by a mechanical screw/slide assembly holding the stepper motor. Maximum speed of the stepper motor was 0.254 cm/sec. The position of the traverse was monitored by a TransTek Inc. Model 0217 linear voltage displacement transducer (LVDT) and recorded by the DAS.

3.5.3 Data Acquisition System

Mean flow data (tunnel stagnation pressure, traverse position, and probe pressure) were recorded by a Nicolet MultiPro 120 Digitizer[20] at a 200 Hz sampling rate.

3.5.4 Filters and Signal Conditioners

All mean flow signals were conditioned, filtered, and amplified prior to acquisition by the DAS. Signals from pressure transducers were fed to Endevco Model 4423 Signal Conditioners which supplied excitation voltage to the transducers, filtered the signal, and amplified it. LVDT signals were passed through a TransTek Model 1000-0012 oscillator/demodulator.

3.5.5 Downstream Pressure Probes

Mean flow parameters were measured using a conventional Pitot probe and a 10° half-angle cone-static probe. The Pitot probe was constructed of a 1.59 mm outer diameter stainless steel tube inserted into a 3.175 mm stainless steel tube for reinforcement. An Endevco 0-103 kPag transducer recorded both Pitot pressure and cone-static pressure.

The cone-static probe consisted of a 10° semivertex angle axisymmetric cone. The cone tip was machined from stainless steel with four 0.34 mm (#80 drill) pressure taps at 90° intervals around the circumference and 4.3 mm from the tip. The four pressure taps met in a common chamber where they were averaged to account for misalignment errors of up to 7°.[21] The cone was soldered to 1:59 mm tubing inserted into a 3.175 mm sleeve similar to the Pitot probe. The pressure taps in the cone-static probe and the opening in the Pitot probe were equidistant from the probe support centerline.

3.6 Hot-Wire Instrumentation

Data acquisition for the hot-wire data was almost identical to that of the mean flow data with the substitution of two hot-wire channels for the downstream pressure probe.

3.6.1 Nicolet Configuration

A total of four channels of data were acquired in the hot-wire runs: total pressure, LVDT, and two hot-wire channels. Total pressure and hot-wire channels were acquired at 10 kHz. 10 kHz was deemed sufficient to capture the energy of the turbulent flow. The probe wires were tuned to provide 100-150 kHz frequency response.[22]

3.6.2 Cross-Wire Probes

For the present work, TSI Inc. Model 1243-20 platinum hot film probes were used.[22] Each wire had a length of 1 mm and a diameter of 51 μm, with a coefficient of resistance of 0.24%/°C at 20°C. The coefficient was assumed constant for the range of temperature encountered. Model 1243-20 probes were used to acquire "uv" data and Model 1243AN-20 probes were used to acquire "uw" data. The probes were identical except for their wire orientation.

15

3.6.3 Anemometer

A TSI Inc. IFA 100 System Intelligent Flow Analyzer, constant temperature anemometer was employed for the present study. The IFA 100 contained a Model 150 anemometer and a Model 157 Signal Conditioner, and transducers for each hot-wire channel all housed in the Model 158 master cabinet. The IFA 100 symmetrical bridge had a top resistance of 50 Ω (R_s) and allowed for an external bridge arm which was used to set the overheat ratio. All resistance measurements were taken with a Hewlett-Packard 3468A digital multimeter using the four-wire method. For single overheat data, the external resistance was set so the overheat ratio was 2.03±0.04. For multiple overheat data, the external resistance was varied based on the resistance the individual wire according to the following:

Overheat Number	Overheat Ratio
1	1.25
2	1.35
3	1.50
4	1.60
5	1.75
6	1.85
7	1.95
8	2.10

For each overheat ratio, a data run and a calibration run was made. While some fidelity in matching pressures from run to run is lost, great gains are made in spatial resolution over the overheat scanning circuit method of Bowersox.[12]

3.7 Computational Facilities

Data acquisition was accomplished with both a Zenith 486 and a Compaq 386 PC. Traverse operation was performed by a Zenith 286 and a Compaq 386 PC (computers were upgraded during the test sequence). Data reduction was performed on 486 PCS and AFIT's Sun Sparc 20 work stations. Two-dimensional plots were generated with Grapher for Windows and contour plots were generated with Mathcad 5.0+.

16

IV. Data Reduction Techniques

This chapter describes the data reduction techniques for both the mean flow and hot-wire (both single and multiple overheat) data.

4.1 Mean Flow

All mean flow data were combined to obtain flowfield Mach number. For each run, total temperature (T_{t1}), tunnel stagnation pressure (p_{t1}), and Pitot pressure (p_{t2}) or cone-static pressure (p_c) was recorded. The Mach number can be calculated by the ratio of cone-static to Pitot pressure in the freestream. This ratio as a function of Mach number for the $10°$ cone was determine by a least-square fit by Bowersox:[6]

$$\frac{1}{M} = -0.052976 + 4.6840\,x - 18.6786\,x^2 + 50.7006\,x^3 - 54.1577\,x^4 \qquad (4.1)$$

where $x = p_c/p_{t2}$. Equation (4.1) is valid for Mach numbers between 1.5 and 4.4 with a standard deviation of 0.06%.

4.2 Turbulent Flow

The data reduction methods for the fluctuating component of the flowfield is considerably more difficult than the mean flow component. This section outlines the data reduction methods used for both single and multiple overheat cross-wire anemometry.

4.2.1 General Theory

For turbulent compressible flow, the Nusselt number of a cylinder (ie hot-film probe) has the following functional relationship[23]

$$Nu = Nu(L/d, M, Pr, Re_c, \tau) \qquad (4.2)$$

where L/d is the wire aspect ration, M is the Mach number, Pr is the Prandtl number, Re_c is

the effective Reynolds number based on wire diameter, and τ is the temperature loading factor $[\tau = (T_w - T_e) / T_t]$. T_w is the wire temperature and T_e is the equilibrium temperature the wire would obtain if placed unheated in the flow. Eqn. (4.2) reduces to

$$Nu = Nu(Re_e, \tau).$$

(4.3)

for the following conditions: high Reynolds number (Re > 20), constant Prandtl number flows where the Mach number normal to the wire is greater than approximately 1.2, and where the wire aspect ratio is large (L/d >> 1).[23] For wires normal to the flow, hot-wire data has been found to collapse onto the following curve

$$Nu = a \sqrt{Re} + b$$

(4.4)

When using (4.4), the hot-wire must be calibrated at each wire temperature.

The Nusselt number is also proportional to the power supplied to the wire (q_w)

$$Nu = \frac{q_w}{\pi k_t L (T_w - T_e)}$$

(4.5)

where $q_w = i_w^2 R_w$ and $i_w = V_w / (R_w + R_s + R_L)$ (i_w=wire current, R_w=wire resistance, V_w=wire voltage). The Nusselt number can then be expressed as the following, if T_e is assumed to be T_t in both the calibration and data reduction process

$$Nu = \frac{V_w^2 R_w}{(R_w + R_s + R_L)^2} \frac{1}{\pi k_t L (T_w - T_e)}$$

(4.6)

To arrive at the appropriate mean and fluctuating equations, the voltage, Reynolds number, and total temperature are replaced by their mean and fluctuating components, apply the binomial theorem, and noting

$$\frac{\overline{V_w}^2}{C_0} = \left(\frac{\overline{T_t}}{T_0} \right)^{n_k} \left[a \sqrt{\overline{Re_e}} + b \right] \left(T_w - \overline{T_t} \right)$$

(4.7)

18

where

$$C_0 = \frac{(R_w + R_s + R_L)^2}{R_w} \pi L k_0$$ (4.8)

and $n_k = 0.89$. The detailed procedure to derive (4.7) is presented in Bowersox.[24] Solving for $v_w' / \overline{V}_w$ yields

$$\frac{v_w'}{\overline{V}_w} = f\left(\frac{Re\, o_e'}{\overline{Re\, o_e}}\right) + g\left(\frac{T_t'}{\overline{T}_t}\right)$$ (4.9)

where the hot-wire sensitivities (f and g) are given as the following

$$f = \frac{1}{4}\left(1 + \frac{b}{a\sqrt{\overline{Re}_e}}\right)^{-1} \quad \text{and} \quad g = \frac{-\overline{T_t'}}{2(\overline{T}_w - \overline{T}_t)} + \frac{n_k}{2} - f n_\mu$$ (4.10)

From (4.10), it is clear that $\sqrt{\overline{Re}_e}$ and $\overline{T}_t$ must be known in order to evaluate the hot-wire sensitivities. Equation (4.7) can be rewritten as

$$\sqrt{\overline{Re}_e} + x_i \overline{T}_t \sqrt{\overline{Re}_e} + y_i \overline{T}_t = z_i$$ (4.11)

where $x_i = -1 / T_{wi}$, $y_i = -b_i / (a_i T_{wi})$, and $z_i = \overline{V}_{wi}^2 / (C_i a_i T_{wi}) - b_i / a_i$. Within (4.11), i is the overheat number and C is C_0 where k_0 is replaced with k_r. As a minimum, two overheat ratios are necessary to determine the two unknowns $\sqrt{\overline{Re}_e}$ and $\overline{T}_t$. If more than three overheat ratios are used, then a least squares analysis can be used to obtain $\sqrt{\overline{Re}_e}$ and $\overline{T}_t$.

Squaring then averaging Eqn. (4.9) yields the following hot-wire fluctuation equation

$$f_i^2 \overline{\left(\frac{Re\, o_e'}{\overline{Re\, o_e}}\right)^2} + 2 f_i g_i \overline{\left(\frac{Re\, o_e' T_t'}{\overline{Re\, o_e} \overline{T}_t}\right)} + g_i^2 \overline{\left(\frac{T_t'}{\overline{T}_t}\right)^2} = \overline{\left(\frac{v_w'}{\overline{V}_w}\right)^2}_i$$ (4.12)

The general least square (GLS) method yields the following 3×3 system, where i again

19

denotes the overheat number and where the summations are over N, the number of overheat ratios used,

$$
\begin{bmatrix}
\Sigma f_i^4 & 2\Sigma f_i^3 g_i & \Sigma f_i^2 g_i^2 \\
\Sigma f_i^3 g_i & 2\Sigma f_i^2 g_i^2 & \Sigma f_i g_i^3 \\
\Sigma f_i^2 g_i^2 & 2\Sigma f_i g_i^3 & \Sigma g_i^4
\end{bmatrix}
\begin{pmatrix}
\overline{\left(\dfrac{Re\,o_e{}'}{\overline{Re\,o_e}}\right)^2} \\[2ex]
\overline{\left(\dfrac{Re\,o_e{}'}{\overline{Re\,o_e}}\dfrac{T_t{}'}{\overline{T_t}}\right)} \\[2ex]
\overline{\left(\dfrac{T_t{}'}{\overline{T_t}}\right)^2}
\end{pmatrix}
=
\begin{pmatrix}
\Sigma f_i^2 \overline{\left(\dfrac{v_w{}'}{\overline{V_w}}\right)^2}_i \\[2ex]
\Sigma f_i g_i \overline{\left(\dfrac{v_w{}'}{\overline{V_w}}\right)^2}_i \\[2ex]
\Sigma g_i^2 \overline{\left(\dfrac{v_w{}'}{\overline{V_w}}\right)^2}_i
\end{pmatrix}
\qquad (4.13)
$$

It is important to note that, for the GLS method, any errors introduced in the experiment through scatter are amplified by a combined power of four. This inherent disadvantage of the GLS approach led to the development of a new method, the quadratic least square (QLS) method.[6]

The QLS method begins by assuming that the error in the measured hot-wire voltages are purely random and that all bias errors are contained in f and g.[24] Defining τ^* as

$$
\tau^* = \frac{\left(T_w - \overline{T_t}\right)}{\overline{T_t}}
\qquad (4.14)
$$

and rewriting the hot-wire sensitivities as

$$
f = f_0 + m_f \frac{1}{\tau^*}
$$
$$
g = g_0 + m_g \frac{1}{\tau^*}
\qquad (4.15)
$$

(4.12) can be rewritten as

20

$$\left(\overline{\dfrac{v_w'}{\bar{V}_w}}\right)^2 = a_0 + a_1\left(\dfrac{1}{\tau^*}\right) + a_2\left(\dfrac{1}{\tau^*}\right)^2 \tag{4.16}$$

where

$$\begin{bmatrix} f_0^2 & 2f_0 g_0 & g_0^2 \\ 2f_0 m_f & 2\left(f_0 m_g + g_0 m_f\right) & 2 g_0 m_g \\ m_f^2 & 2 m_f m_g & m_g^2 \end{bmatrix} \begin{pmatrix} \overline{\left(\dfrac{\overline{Re\,o_e'}}{\overline{Re\,o_e}}\right)^2} \\ \overline{\left(\dfrac{\overline{Re\,o_e'\,T_t'}}{\overline{Re\,o_e}\,\overline{T_t}}\right)} \\ \overline{\left(\dfrac{T_t'}{\overline{T_t}}\right)^2} \end{pmatrix} = \begin{pmatrix} a_0 \\ a_1 \\ a_2 \end{pmatrix} \tag{4.17}$$

A minimum or three overheat ratios are necessary to solve for the unknowns in (4.16). If more than three are used, then the QLS method can be used to evaluate the right-hand side of (4.16). The turbulence results can then be obtained by solving (4.17).

It is important to note that any error due to experimental scatter is amplified by a combined power of two. The GLS method and the QLS method yield identical results if (4.15) is valid and if the experimental scatter in the hot-wire sensitivities is purely random; the QLS method only reduces the effects of bias error in f and g.[24]

The next step is to specify Re_e for the cross-wire probe.

4.2.2 Cross-Wire

To obtain cross-wire turbulence results, Re_e must be related to the x and y tunnel coordinates. The following analysis is presented in full in Bowersox.[24]

It can be shown that

$$Re^2 = Re_n^2 + k_c^2\, Re_t^2 = A_1\, Re_x^2 + 2\, A_2\, Re_x\, Re_y + A_3\, Re_y^2 \tag{4.18}$$

where A_i are given by the following

$$A_1 = \cos^2(\phi) + k_c^2 \sin^2(\phi)$$
$$A_2 = (1 - k_c^2) \cos(\phi) \sin(\phi) \qquad (4.19)$$
$$A_3 = k_c^2 \cos^2(\phi) + \sin^2(\phi)$$

.

and ϕ is the hot-wire incidence angle.

Replacing Re_c, Re_x, and Re_t by their mean and fluctuating components, it can be shown that

$$\overline{Re\, o_{ej}} = \overline{Re\, o_x} \sqrt{B_{3j}}$$

$$\left(\frac{Re\, o_e{}'}{\overline{Re\, o_e}} \right)_j = B_{1j} \left(\frac{Re\, o_x{}'}{\overline{Re\, o_x}} \right) + B_{2j} \left(\frac{Re\, o_y{}'}{\overline{Re\, o_x}} \right) \qquad (4.20)$$

where $B_1 = A_1/B_3$, $B_2 = A_2/B_3$, $B_3 = A_1 + 2A_2R_0$, $R_0 = \overline{\rho\, v}/\overline{\rho\, u}$, and j is the wire number on the cross-wire probe. Equation (4.20) assumes $R_0^2 \ll 1$.

4.2.3 Single Overheat Ratio Technique

For many compressible flows, the total temperature fluctuations are small; T_t is essentially constant and $d(T_t) = 0$ (adiabatic flow). For adiabatic flow with $Pr = 1$, provided $T_t{}' = 0$, the following results

$$\frac{T'}{\overline{T}} = -(\gamma - 1) M^2 \left(\frac{u'}{\overline{u}} \right) \qquad (4.21)$$

But for air, $Pr \neq 1$ and $T_t{}' \neq 0$ even for flows that are adiabatic in the mean. Therefore, a correction factor can be added to account for $Pr \neq 1$ and $T_t{}' \neq 0$

$$\frac{T'}{\overline{T}} = -\kappa(\gamma - 1) M^2 \left(\frac{u'}{\overline{u}} \right) \qquad (4.22)$$

Typically, $\kappa \in [0.3, 0.5]$, but $\kappa = 1.0$ was used in this study based on the high overheat ratio used ($T_t{}' \to 0$). Defining $\theta \equiv -\kappa(\gamma-1)M^2$ and assuming $R_0^2\theta \ll 1-\theta$, then it can be shown that

$$\frac{u'}{\overline{u}} = \frac{1}{1-\theta}\left[\overline{\frac{(\rho\,u)'}{\overline{\rho\,u}}}\right] \tag{4.23}$$

and

$$\frac{v'}{\overline{u}} = \frac{(\rho\,v)'}{\overline{\rho\,u}} - R_0\frac{\rho'}{\overline{\rho}} \tag{4.24}$$

The total temperature fluctuation equation (4.27) now becomes

$$\frac{T_t'}{\overline{T_t}} = \frac{\beta + \alpha\,\theta}{1-\theta}\left[\overline{\frac{(\rho\,u)'}{\overline{\rho\,u}}}\right] \tag{4.25}$$

where $\alpha = 1.0 / [1 + 0.5(\gamma - 1)M^2]$ and $\beta = (\gamma - 1)\alpha M^2$. With the above equations (4.22)-(4.25), the single overheat cross-wire response can be approximated as

$$[S_{ij}] = \begin{pmatrix} \overline{\left(\frac{Re\,o_x'}{\overline{Re\,o_x}}\right)^2} \\[2ex] \overline{\frac{Re\,o_x'\ Re\,o_y'}{\overline{Re\,o_x}\ \overline{Re\,o_x}}} \\[2ex] \overline{\left(\frac{Re\,o_y'}{\overline{Re\,o_x}}\right)^2} \end{pmatrix} = \begin{pmatrix} \overline{\left(\frac{v_w'}{\overline{V_w}}\right)^2}_{1} \\[2ex] \overline{\left(\frac{v_w'}{\overline{V_w}}\right)^2}_{2} \\[2ex] \overline{\left(\frac{v_w'}{\overline{V_w}}\right)_{1}\left(\frac{v_w'}{\overline{V_w}}\right)_{2}} \end{pmatrix} \tag{4.26}$$

where **S** is the single overheat matrix whose coefficients are given below (note that the coefficients become greatly simplified with the assumption $R_0 \approx 0$)

$$S_{11} = f_1^2 B_{11}^2 + 2 f_1 g_1 R_{mT} B_{11} + g_1^2 R_{mT}^2$$

$$S_{12} = 2 \left[f_1^2 b_{11} B_{21} + f_1 g_1 R_{mT} \left(R_{uT} R_0 + R_{vT} B_{21} B_{11} \right) + g_1^2 R_{mT}^2 R_0 \right]$$

$$S_{13} = f_1^2 B_{21}^2 + 2 f_1 g_1 R_{mT} R_{vT} R_0 B_{21}$$

$$S_{21} = f_2^2 B_{12}^2 + 2 f_2 g_2 R_{mT} R_{uT} B_{12} + g_2^2 R_{mT}^2$$

$$S_{22} = 2 \left[f_2^2 B_{12} B_{22} + f_2 g_2 R_{mT} \left(R_{uT} R_0 B_{12} + R_{vT} B_{22} \right) + g_2^2 R_{mT}^2 R_0 \right] \qquad (4.27)$$

$$S_{23} = f_2^2 B_{22}^2 + 2 f_2 g_2 R_{mT} R_{vT} R_0 B_{22}$$

$$S_{31} = f_1 f_2 B_{11} B_{12} + f_1 g_2 R_{mT} R_{uT} B_{11} + f_2 g_1 R_{mT} R_{uT} B_{12} + g_1 g_2 R_{mT}^2$$

$$S_{32} = f_1 f_2 \left(B_{11} B_{22} + B_{12} B_{21} \right) + f_1 g_2 R_{mT} \left(R_{uT} R_0 B_{11} + R_{vT} B_{21} \right)$$
$$+ f_2 g_1 R_{mT} \left(R_{uT} R_0 B_{12} + R_{vT} B_{22} \right) + 2 g_1 g_2 R_{mT}^2 R_0$$

$$S_{33} = f_1 f_2 B_{21} + f_1 g_2 R_{mT} R_{vT} R_0 B_{21} + f_2 g_1 R_{mT} R_{vT} R_0 B_{22}$$

where

$$R_{mT} = \frac{\beta + \alpha \theta}{1 - \theta}$$

$$R_{uT} = \frac{\overline{(\rho u)' T_t'}}{\sqrt{\overline{(\rho u)'^2}} \sqrt{\overline{T_t'^2}}}$$

$$R_{vT} = \frac{\overline{(\rho v)' T_t'}}{\sqrt{\overline{(\rho v)'^2}} \sqrt{\overline{T_t'^2}}} \qquad (4.28)$$

$$R_{wT} = \frac{\overline{(\rho w)' T_t'}}{\sqrt{\overline{(\rho w)'^2}} \sqrt{\overline{T_t'^2}}}$$

Past work has shown for boundary layers $R_{uT} \in [0.6, 0.9]$. There is little data, however, concerning R_{uT}, R_{vT}, and R_{wT} for free mixing layers. The present study invoked the typical assumption that $T_t' \approx 0$ (the second term on the right-hand side of Eqn. (4.9) was neglected). This arises from setting $\kappa = 1$ or $R_{mT} = 0$ and is generally accepted to be accurate for overheat ratios greater than 1.9 (all single overheat data in this were taken at OHR~2.0). This is true because the sensitivity g decreases as the OHR is increased. Thus, values for R_{uT}, R_{vT}, and R_{wT} were not needed here.

24

All of the single and multiple overheat ratio data reduction techniques have been coded in the FORTRAN program MSHeAR.[25]

4.2.4 Separation of Turbulence Variables

The information provided by multiple overheat cross-wire anemometry in supersonic flow includes the following "conservative" variable turbulence data

$$\overline{(\rho\, u_i)'\, (\rho\, u_j)'} \qquad \overline{T_t'^2} \qquad \overline{(\rho\, u_i)'\, T_t'} \qquad\qquad (4.29)$$

In order to separate the "conserved" turbulence data into "nonconservative" variables, two assumptions were made.

The first assumption, that the pressure fluctuations are small compared to the density and temperature fluctuations, is still controversial. Kistler[26] has suggested that p' is proportional to u'^2, which is second order and neglected. The validity of the p'~ O(2) (or p' ≈ 0) assumption has been experimentally verified for a Mach 4.0 free mixing layer.[12] The second assumption is the thermally perfect gas assumption (p = ρRT). With first-order assumptions, the following "separated" results can be obtained,[12] which include p' information for completeness

$$\frac{u'}{u} = \frac{(\rho\, u)'}{\rho\, u} - \frac{\rho'}{\rho} \qquad\qquad (4.30)$$

$$\frac{v'}{u} = \frac{(\rho\, v)'}{\rho\, u} - R_0 \frac{\rho'}{\rho} \qquad\qquad (4.31)$$

$$\frac{\rho'}{\rho} = \frac{1}{\alpha + \beta} \left[\beta \left(\frac{(\rho\, u)'}{\rho\, u} \right) - \frac{T_t'}{T_t} + \alpha \frac{p'}{p} \right] \qquad\qquad (4.32)$$

where $\alpha = 1.0 / [1 + 0.5(\gamma - 1)M^2]$ and $\beta = (\gamma - 1)\alpha M^2$. With Equations (4.30)-(4.32) and the p' = 0 assumption, all the turbulent shear terms in the RANS can be obtained.

V. Results

This chapter presents the results of the low angle injection compressible turbulence data acquisition and reduction. Nominal tunnel parameters (without injection) were determined to be $M_\infty = 2.9$, $p_{t\infty} = 203 \pm 4$ kPa, and $T_{t\infty} = 298 \pm 3$ K (see Table 5.1 for a full summary of mean flow parameters). Shadowgraphs of the entire flowfield and schlierens of the area of injection were taken. Mean flow and single overheat data were taken at numerous stations across the flow at two locations downstream of the injector. Multiple overheat data was taken at the furthest downstream station ($x/d = 40$) at the centerline ($z/d = 0$).

Table 5.1 Summary of Mean Flow Parameters

M_∞	2.9
$P_{t\infty}$	200 kPa
$T_{t\infty}$	298 K
Re/m_∞	15×10^6
M_j	1.8
P_{tj}	386 kPa
T_{tj}	298 K
Re/m_j	25×10^6
u_j/u_∞	0.86
ρ_j/ρ_∞	3.29
$(\rho u)_j/(\rho u)_\infty$	2.82
p_j/p_∞	5.44
T_j/T_∞	1.65

5.1 Shadowgraph and Schlieren Analysis

Both shadowgraphs and schlierens provide useful qualitative data on the flowfield. The exposure time (0.6 μsec) was too long to freeze the eddies which would have traveled 0.5 mm during the exposure. Nonetheless, unusual features of the injected flow are visible.

Figure 5.1 is a shadowgraph of the entire test section. The cone-static probe is visible at the $x/d = 40$ station. The strong shock produced by the injection is clearly visible. The weak crossing shocks in the center of the test section below the injector are formed by

slight misalignment of the tunnel sections. The injector shock can be seen reflected from the lower wall and boundary layer. This shock and its reflection are clearly visible in the mean flow Mach number contours (Figure 5.3). The white line at the bottom of the shadowgraph is simply a reflection from the light source off the tunnel floor.

Figure 5.2 is a schlieren of the first half of the flow field. The boundary layers are clearly visible. Shown in greater detail is the injection point and associated flow structures. An unusual feature of this picture is the uneven shock downstream of the injector shock. This shock is somewhat unsteady as it was shaped slightly differently in various schlierens and shadowgraphs. It is most likely a combination of reattachment shock as the boundary layer, initially separated by the jet, reattaches to the tunnel ceiling and a shock from the downstream lip of the injector.

5.2 Conventional Probes

Conventional probe data (Pitot and cone-static) were taken at both x/d stations. The flow area mapped out is approximately 5.08 × 3.96 cm (nearly 50% of the total cross section) (see Fig. 3.3). Normalized Pitot and cone-static pressures as well as Mach number contours are provided in Figs. 5.3-5.5. Approximately 40 points of raw data were averaged per point plotted (approximately 0.5 mm grid spacing). Eleven stations across the flow were taken for a grid spacing of about 4 mm. In addition to providing insight into the mean flow character of the flow, the mean flow data had two additional purposes: to provide needed input for the hot-wire data reduction and to show the extent of jet core penetration to narrow the data taking for the hot-wire data.

No exact definition of jet core size exists, but one can determine the extent to which the jet penetrates the freestream by measuring the position of the jet center. One can approximate the outer dimensions of the jet by mapping Mach number, shear stress, turbulence, etc.

5.3 Conventional Probe Results

5.3.1 Station x/d=20

Based on the Mach contour (Fig. 5.3) the jet core penetrated to y/d = -3.0. The jet
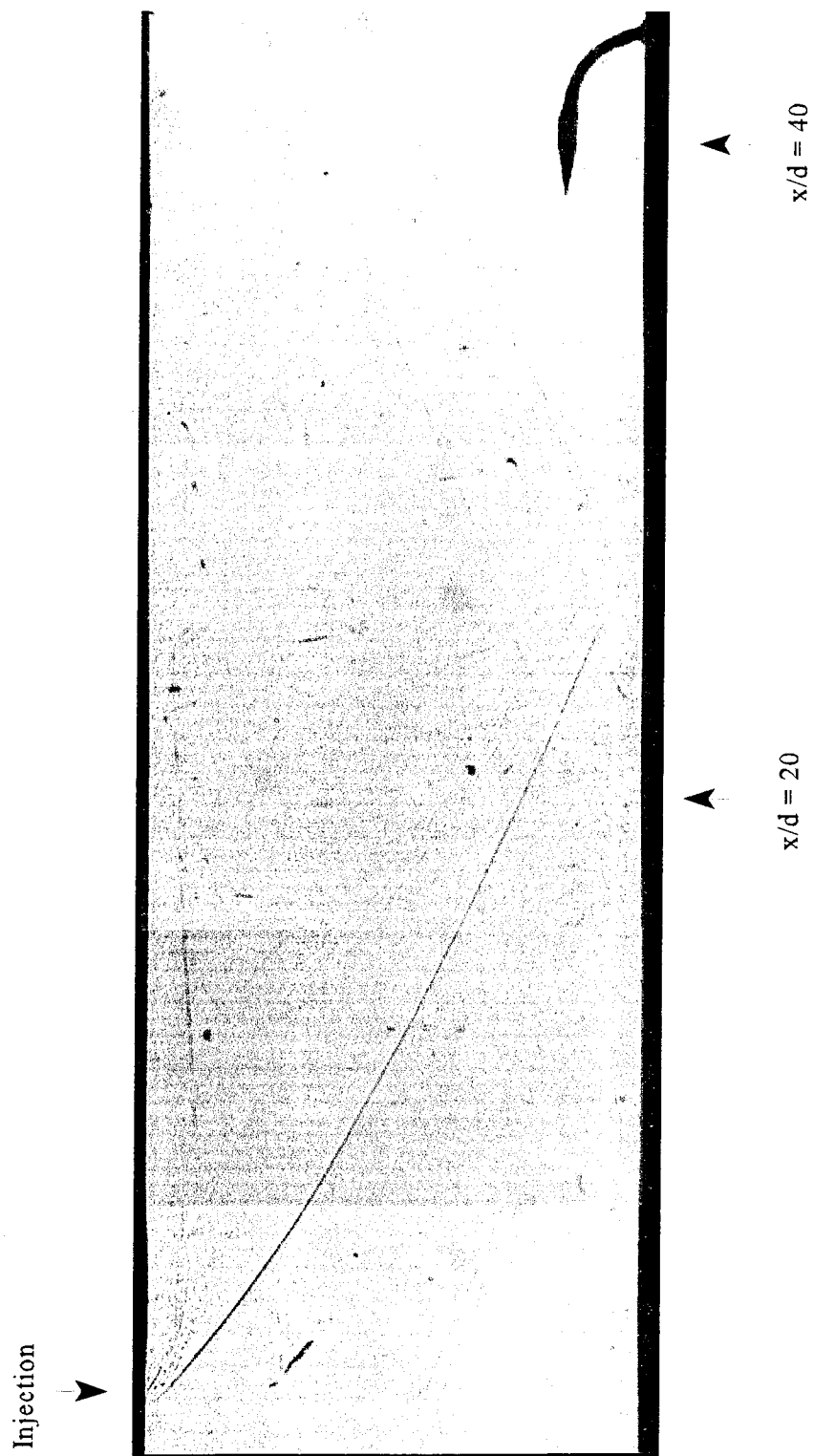
FIGURE 5.1: Shadowgraph of Injector Flowfield

x/d = 40

x/d = 20

Injection

Injection

x/d = 20
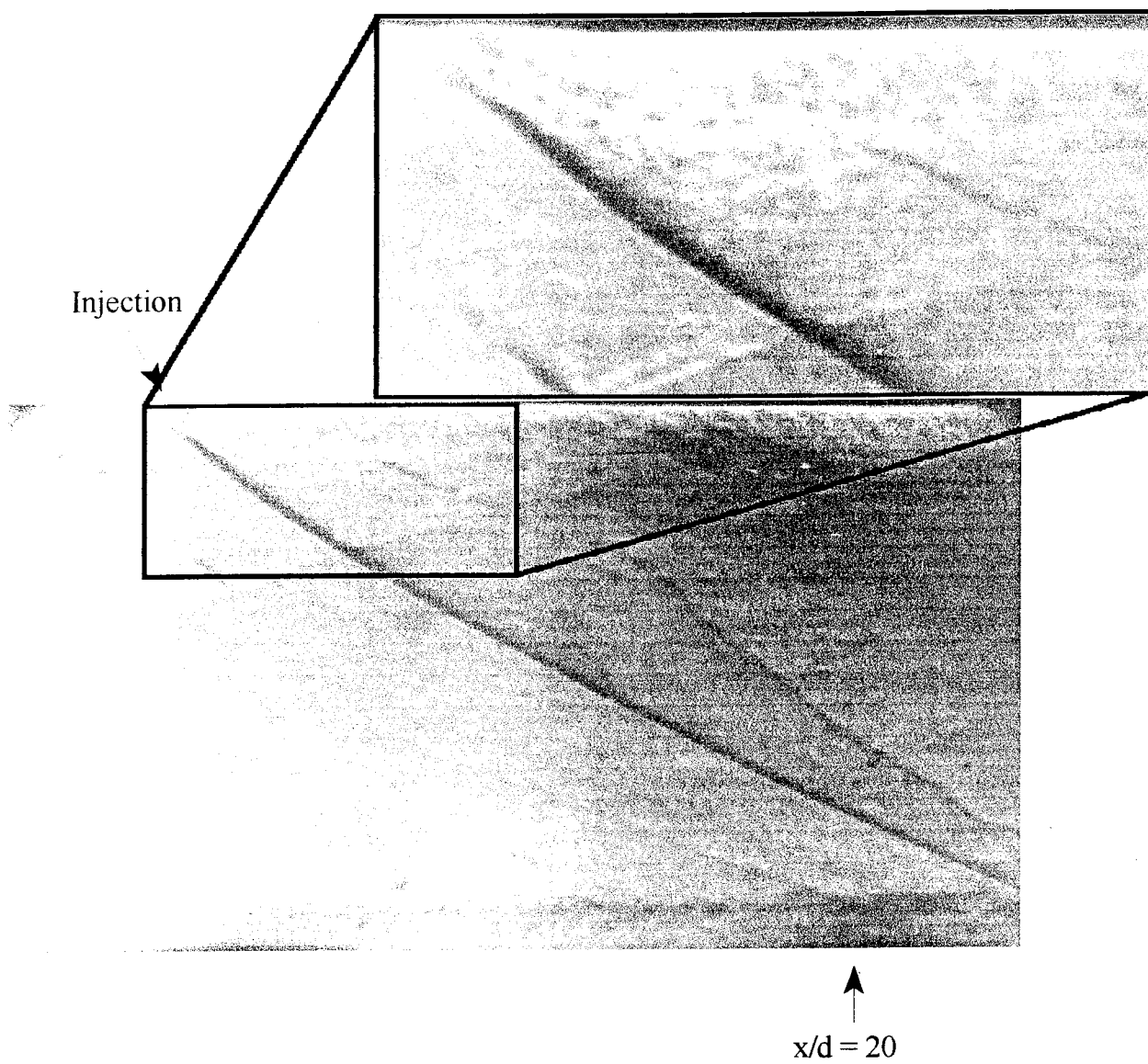
FIGURE 5.2: Schlieren of Injector Flowfield

is roughly symmetrical and encompasses z/d ∈ [-1.6,1.6]. The average diameter of the jet is nominally 3.2d. The boundary layer on the floor of the tunnel is approximately 1.5d, while the boundary layer on the ceiling (injector side) of the tunnel has increased to about 2.0-2.5d because of the action of the jet. It is difficult to determine the exact thickness of the boundary layer at this point because of the interaction with the jet.

5.3.2 Station x/d=40

Again, based on the Mach contour (Fig. 5.3) the jet core has penetrated to y/d = -4.5 with an average diameter of roughly 3.6d. The jet has expanded only slightly to encompass z/d ∈ [-1.8, 1.8]. The boundary layer has not grown significantly by this point because of the short distance between stations (about 7.9 cm). This can be seen in Fig. 5.2 and to a lesser extent, Fig. 5.1. The jet exhibits only slight asymmetry. There are no strong shocks intersecting the upper boundary layer between the injector and x/d = 40. The reflection of the jet shock (although not as sharply defined) is at y/d = -10. Clearly visible at z/d = 3 (and to a much lesser extent at z/d = -3), is a weak vertical structure which is thought to be a shock reflected off the sidewall of the tunnel. This weak shock most likely arises from a slight misalignment of tunnel sections. The Mach number change across the weak shock is less than 0.05. There is a complex, three-dimensional shock pattern in the test section. While the shock visible in Figs. 5.1 and 5.2 reintersects the tunnel ceiling well downstream of the areas of interest, the same cannot be said for the sidewall shocks which have only half the distance to travel from the injector. Another possibility is that of another set of weak misalignment shocks from the nozzle/test section interface. The normalized Pitot and cone-static pressures (Figs. 5.4 and 5.5) follow the same general contour as the Mach number contour. Based on the jet core penetration from Fig. 5.3, it was decided to take hot-wire data in the area z/d ∈ [-3,3] and y/d ∈ [0,9.8].

5.4 Cross-Wire Probes

Single overheat cross-wire data were obtained at every half z/d station from z/d ∈ [-3,3] and at x/d = 20 and 40. The mean flow pressure data were linearly interpolated between stations as needed for the hot-wire data reduction. Multiple overheat data was taken only

30

at the $x/d = 40$ centerline station.

5.4.1 Calibration Technique

The cross-wire probes were calibrated over the range of Reynolds numbers anticipated in the flow field, approximately $15 - 25 \times 10^6$/m, based on the calculated extremes in the tunnel and jet (see Table 5.1). The minimum stagnation pressure at which the tunnel could operate was approximately 159 kPa and the maximum attainable by the pressure regulation and supply system was 290 kPa. The anemometer was tuned in accordance with the IFA 100 manual at roughly 200 kPa whenever a probe was changed. All calibrations were performed at the approximate center of the test section with the injector off. For the calibration run, the tunnel stagnation pressure was varied from the minimum to as close to the maximum as was possible. Roughly ten data points were taken from the calibration process to produce the variables a and b in Eqn. (4.10).

For single overheat data, a calibration run was made at the beginning and end of a data acquisition sequence. Generally, all thirteen z/d stations were taken in a 2-3 hour period. The calibration runs were compared to determine if any electronic drift or probe contamination had occurred. Neither were noted during any test sequence. For multiple overheat data, a calibration run was performed for every overheat ratio. The sequence involved setting the overheat, taking the calibration data, then taking the flow data. This sequence was repeated eight times per probe type.

5.4.2 Single Overheat Data

Two probe types were used: the TSI 1243-20 ("uv" probe) and the TSI 1243AN-20 ("uw" probe). Probe wire resistances as measured by the four-wire method and overheat ratios used appear in Table 5.2. All single overheat ratios were kept in a narrow band OHR $\in [1.99, 2.06]$. At high overheat ratios the probes are less sensitive to temperature fluctuations (i.e. the second term of the right-hand side of Eqn. (4.9) is small compared to the rest). That is, the wire temperature is much greater than the flow temperature.

31

Table 5.2 Cross-Wire Probe Operating Resistances and Overheat Ratios

Probe	Station	Wire 1, Ω (OHR)	Wire 2, Ω (OHR)
uv	x/d=20 (SOH)	5.90 (2.00)	5.94 (1.99)
uw	x/d=20 (SOH)	5.59 (2.02)	6.34 (2.01)
uv	x/d=40 (SOH)	5.95 (2.06)	5.99 (2.04)
uv	x/d=40 (MOH)	5.91 (variable)	5.98 (variable)
uw	x/d=40 (SOH)	6.28 (2.05)	6.03 (2.03)
uw	x/d=40 (MOH)	6.20 (variable)	5.96 (variable)

A full set of data was not taken at $x/d = 20$ with the "uw" probe. A series of probe wire failures, probably the result of faltering filters allowing small particulates into the flow, left only stations $z/d = $ -3, -2, -1, and 0 measured (half stations were not measured). Therefore, the spatial resolution of any data at $x/d = 20$ requiring the "uw" probe is only half as good as the other stations. All contour plots using the "uw" probe at $x/d = 20$ have the left half reflected onto the right. That is, station $z/d = 3$ was used as $z/d = $ -3, etc. This is a fair practice since with only one exception (flow angles, Fig 5.13 and velocity component w, Fig. 5.50) the jet exhibits a high degree of symmetry.

5.4.3 Multiple Overheat Data

Eight overheat ratios were taken with each probe type at overheats based on the chart in Section 3.6.3. The overheat ratios ranged from 1.25 to 2.1, but the highest overheat and lowest ratios were generally not used because they exhibited instabilities. Continuous multiple overheat data were taken (one overheat ratio per run) and combined.

Table 5.3 Actual Overheat Ratios for Multiple Overheat Data

Overheat	"uv" Probe		"uw" Probe	
	Wire 1	Wire 2	Wire 1	Wire 2
1	2.08	2.06	†	†
2	1.99	1.97	1.96	1.96
3	1.83	1.80	1.83	1.82
4	1.73	1.71	1.75	1.73
5	1.63	1.61	1.58	1.61
6	1.54	1.52	1.51	1.48
7	1.35	1.33	1.34	1.36
8	1.26	1.24	1.25	1.27

† The probe failed on this run.

5.5 Cross-Wire Probe Results

The "uv" and "uw" cross-wire probes generally showed good fidelity on quantities which both probes measured. Turbulence intensity (Figs 5.6 and 5.10) was within ±2% based on the root-mean-square (rms) quantities. Favre terms (Figs 5.23 and 5.24) matched to within ±0.001. Separated turbulence intensities (Figs. 5.29, 5.30, 5.31, and 5.32) were within ±1% rms. Density-velocity correlations (Figs. 5.37 and 5.38) were within ±0.002. Finally, mean velocities (Figs. 5.47 and 5.48) were within ±10 m/sec. One exception to the previous generality is in measurements in the boundary layer (upper reaches of Figs. 5.53(a) and 5.54(a)).

This difference is thought to arise out of both the scale and orientation of the probes. Both probes are easily larger than the smaller eddies encountered in the flow field and would be expected to evince some scatter between them. More importantly perhaps, is the orientation of the probe wires. The "uv" probe's wires are oriented vertically (perpendicular to the tunnel floor). In this orientation, the probe wires are less affected by sharp vertical gradients as are found in the boundary layer. The "uw" probe's wires are oriented horizontally so that in a sharp vertical gradient the two wires could experience

vastly different flows. One solution to the problem would be to ensure the probe wires are never perpendicular to such a gradient.

5.5.1 Single Overheat Cross-Wire Results

The single overheat results are shown in contour plots labeled Figs. 5.6-5.52. Each figure contains two contour plots one for the x/d = 20 station (a) and one for the x/d = 40 (b) station except for Fig. 5.51 which contains a single plot at the x/d = 40 station.

Perhaps the most interesting gross feature of the injected flow is a slight bifurcation of the jet. The bifurcation is clearly visible in Fig. 5.6 at both x/d stations. The phenomenon is also apparent in all turbulence intensity, Favre, turbulent kinetic energy, vorticity, and most shear stress graphs. This bifurcation probably arises from vortical motion in the jet itself, not unlike the wingtip vortices seen on aircraft. No similar phenomenon was observed in the literature. It should be noted that most literature on low-angle injection involves helium injection with measurement of concentration in the jet. The measurement techniques employed are not designed to measure the observed vortical motion.

The apparent existence of the bifurcation is bolstered by direct flow angle (Figs. 5.9 and 5.13) and mean flow velocity (Figs. 5.49 and 5.50) measurements. The V and W mean flow velocities were combined into a single graph of vorticity about the x-axis (Fig. 5.51). The figure shows the bifurcations to be two counterrotating vortices of nearly equal strength.

Two hypothesis are proposed to account for the phenomenon. First, the bifurcation may arise, or at least be bolstered, by the design of the injector. Recall from Fig. 3.2 and Section 3.2.2 that the lower half of the injector settling chamber is spherical. This could induce opposing vortices. However, boundary layer vorticity is the more likely player.

As the jet enters the boundary layer it causes a temporary separation which serves to entrain the boundary layer into the jet (see Fig. 5.3). Additionally, flow around the jet would lead to some vortical motion. The jet was modeled as a half cone in the flow for the purpose of determining P_{eb}, which is true initially, but as the jet rises out of the boundary layer it behaves more like a cylinder inclined to the flow. As the flow wraps around the cylinder, it can impart some vortical motion on the jet itself.

In Fig. 5.6, and subsequent figures, the jet appears more rounded than in the Mach

34

contour. While the measured center of penetration of the core does not change appreciably ($< 0.1d$), the extent of influence of the jet, which one could consider the diameter of the jet, has increased. At $x/d = 20$, the jet diameter is $4.0d$ and at $x/d = 40$, it is $6.0d$. Measures taken from other turbulence intensity plots and the turbulent kinetic energy plot (Fig. 5.14) show roughly ($\pm 0.2d$) the same jet diameter. Turblulence intensity is likely a better indicator of jet size in the freestream.

As shown in previous studies,[12] compressibility accounts for about 50-75% of Reynolds shear stress. Figs 5.15-5.18 show the separated Reynolds shear components as measured by the "uv" probe. Fig. 5.15 shows the incompressible portion (first term of Eqn. (2.14)), while Figs. 5.16 and 5.17 show the compressible components (second and third terms of Eqn. (2.14)). Note the maximum values of Figs. 5.15-5.17. The incompressible portion is approximately half that of the first compressible term while the second incompressible term is an order of magnitude smaller than the first. The third term can be safely ignored in turbulence models, however, since the second term accounts for roughly 67% of the total Reynolds shear stress (Fig. 5.18) it cannot be ignored and must, in fact, be rigorously included. The same analysis, with the same result, can be applied to the Reynolds shear measured by the "uw" probe (Figs. 5.19-5.22).

Since most modern turbulence models are based on the Favre-averaged Navier-Stokes equations Favre data is included as Figs. 5.23-5.28. Notice that the Favre shear (Figs. 5.27 and 5.28) match nearly exactly the incompressible portion of the Reynolds shear (Figs. 5.15 and 5.19). This result is expected since the FANS equations bear a close resemblance to the incompressible RANS.

For completeness, the separated turbulence intensities $(\rho'/\rho)_{rms}$, $(u'/u)_{rms}$, $(v'/u)_{rms}$, and $(w'/u)_{rms}$ are included as Figs. 5.29-5.34. Also, the velocity-velocity and velocity-density correlations are included as Figs. 5.35-5.40.

Turbulent shear stress obtained through the turbulence transformation process discussed in Section 2.4 are presented as Figs. 5.41-5.46. For data obtained with the "uv" probe, Fig. 5.41 shows the first term of Eqn. (2.21), Fig. 5.42 shows the second term, and Fig. 5.43 shows the total. Figs. 5.44-5.46 show the "uw" probe data. The data indicate the first term comprises approximately 90% of the total and, subsequently, the second term is

an order of magnitude smaller than the first. This result is important because it shows the first term to be of primary importance for modeling purposes. It also indicates the validity of the p'=0 assumption discussed in Section 4.2.4 does not have a significant impact on the total transformed shear. This arises because only the second term of Eqn. (2.21) is reliant on separation of variables which requires the p'=0 assumption. Thus, even if the p'=0 assumption is found to invalid, the total transformed shear would be minimally affected.

Mean velocities and mean mass flux are provided in Figs. 5.47-5.50 and Fig. 5.52 respectively. The data from Figs. 5.49 and 5.50 were used to generate vorticity plot (Fig. 5.51).

5.5.2 Multiple Overheat Cross-Wire Results

Figs. 5.53-5.62 contain the multiple overheat data taken at the x/d = 40 centerline station. Figs. 5.53-5.56 show comparisons of multiple and single overheat data taken at that station.

The multiple overheat data show good agreement with single overheat data taken at the x/d = 40 centerline station. Generally, the multiple overheat data evinces greater scatter than the single overheat. This is true because the multiple overheat data was collected over as many as eight runs while the single overheat was collected in a single run. Some difference in tunnel conditions from run to run is inevitable. Any inherent unsteadiness in the flow will exacerbate the scatter.

Overall, multiple overheat data showed "uw" turbulence intensities (Fig. 5.54) to be less than that measured by the single overheat method but showed "uv" turbulence intensities (Fig. 5.53) to be greater. The opposite trend was visible in shear data (Fig. 5.55). These differences are within the expected error (see Section 5.6).

Flow angle data (Fig 5.56) showed multiple overheat "uv" data to be in close agreement, however, "uw" flow angle data show the single overheat flow data to be off by -4.6°. This error was accounted for in Fig. 5.13 by adding 4.6° to the entire flowfield. Similar analysis of the z component of the mean flow indicated an error of approximately -50 m/sec. Figure 5.50 was corrected as well. The most likely source of this error is a misalignment of the "uw" probe. The nature of hot-wire anemometry tends to reduce small

angular errors, but only when these errors are consistent in both the calibration and data acquisition. Changing the angle of the probe to the flow $\pm 5°$ in the data reduction only varied the final determination of flow angle by $\pm 0.5°$. However, calibrating the probe at one angle and running the data reduction at a different angle produces a change in flow angle nearly equal to the initial difference. It is very likely the data and calibration runs were taken with different probe alignments.

Total temperature turbulence is plotted in Fig. 5.57. It indicates the total temperature fluctuated a maximum of approximately 3% which matches the maximum difference between single and multiple overheat data in Figs. 5.53-5.55. The assumption of small total temperature fluctuation appears valid.

Most of the data in Figs. 5.58-5.62 reach extrema, maxima or minima, near $y/d = -5.0$. This may indicate the center of the jet and therefore jet penetration. However, as seen in the single overheat data, the extreme values of the data did not usually occur at the centerline station. Usually, the extrema occurred at the center of the bifurcations. This leads to some ambiguity in the determination of jet penetration based on compressible turbulence. Since the single and multiple overheat data vary to some degree, more multiple overheat data across the flowfield will be necessary.

Fig. 5.58(a) shows the mass flux/total temperature correlations to track well together until the boundary layer/jet interaction area is reached ($y/d \in [0, 4.5]$). Fig. 5.58(b) indicates the z component of the specific turbulent heat flux to be much less than the other two except in the boundary layer/jet interaction area. This makes physical sense based on the relative velocities and flow angles. At the centerline, the z component of velocity and angle would ideally be zero, and it is quite close to the ideal over most of the centerline. Figs. 5.13 and 5.50 show the departure of the flow angle and velocity from the ideal nearer the wall.

The multiple overheat Reynolds shear stress (Fig. 5.59) complements the single overheat data showing compressibility to account for 60-70% of the total Reynolds shear.

Figs. 5.60-5.62 show the general trends discussed thusfar: extrema at $y/d = -5.0$, increase in absolute magnitude of z components in the boundary layer/jet interaction area, and general departure of "uv" and "uw" data in the boundary layer.

37

5.6 Error Analysis

Scatter, or error, is a natural part of taking any measurement, in particular of an unknown quantity. Presented in this section are some of the sources of error in this work and the extent to which these errors affect the accuracy of the results. The L_2 or Euclidean norm[27] is employed as the measure of error here. The L_2 norm is given by

$$e_x = \left[\sum_{i=1}^{n} e_i^2 \right]^{1/2} \tag{5.1}$$

where i indexes the various errors associated with measurement of the quantity x.

5.6.1 Conventional Probes

Volluz[21] indicates turbulence induces about ±690 Pa error for both Pitot and cone-static probes. The calibration error is approximately 500 Pa for both probes. The settling chamber pressure has an uncertainty of about 1.7 kPa.

The probe was observed to flex about 2.5 mm while the tunnel was in operation, therefore the probe location error is estimated to be ±0.5%. This corresponds to a Mach number error of ±0.2 or ±7%. The error in the local mass flux, based on previous work,[12] is ±2%

5.6.2 Cross-Wire Probes

Multiple overheat data was taken continuously and averaged over every 2,048 points. Based on the speed and data acquisition rate of the probes, the position error is 0.5 mm, however, the largest errors are associated with the calibration. Bowersox[12] indicates conventional probe errors can be carried over into the hot-wire analysis. The calibration errors can be estimated through a perturbation analysis. This analysis has shown error associated with the probe location to be small, primarily because the probe is calibrated at each overheat and each station. As shown in Section 5.5.2, varying the angle of the probe in the flow as much as 5° caused only a 0.5° error in flow angle. Provided the probe is not removed or replaced, misalignment errors will be minimized.

The error analysis of Bowersox[12] has also shown the error arising from linearization

38

of the hot-wire response equation, through the binomial theorem (Chapter 4) to be very small. Bowersox[6] presents the following hot-wire errors associated with similar turbulence measurements under similar flow conditions as those in the present work:

Table 5.4 Cross-Wire Errors*

e_T	7.6%
e_ρ	3.6%
e_u	1.5%
$e_{\rho u}$	2.1%
e_f	1.0%
e_g	1.0%
$e_{()'()'}$	8.4%

*based on M=3.0

Comparison of data measured by both the "uv" and "uw" probes can yield insight into the errors associated with the present flow. As stated in Section 5.5, the u velocity error is 10 m/sec out of a maximum of about 600 m/sec. This is an error of 1.5% and follows well with the errors shown in Table 5.4. The turbulence intensity error is roughly 0.02 rms. Maximum error in the Favre data is approximately 12%. The separated turbulence intensities are within 0.01 rms. Density-velocity correlations have a maximum 12% error.

In the aggregate, the data is repeatable within 12% for the two types of probes which is a good measure of the repeatability from run to run and accounts for all types of measurement errors: probe alignment, temperature, pressure, voltages, etc.
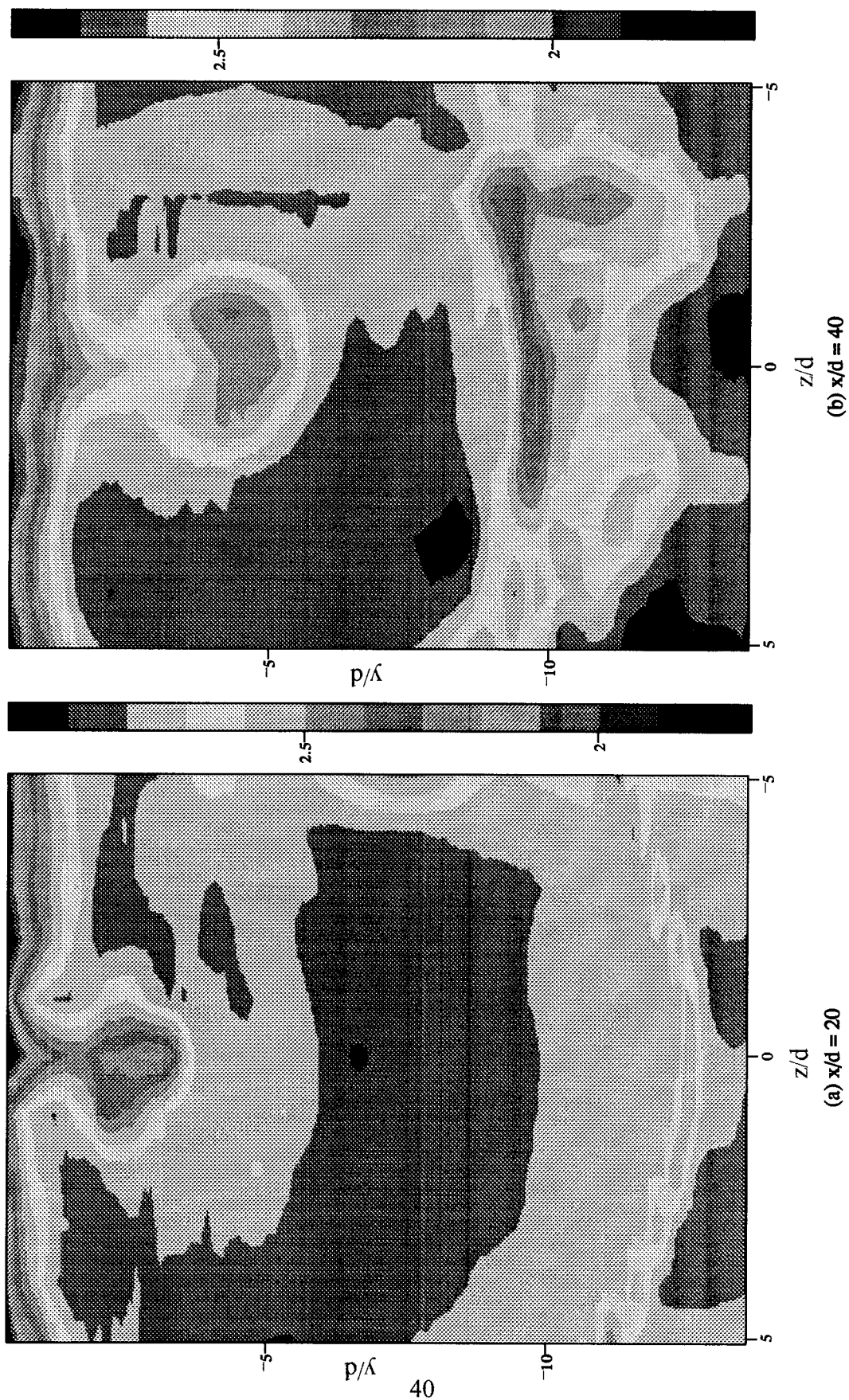
FIGURE 5.3: Mach Number Contours
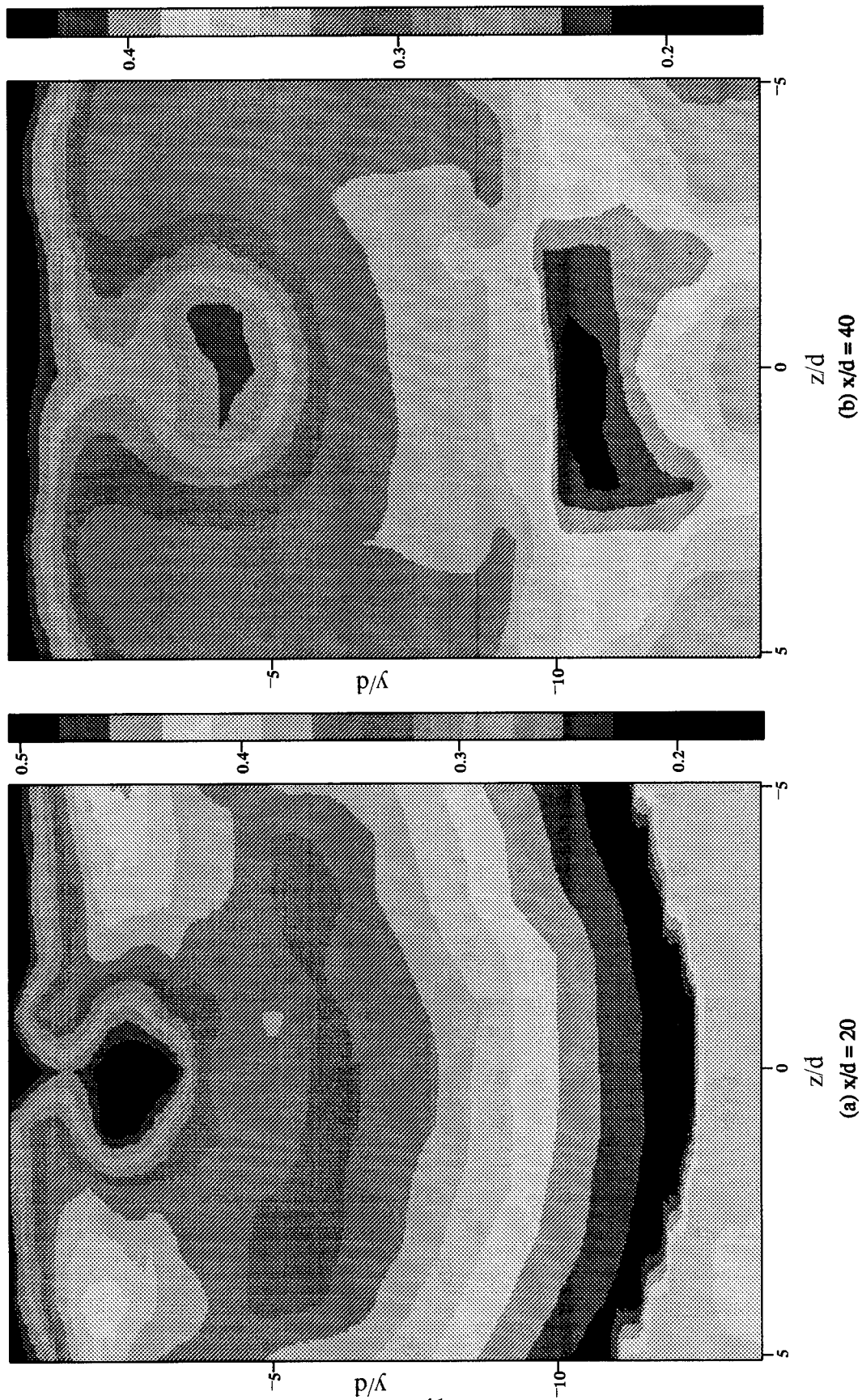
FIGURE 5.4: Normalized Pitot Pressure (p_{t2}/p_{t1})

(a) x/d = 20

(b) x/d = 40

41
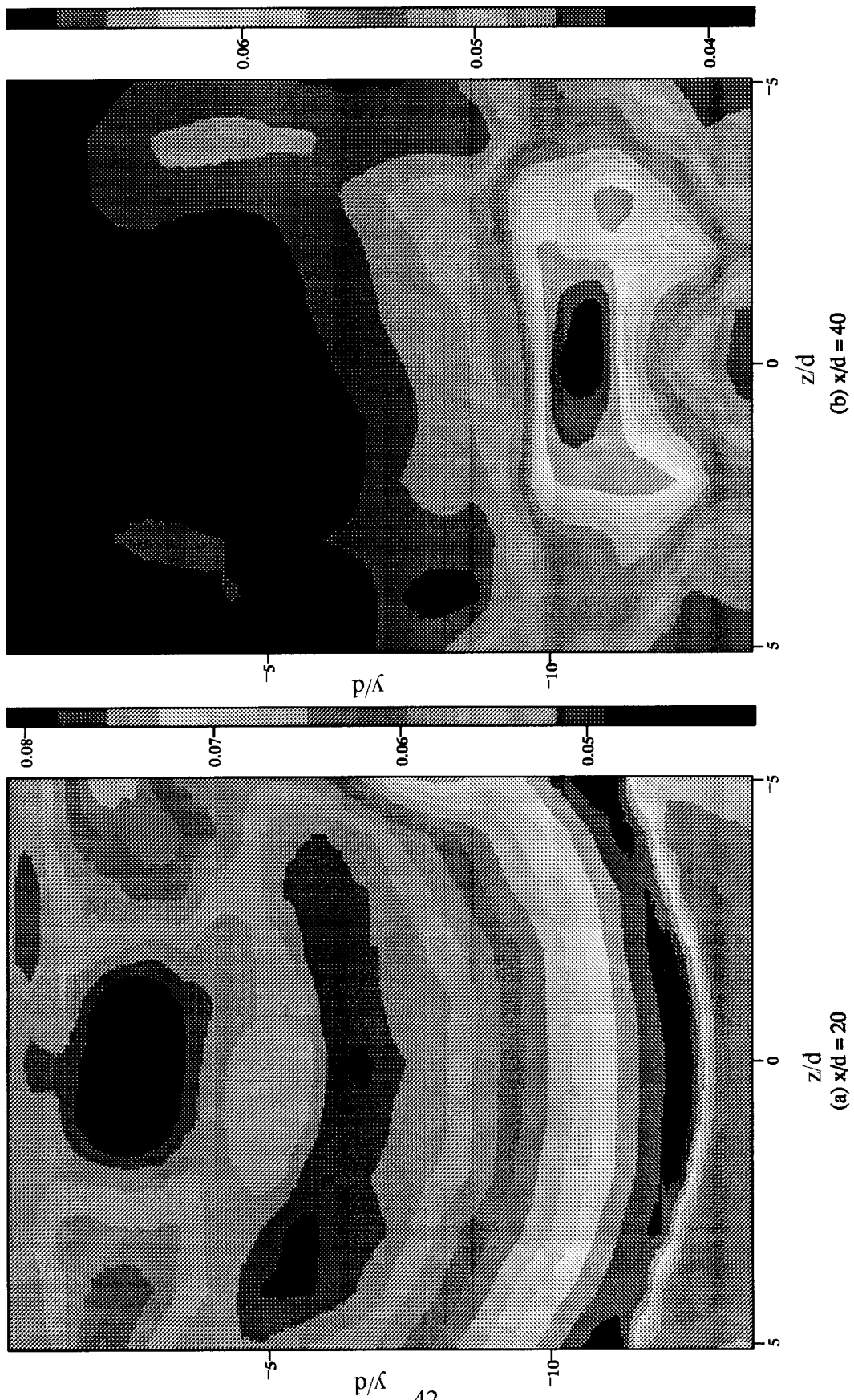
FIGURE 5.5: Normalized Cone-static Pressure (p_c/p_{t1})

(a) x/d = 20

(b) x/d = 40

42
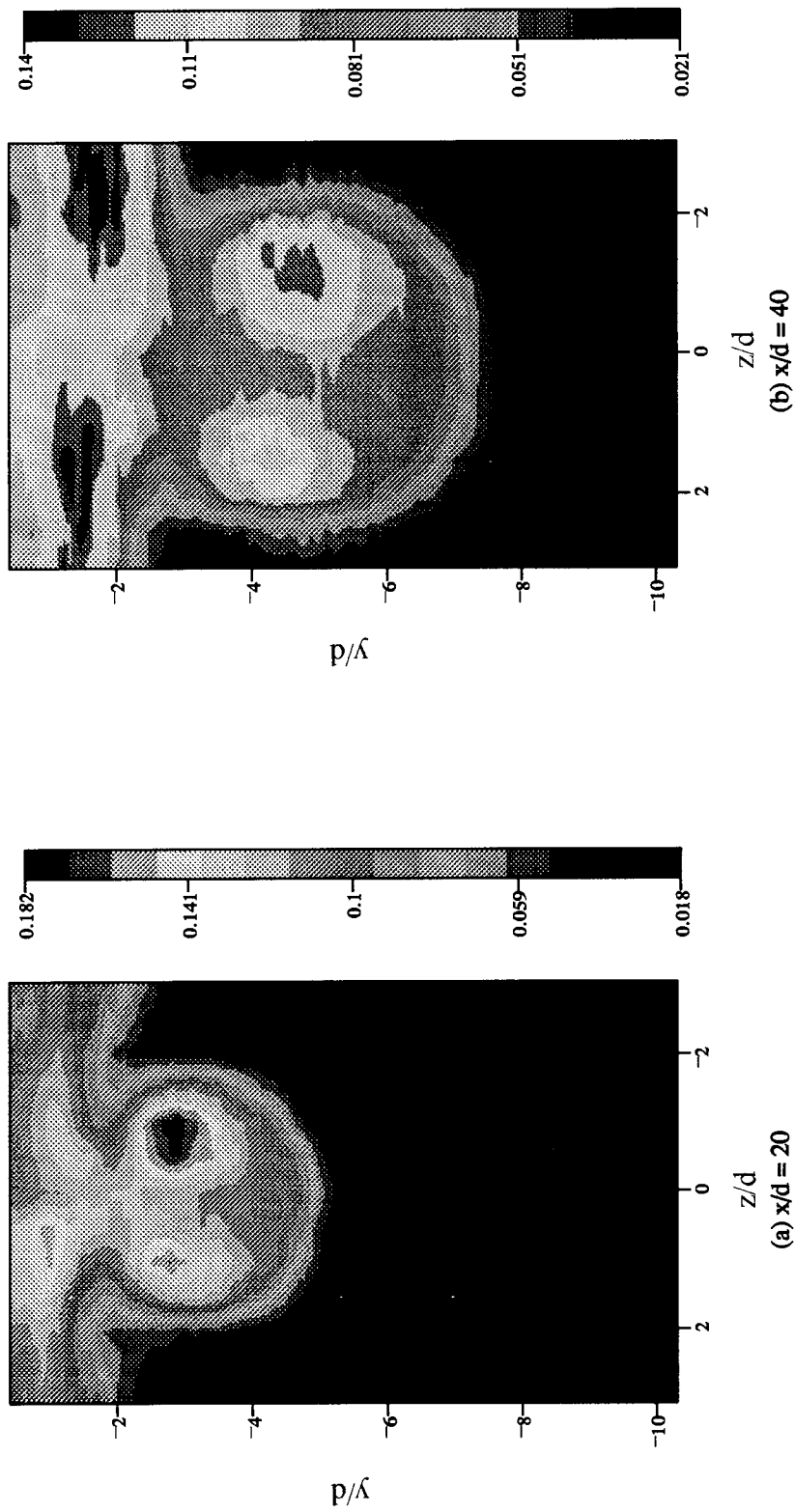
FIGURE 5.6: Turbulence Intensity $[(\rho u)'/\rho u]_{rms}$ (uv probe)

43
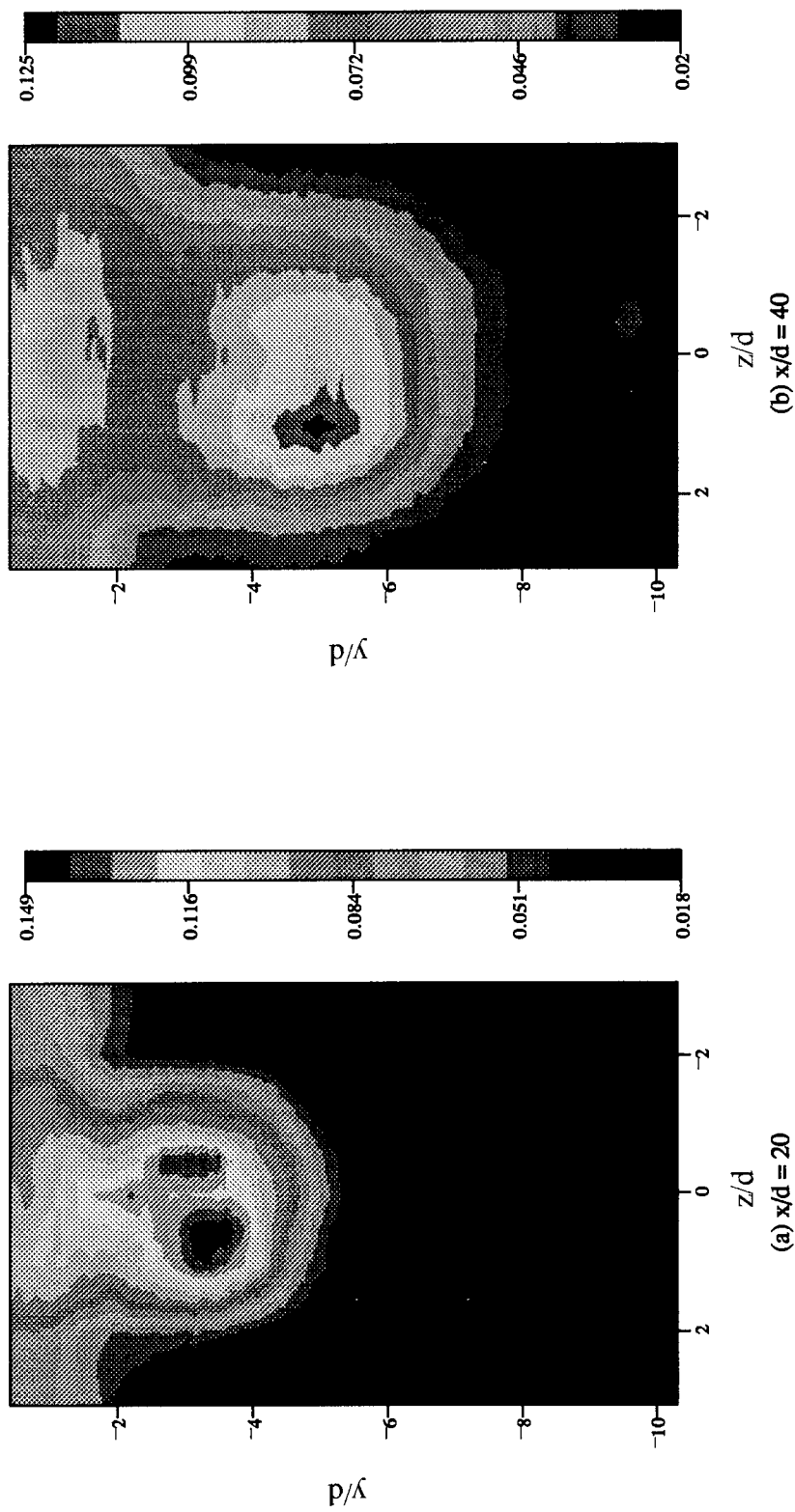
FIGURE 5.7: Turbulence Intensity $[(\rho v)'/\rho u]_{rms}$ (uv probe)
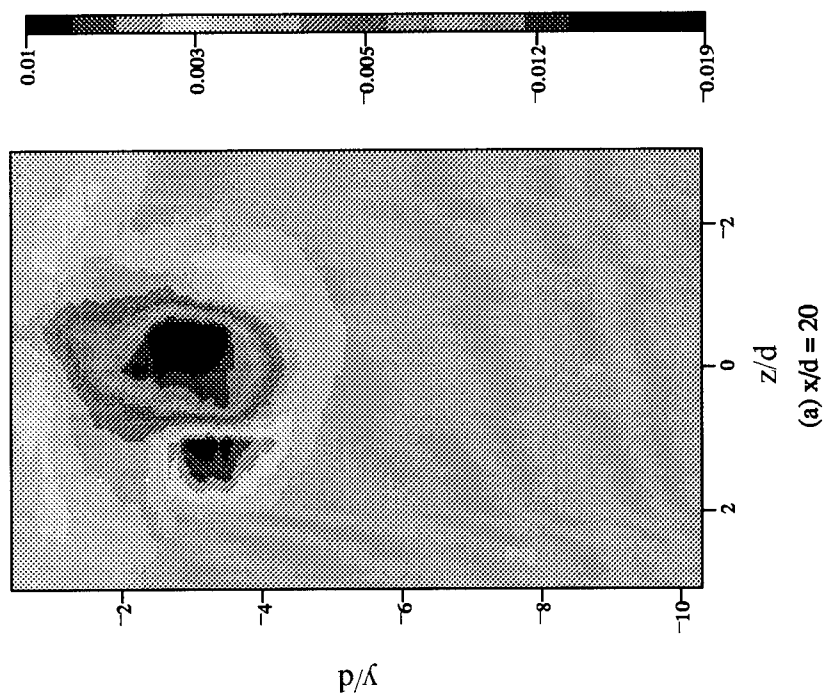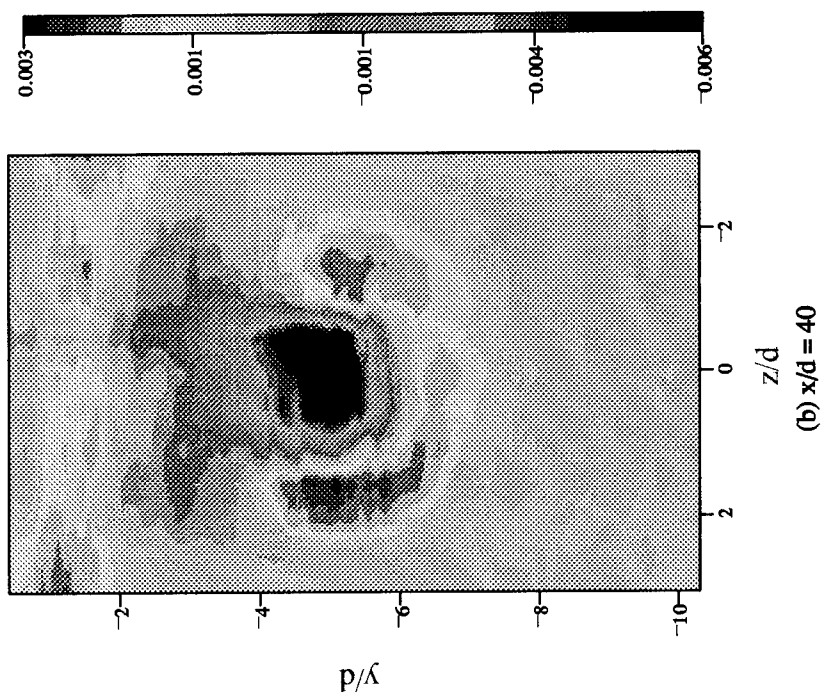
FIGURE 5.8: Shear $[(\rho u)'(\rho v)'/(\rho u)^2]$ (uv probe)
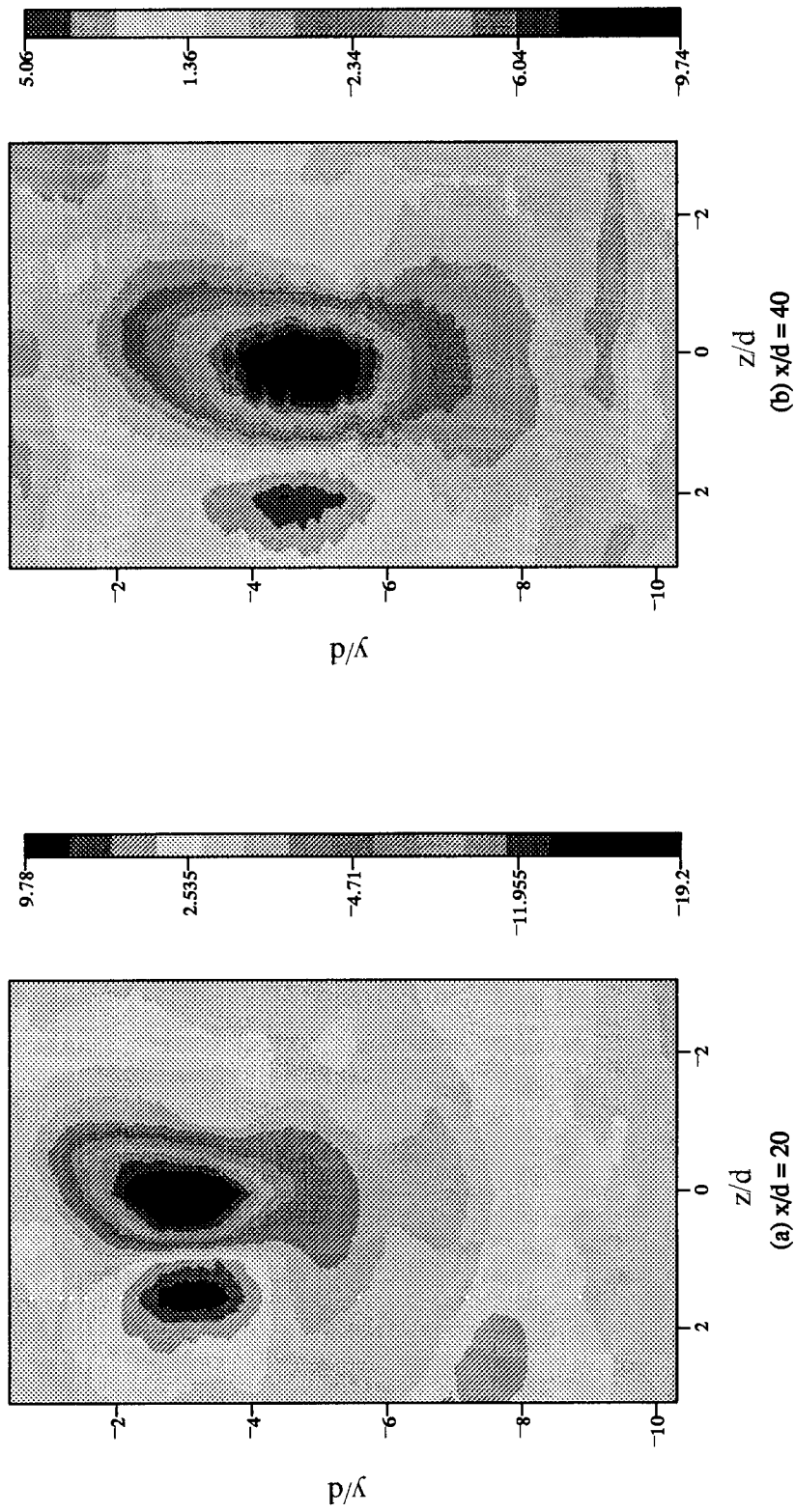
FIGURE 5.9: Flow Angle [$\theta_{pv/pu}$] (uv probe)
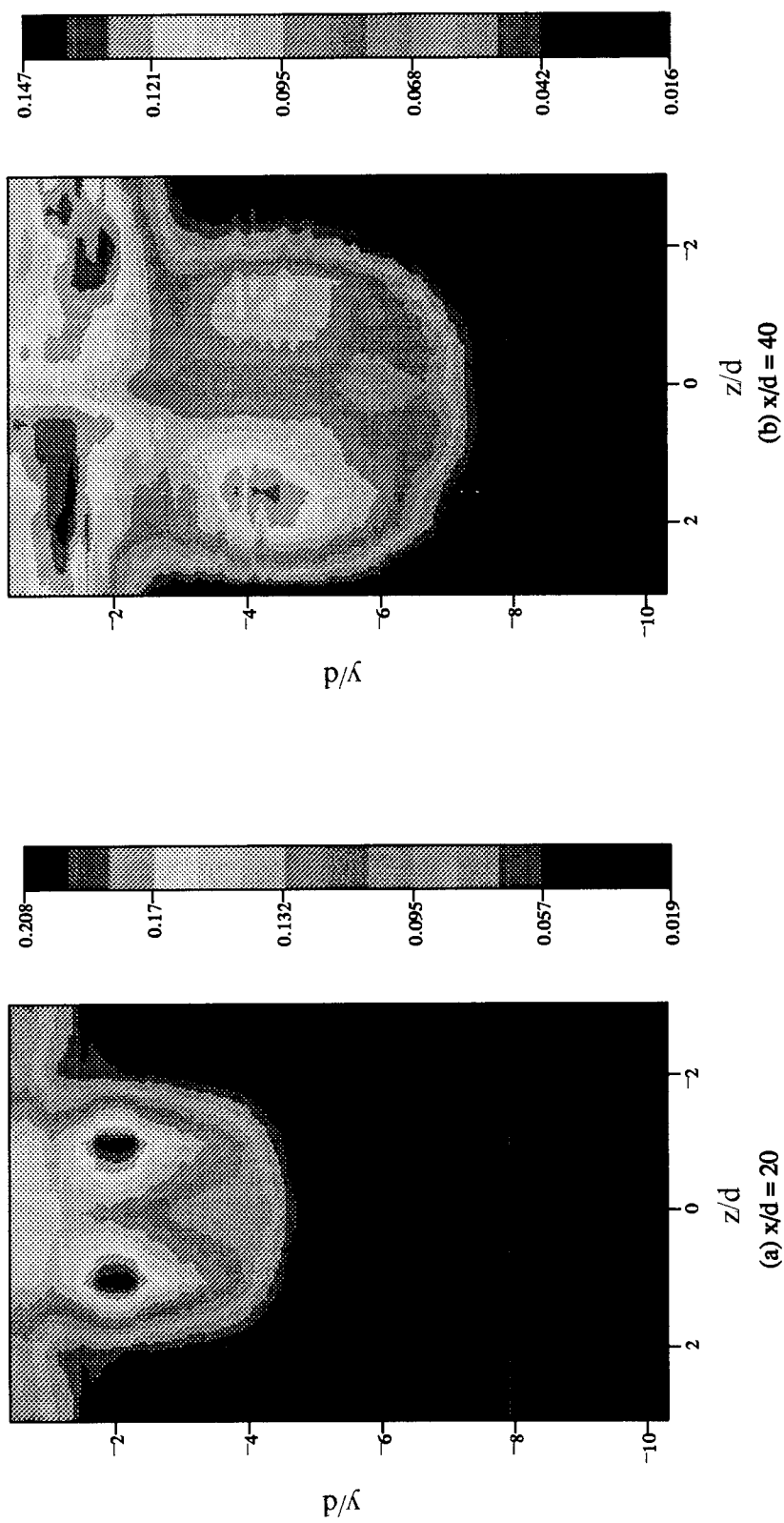
FIGURE 5.10: Turbulence Intensity $[(\rho u)'/\rho u]_{rms}$ (uw probe)

47
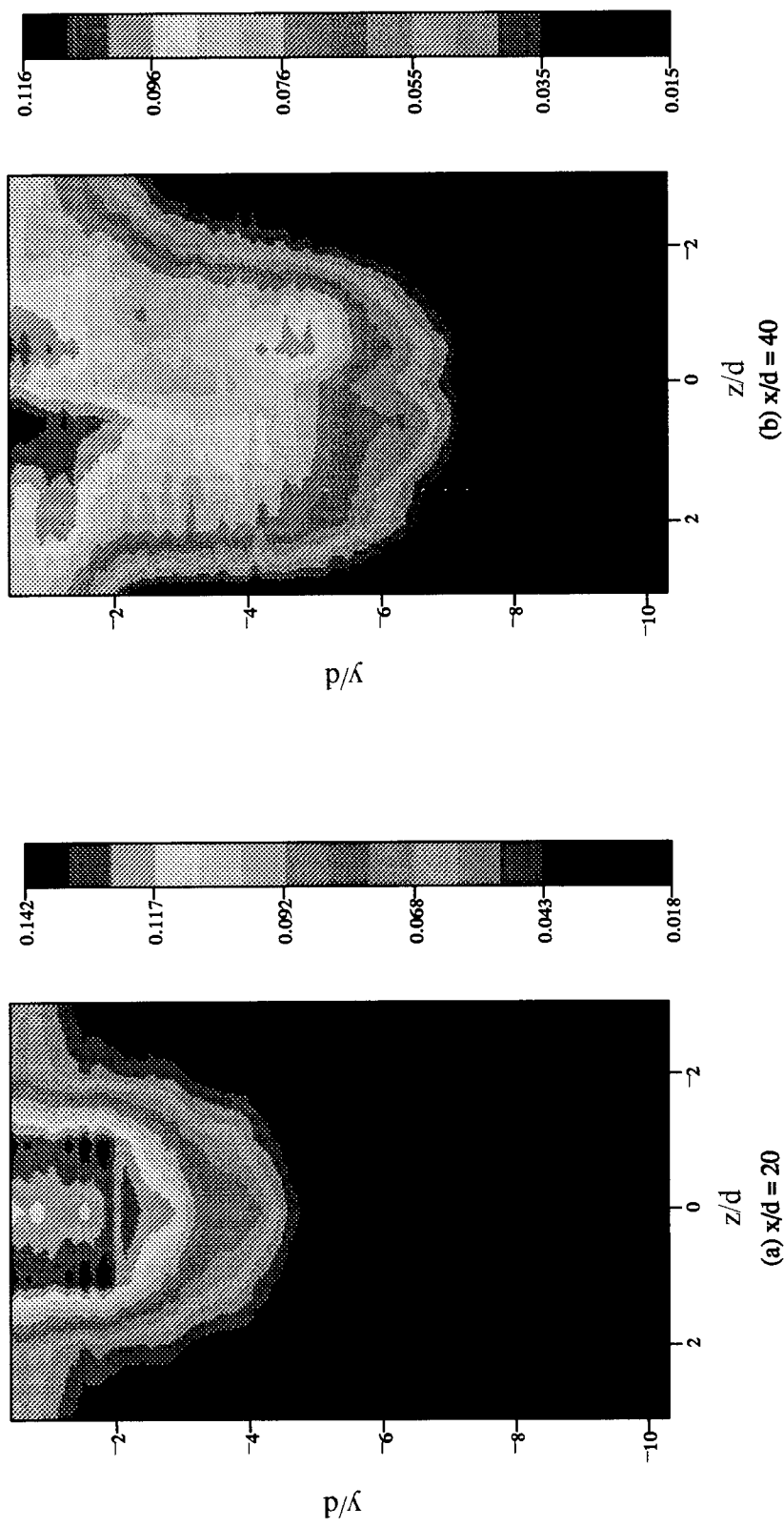
FIGURE 5.11: Turbulence Intensity $[(\rho w)'/\rho u]_{rms}$ (uw probe)
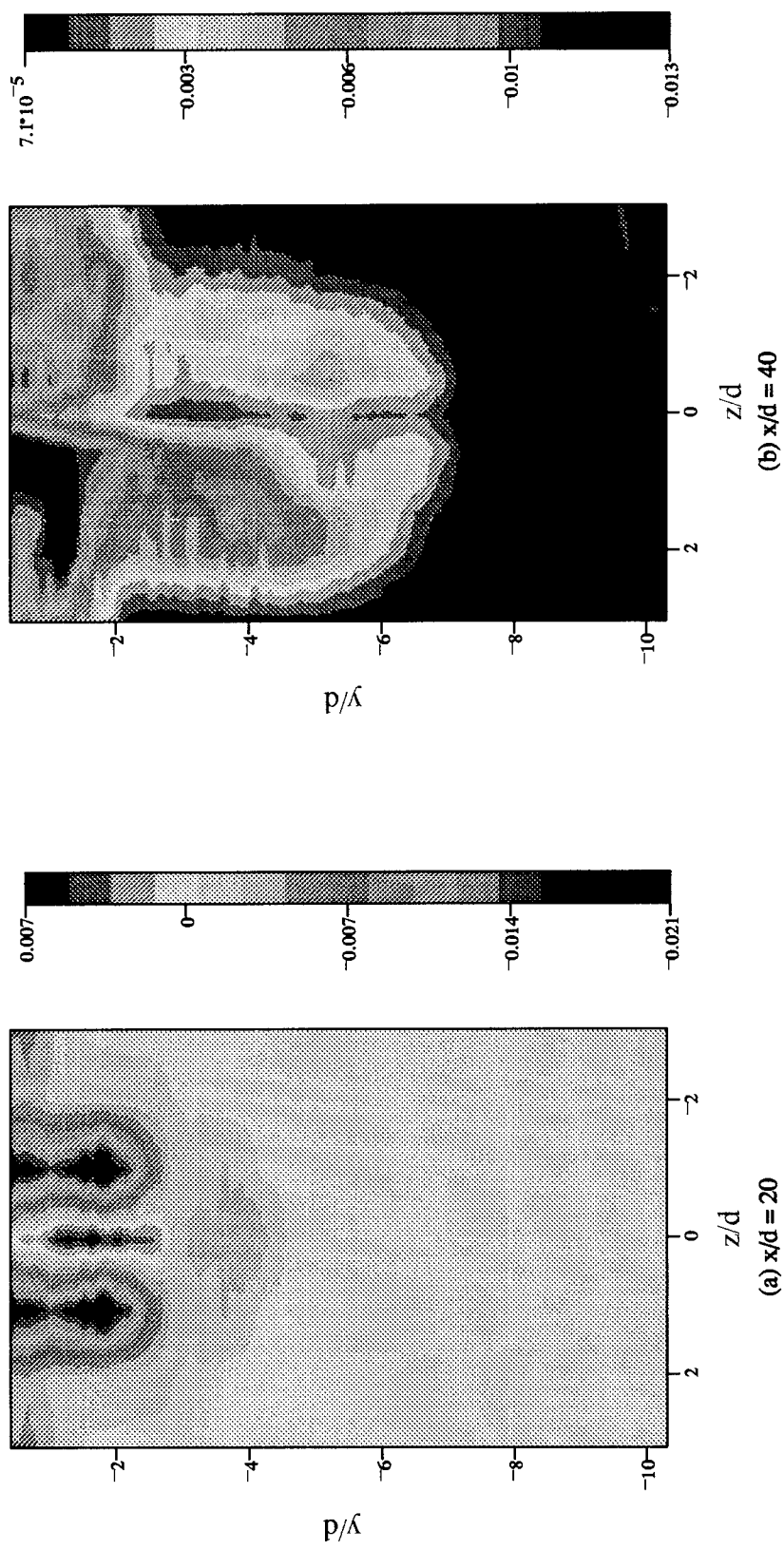
FIGURE 5.12: Shear $[(\rho u)'(\rho w)'/(\rho u)^2]$ (uw probe)
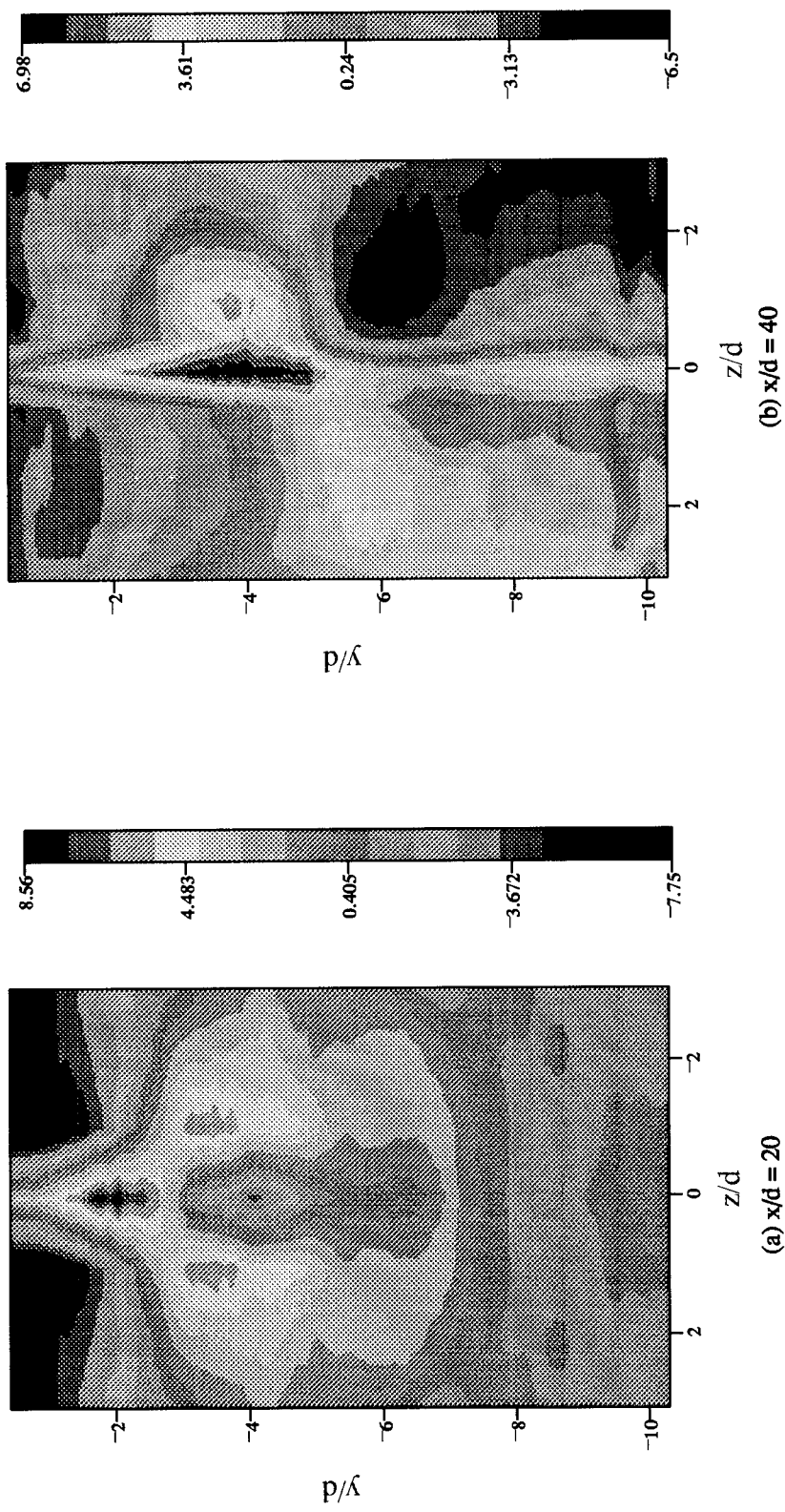
FIGURE 5.13: Flow Angle [$\theta_{\rho w/\rho u}$] (uw probe)
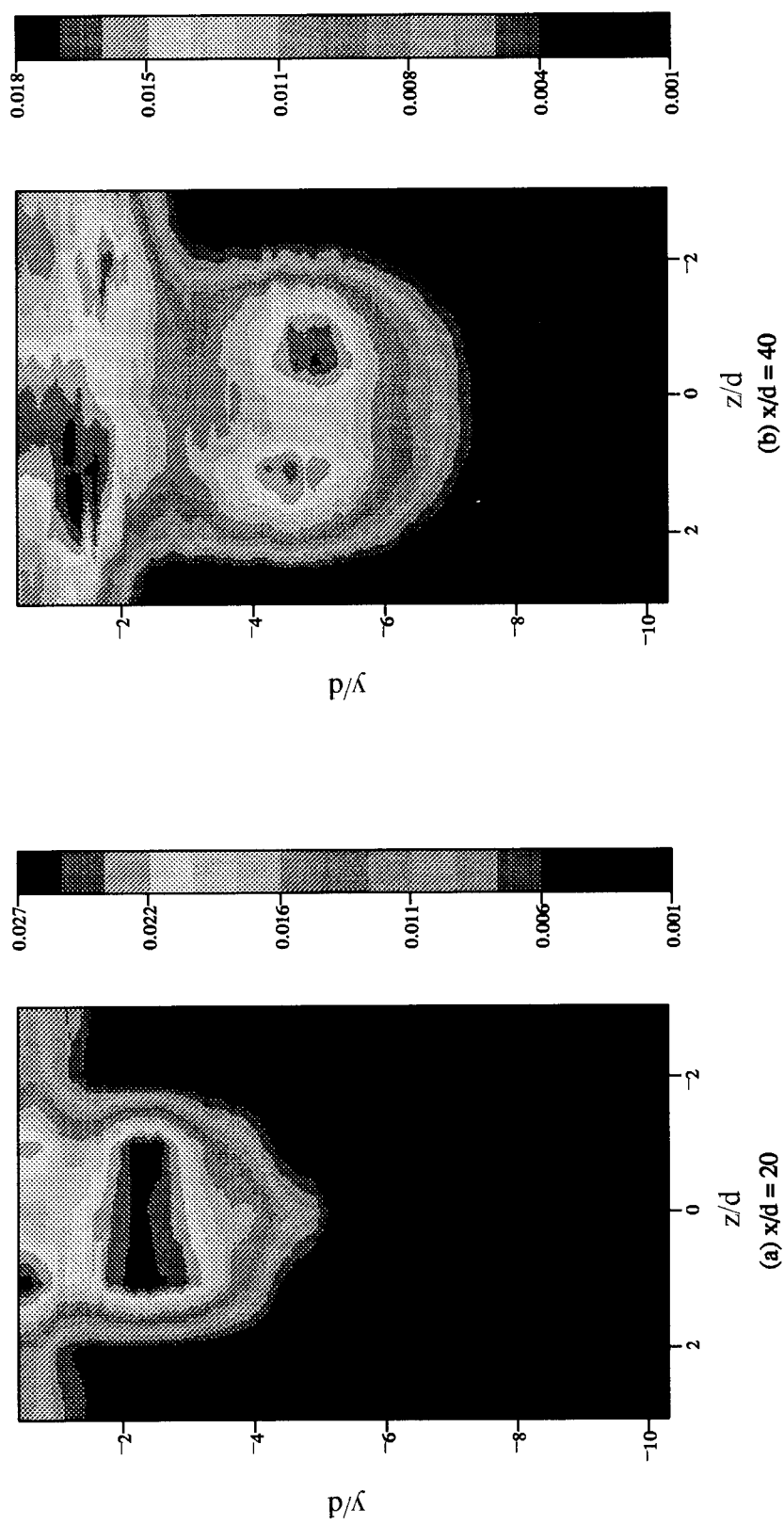
FIGURE 5.14: Turbulent Kinetic Energy [TKE/u^2]
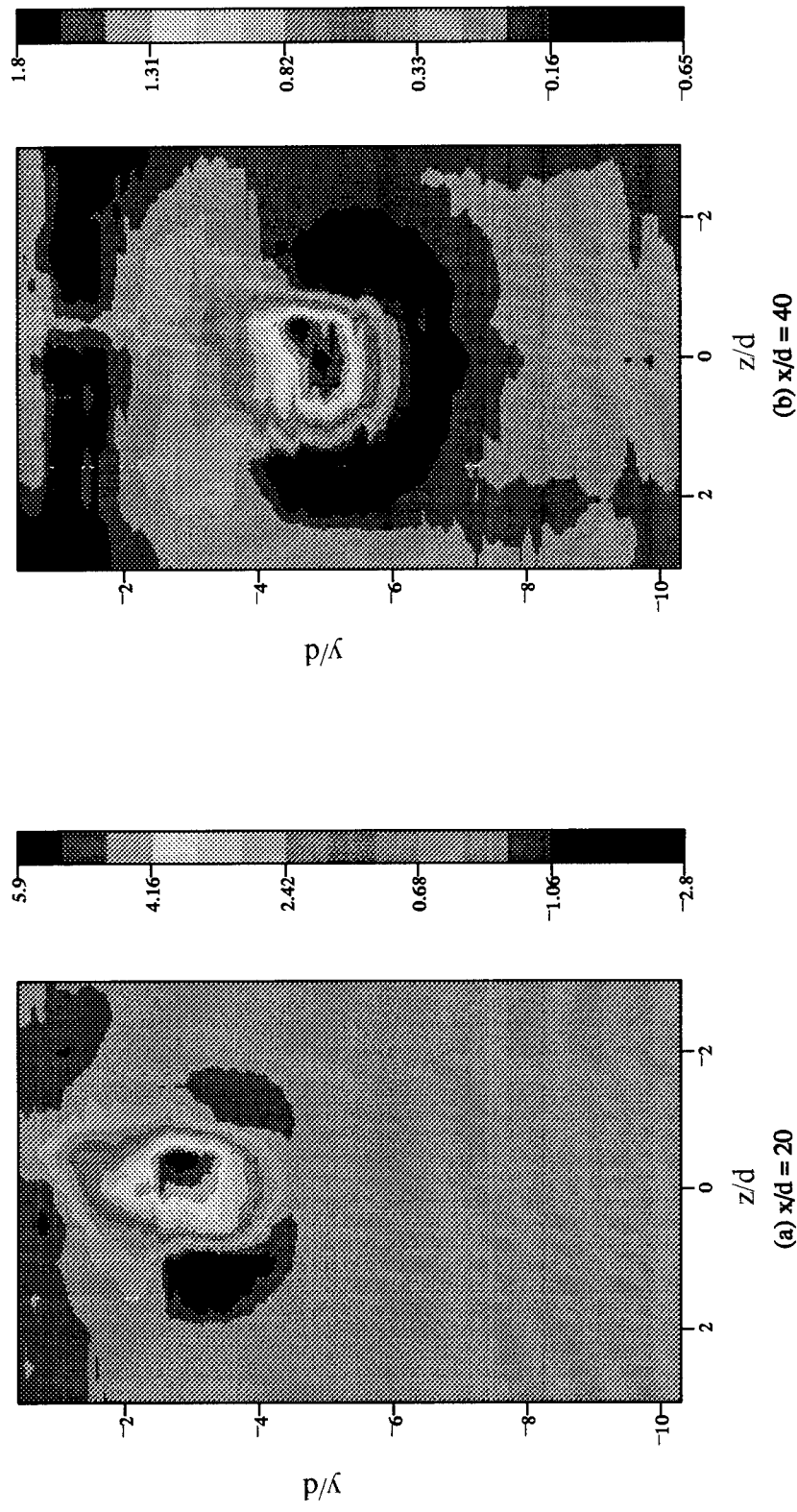
FIGURE 5.15: Separated Reynolds Shear [$-\rho u'v'/\rho u^2$] (uv probe) ($\times 10^3$)
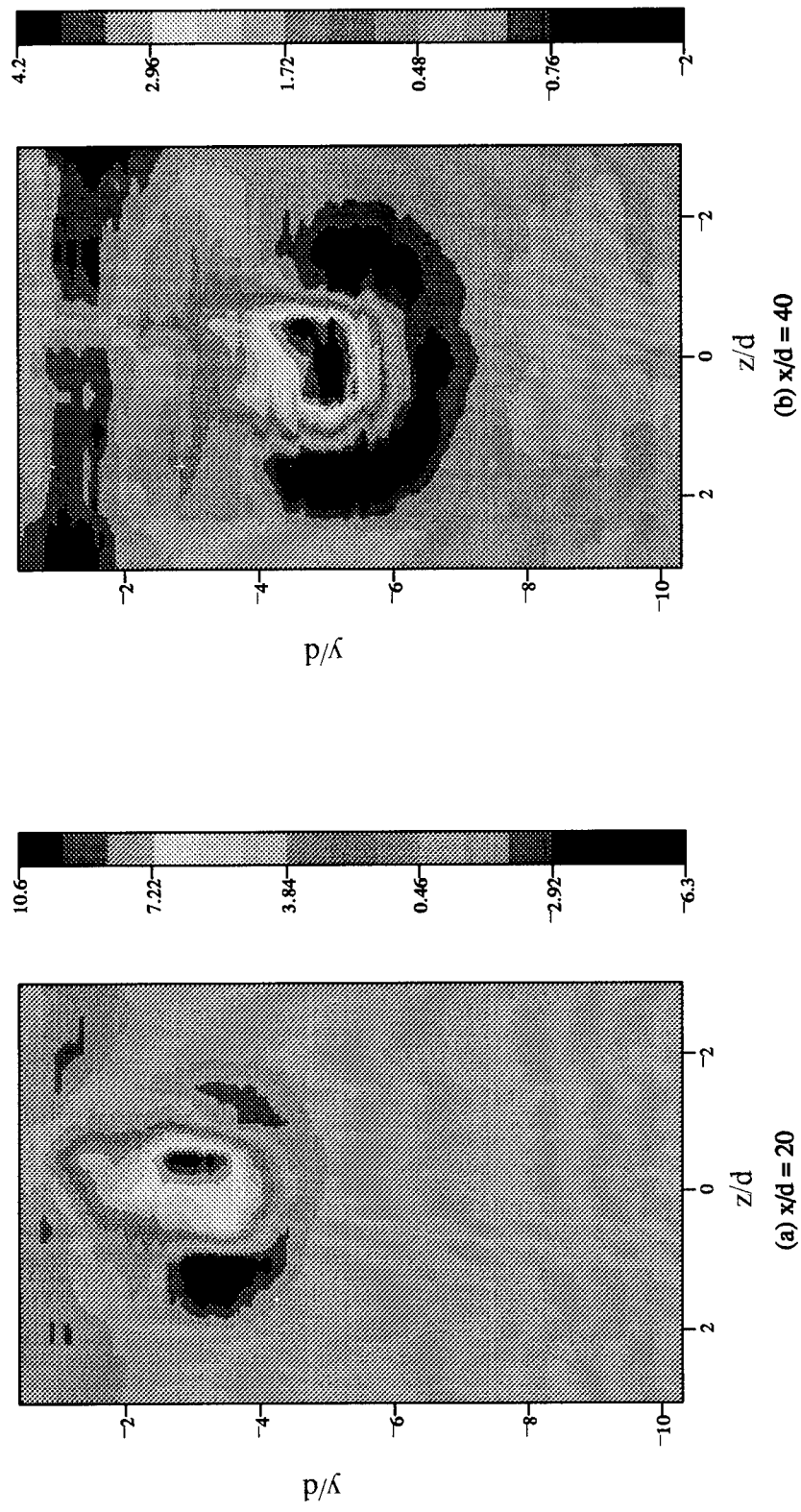
FIGURE 5.16: Separated Reynolds Shear $[-u\rho'v'/\rho u^2]$ (uv probe) (x10³)
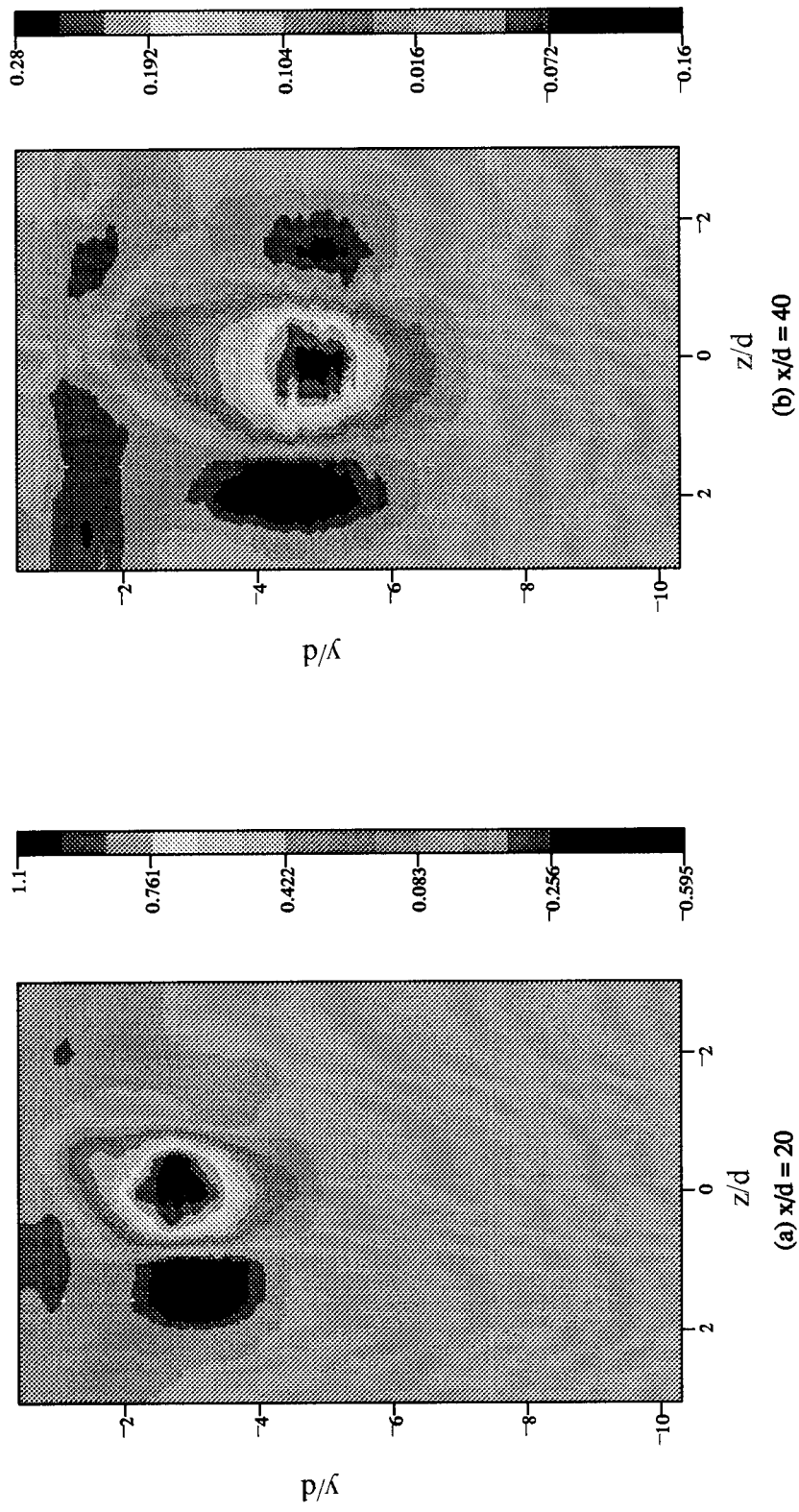
FIGURE 5.17: Separated Reynolds Shear $[-v\rho'u'/\rho u^2]$ (uv probe) (x10³)
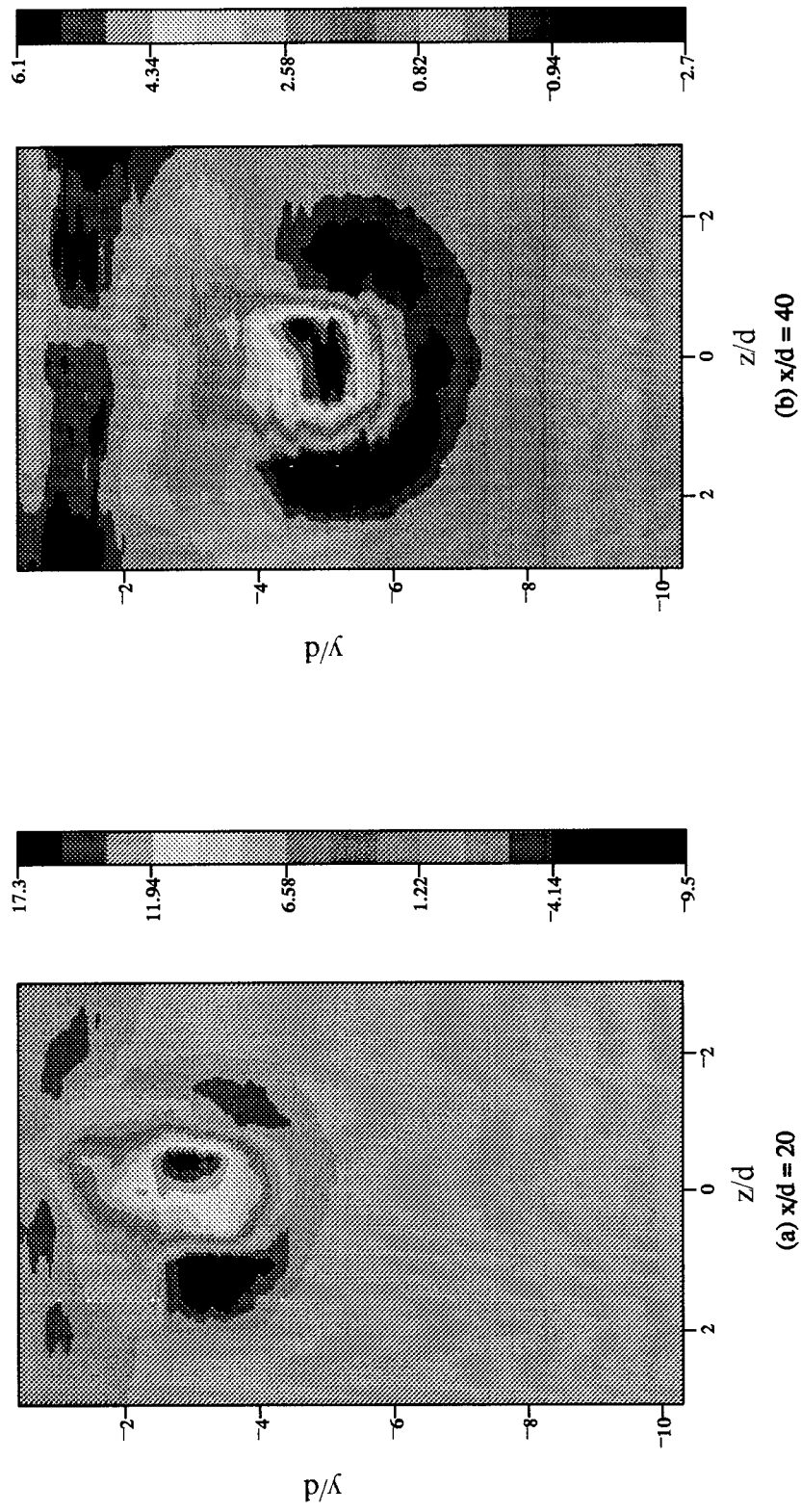
FIGURE 5.18: Separated Reynolds Shear [Reynolds Shear] (uv probe) (x10³)
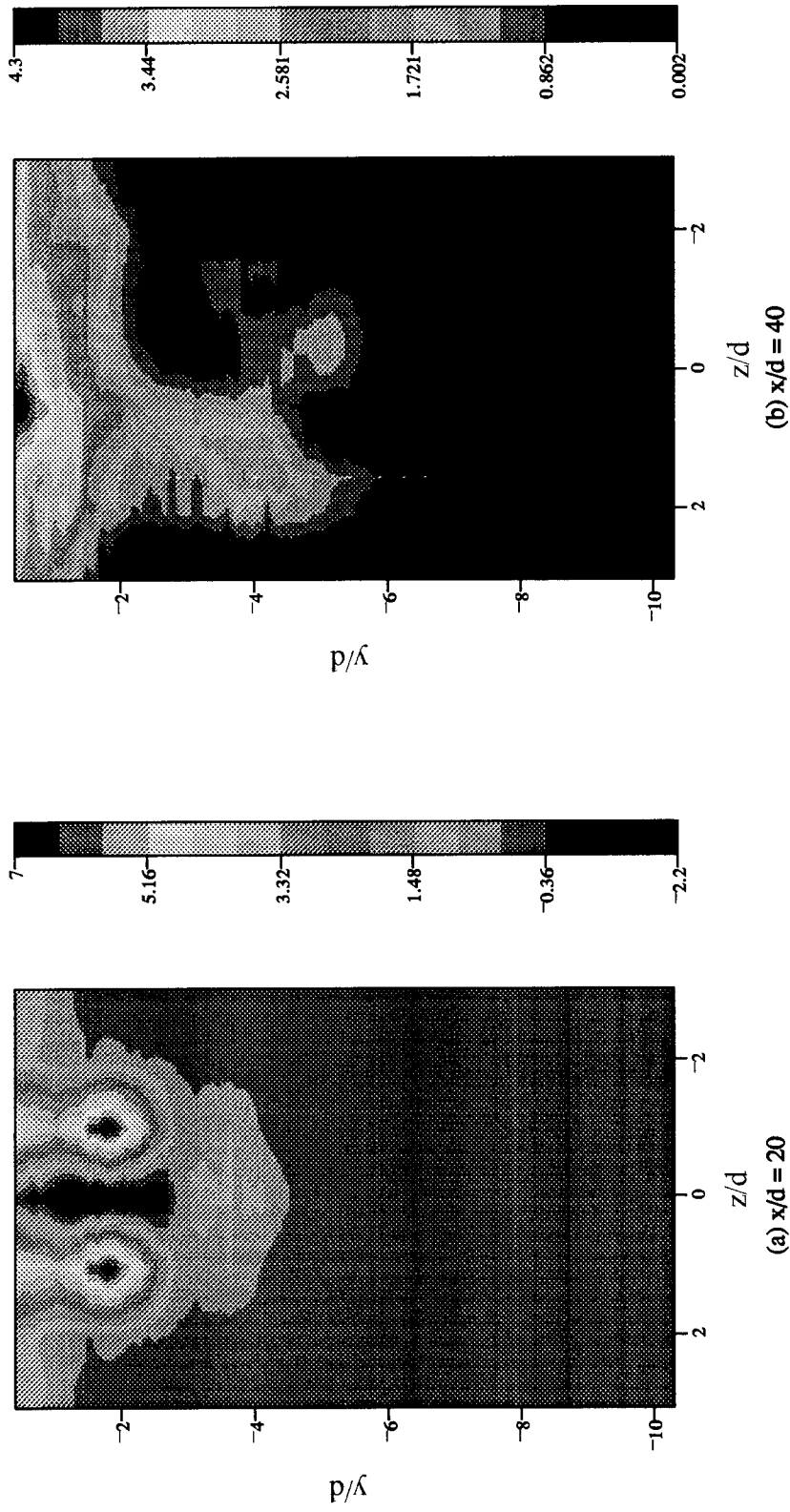
FIGURE 5.19: Separated Reynolds Shear $[-\rho u'w'/\rho u^2]$ (uw probe) (x10^3)
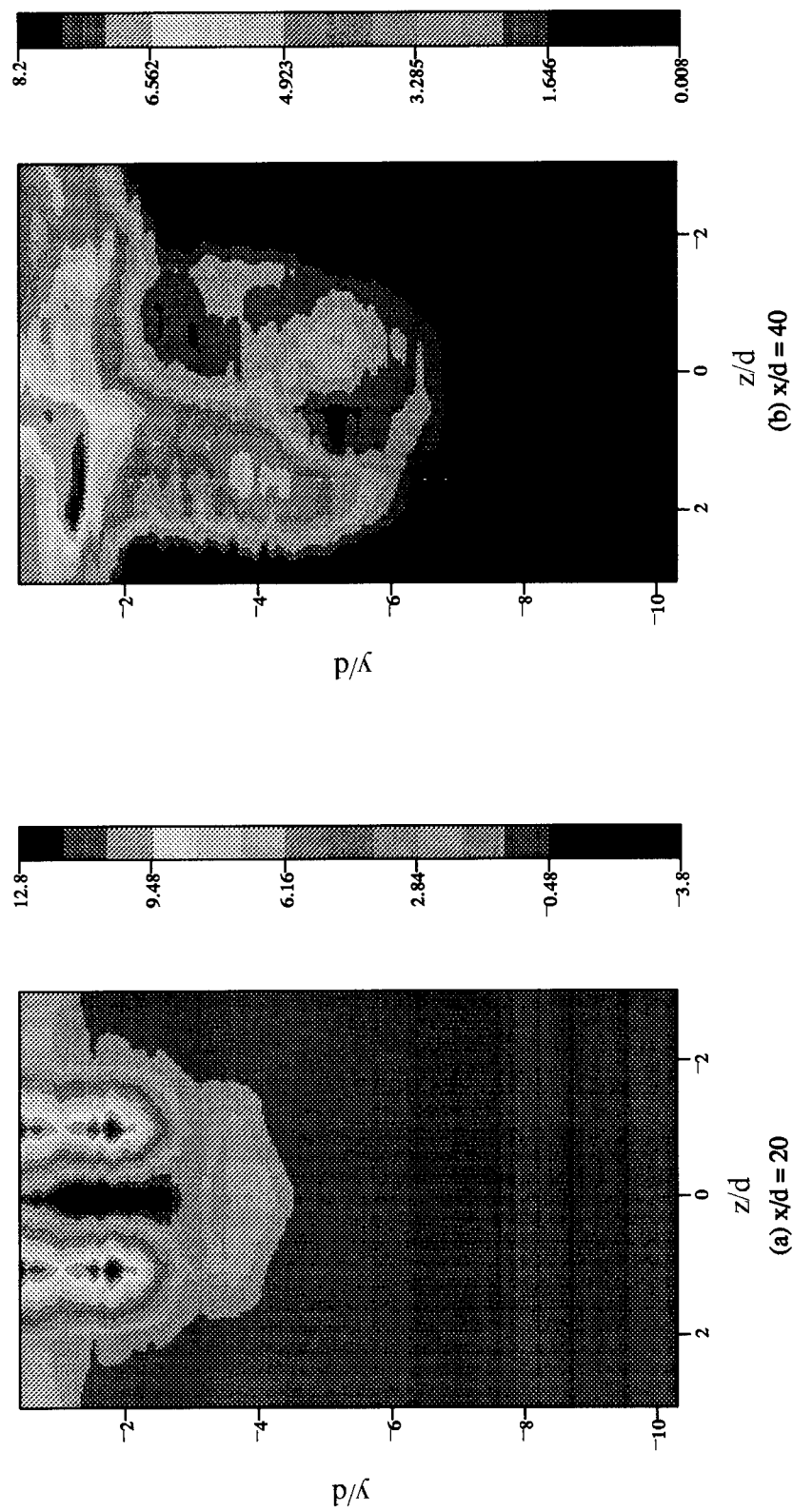
FIGURE 5.20: Separated Reynolds Shear $[-u\rho'w'/\rho u^2]$ (uw probe) (x10^3)
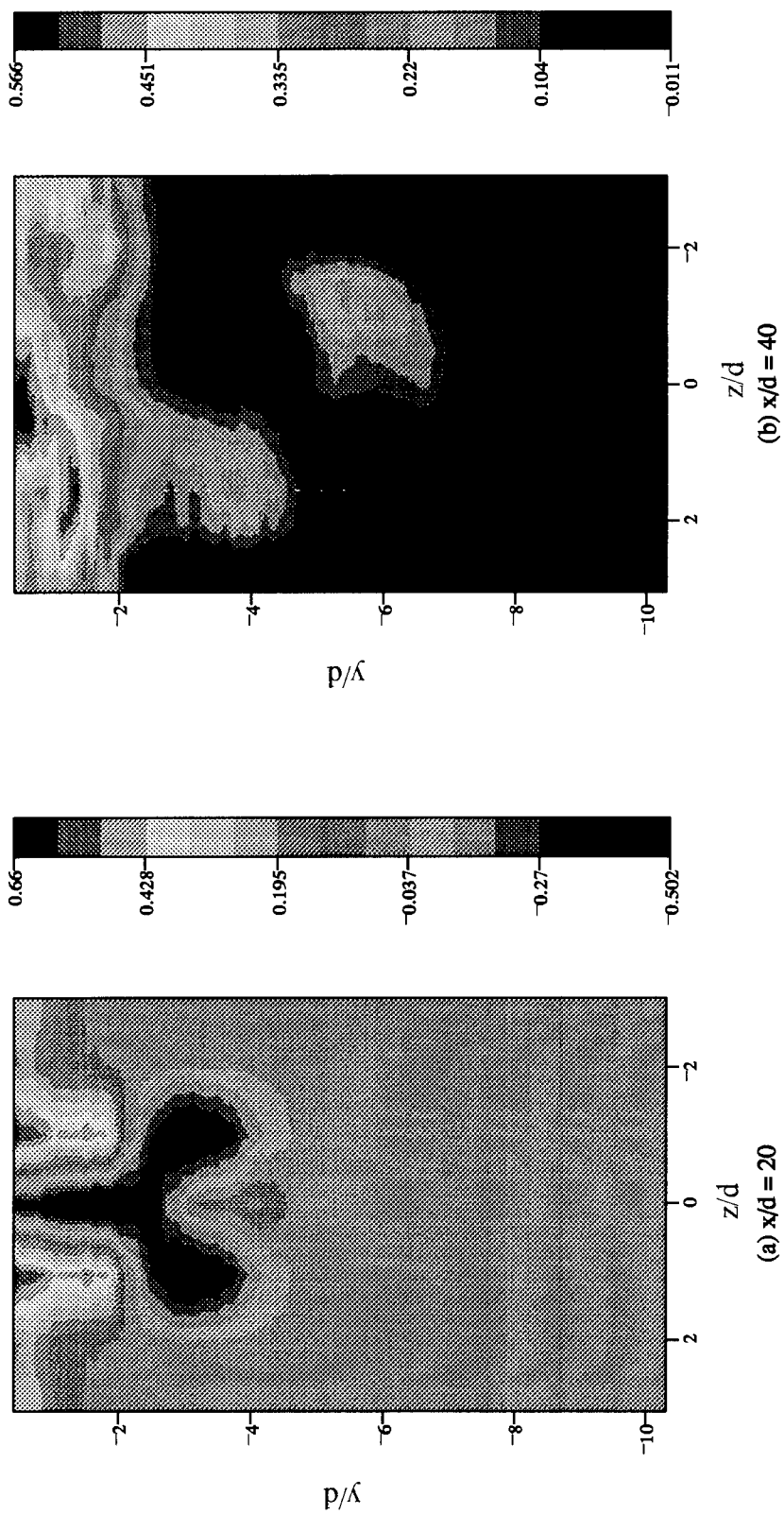
FIGURE 5.21: Separated Reynolds Shear [-wρ'u'/ρu²] (uw probe) (x10³)
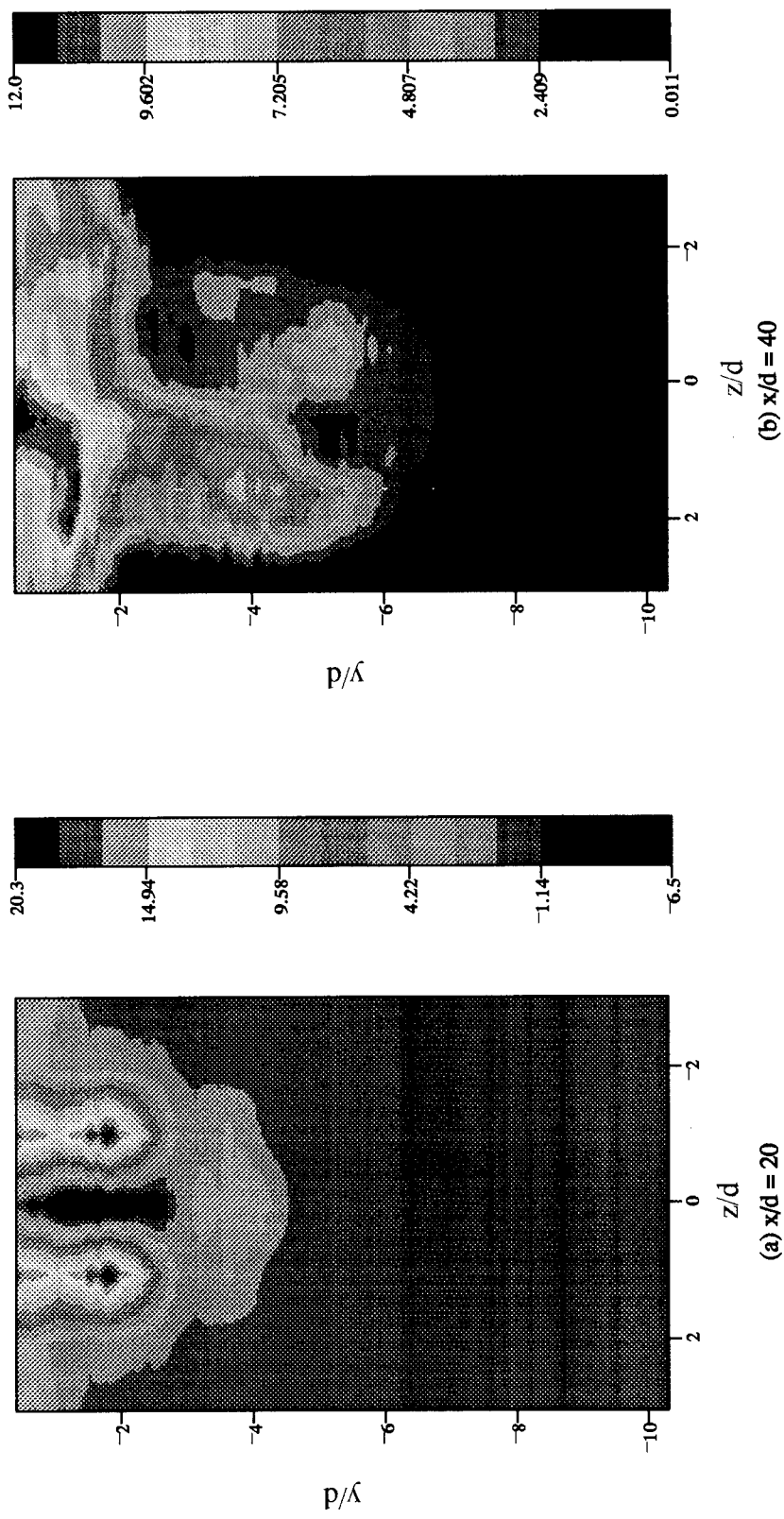
FIGURE 5.22: Separated Reynolds Shear [Reynolds Shear] (uw probe) (x10³)
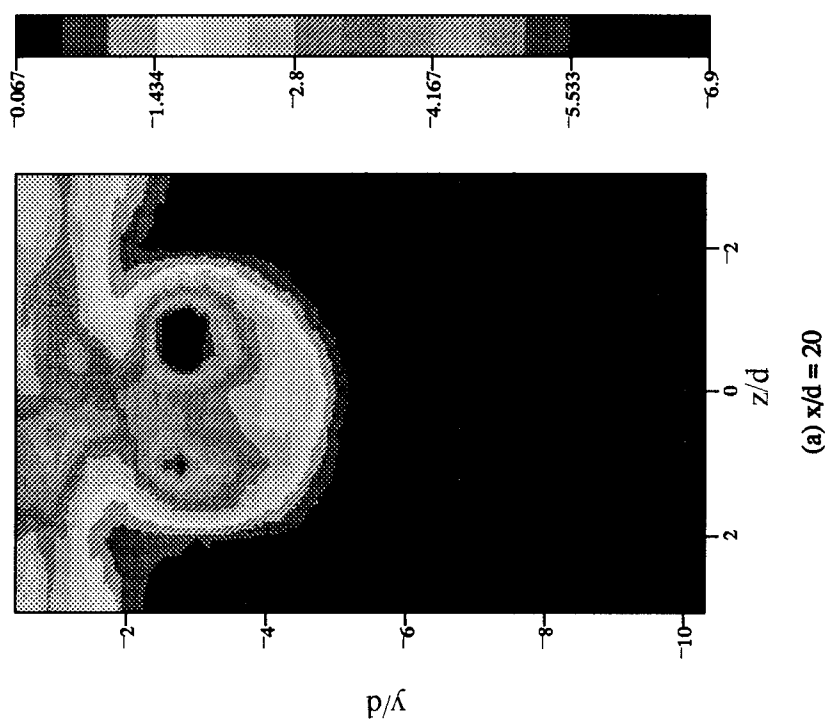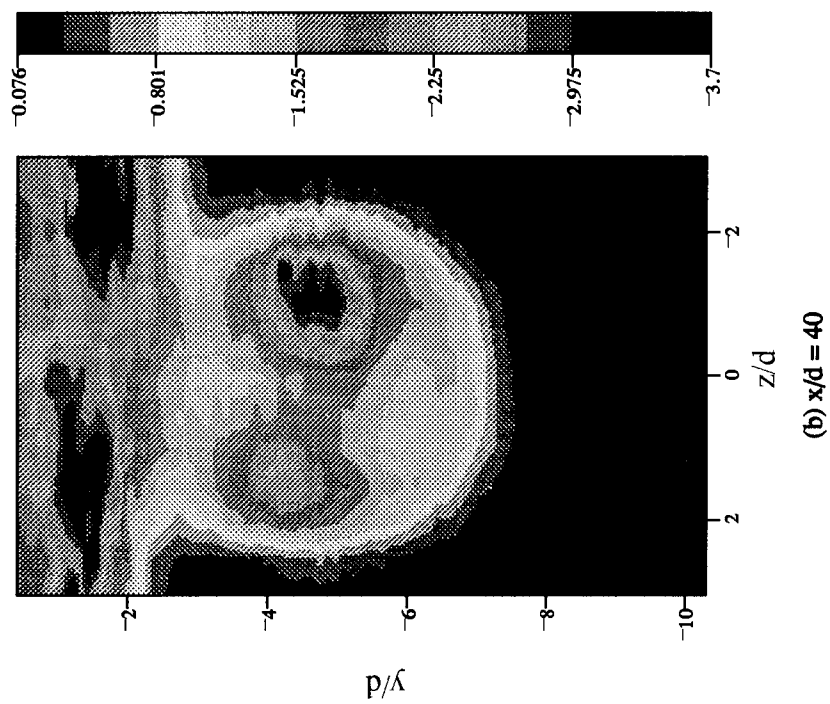
FIGURE 5.23: Favre Term [u"/U] (uv probe) (x10³)

60
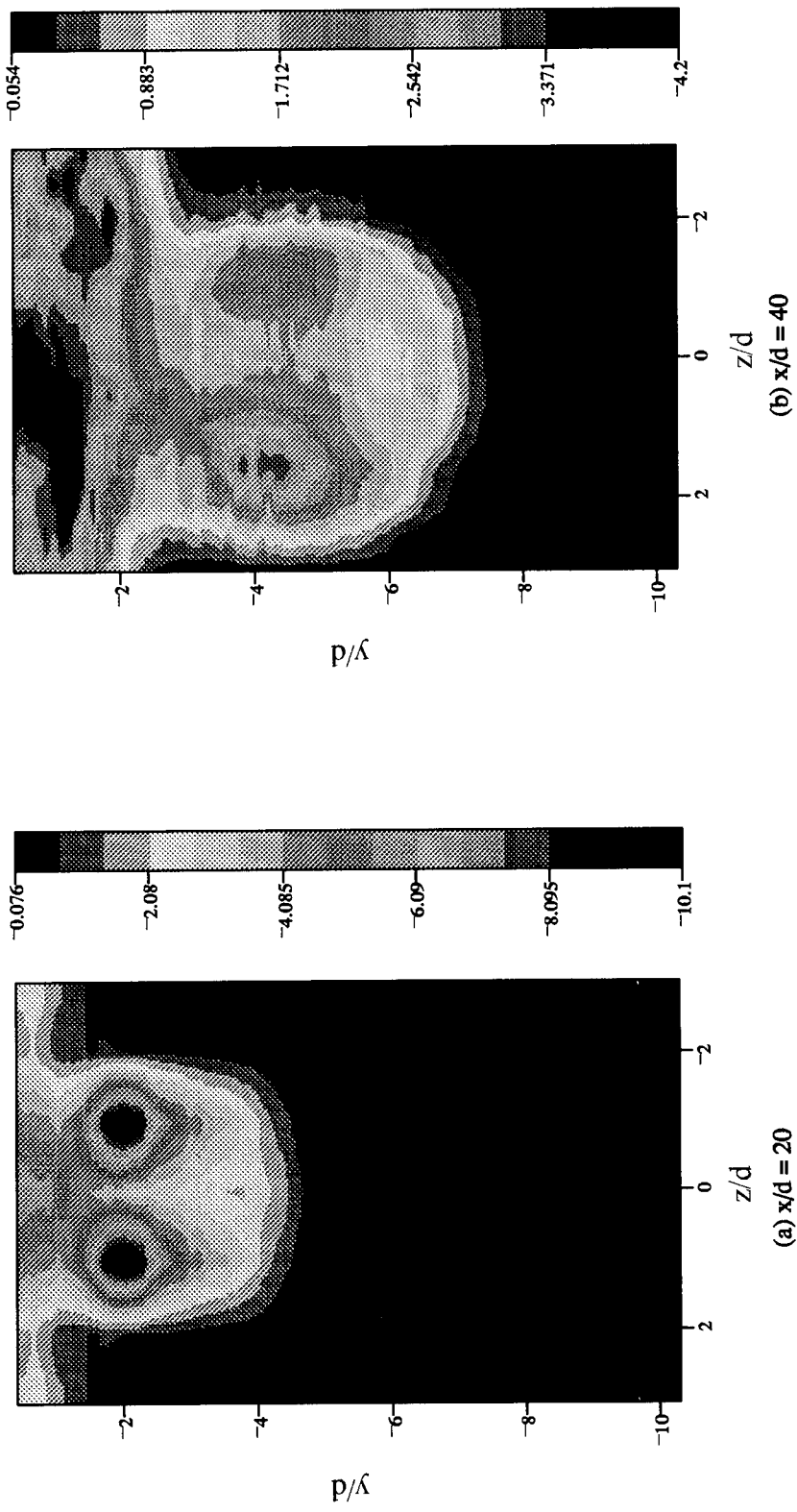
FIGURE 5.24: Favre Term [u"/U] (uw probe) (x10³)

61
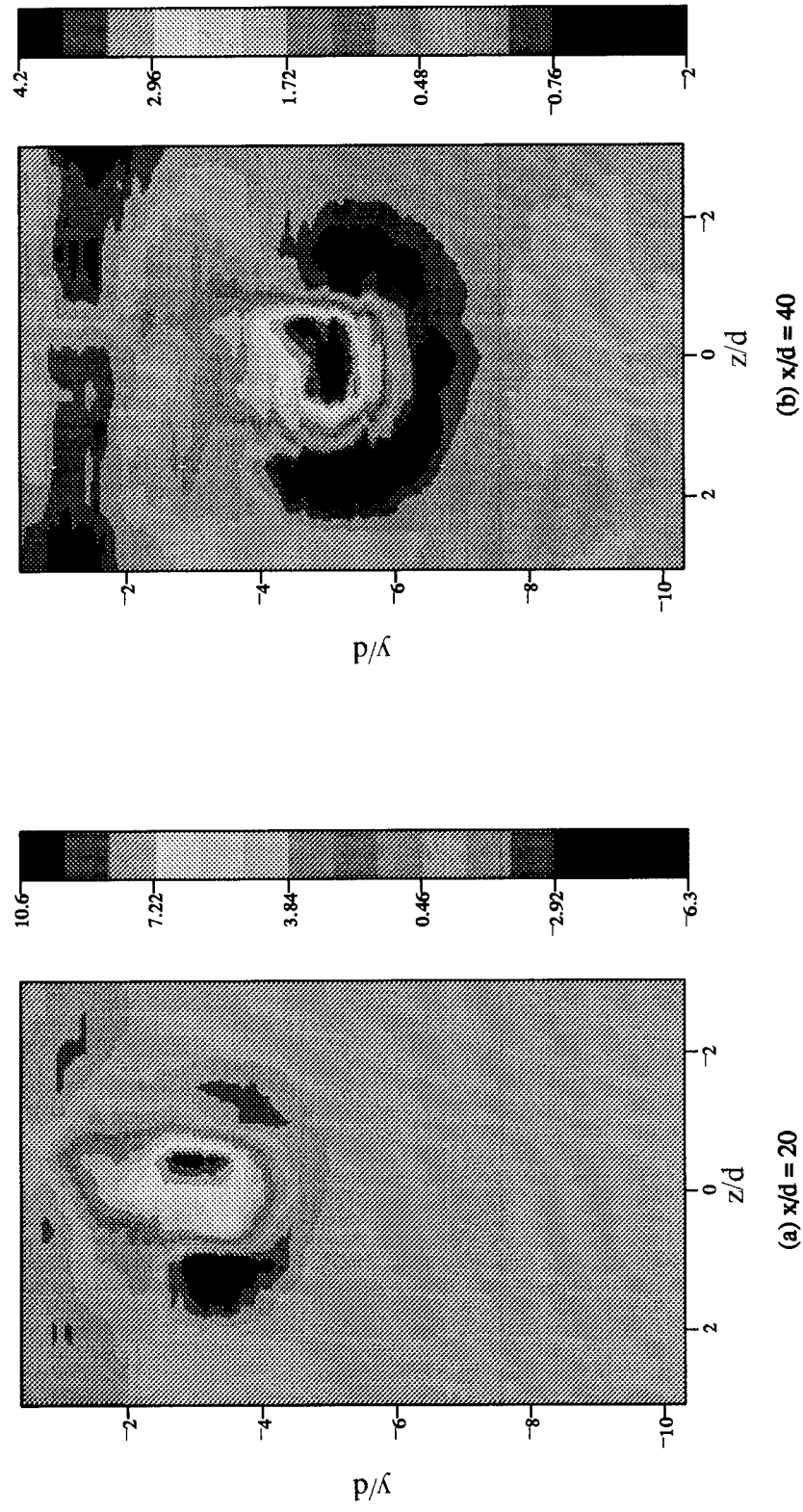
FIGURE 5.25: Favre Term [v"/U] (uv probe) (x10³)

62
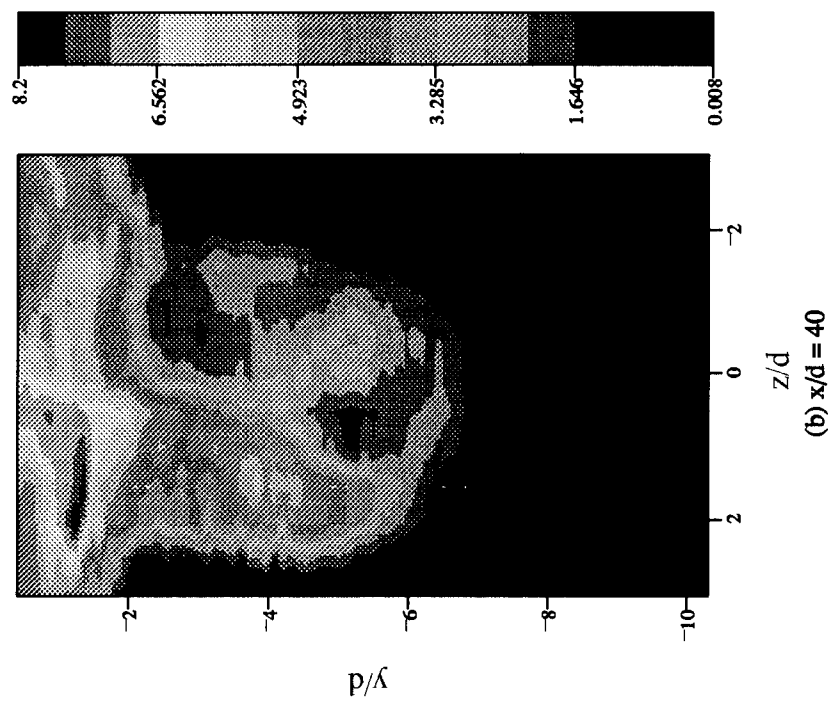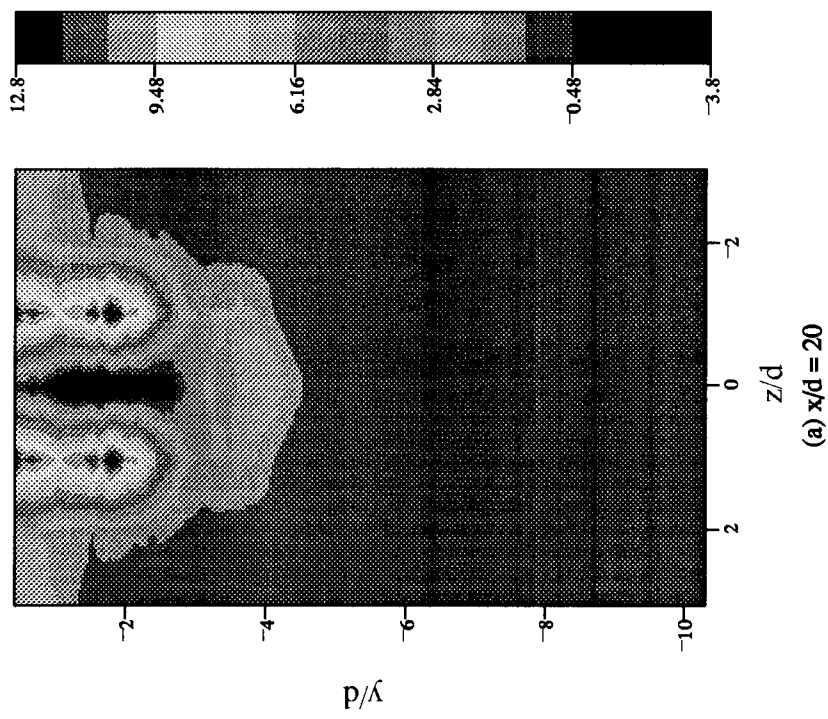
FIGURE 5.26: Favre Term [w''/U] (uw probe) (x10³)
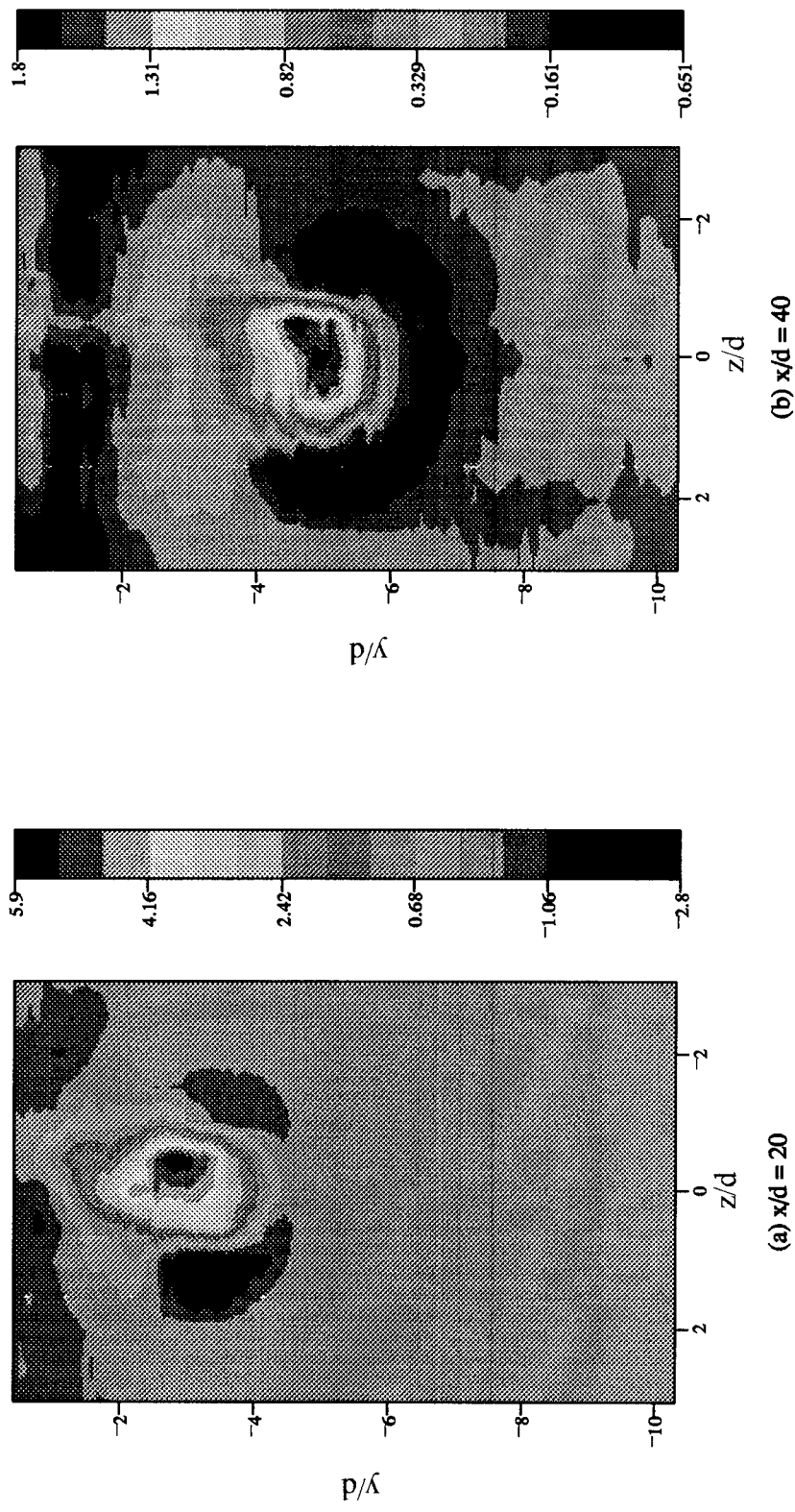
FIGURE 5.27: Favre Shear [ρu''v''/ρU²] (uv probe) (x10³)

(a) x/d = 20

(b) x/d = 40

64
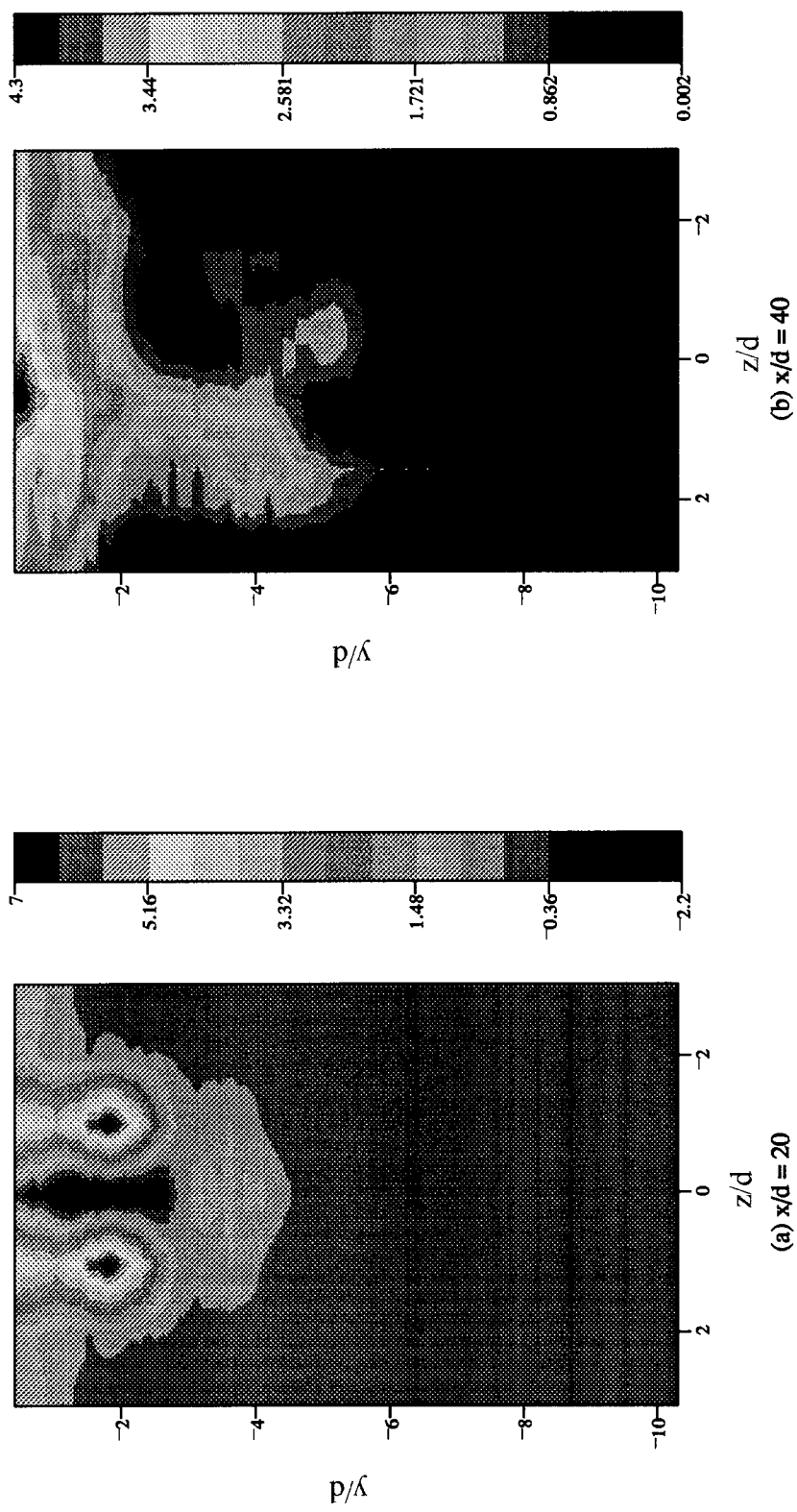
FIGURE 5.28: Favre Shear [$\rho u''w''/\rho U^2$] (uw probe) (x10^3)
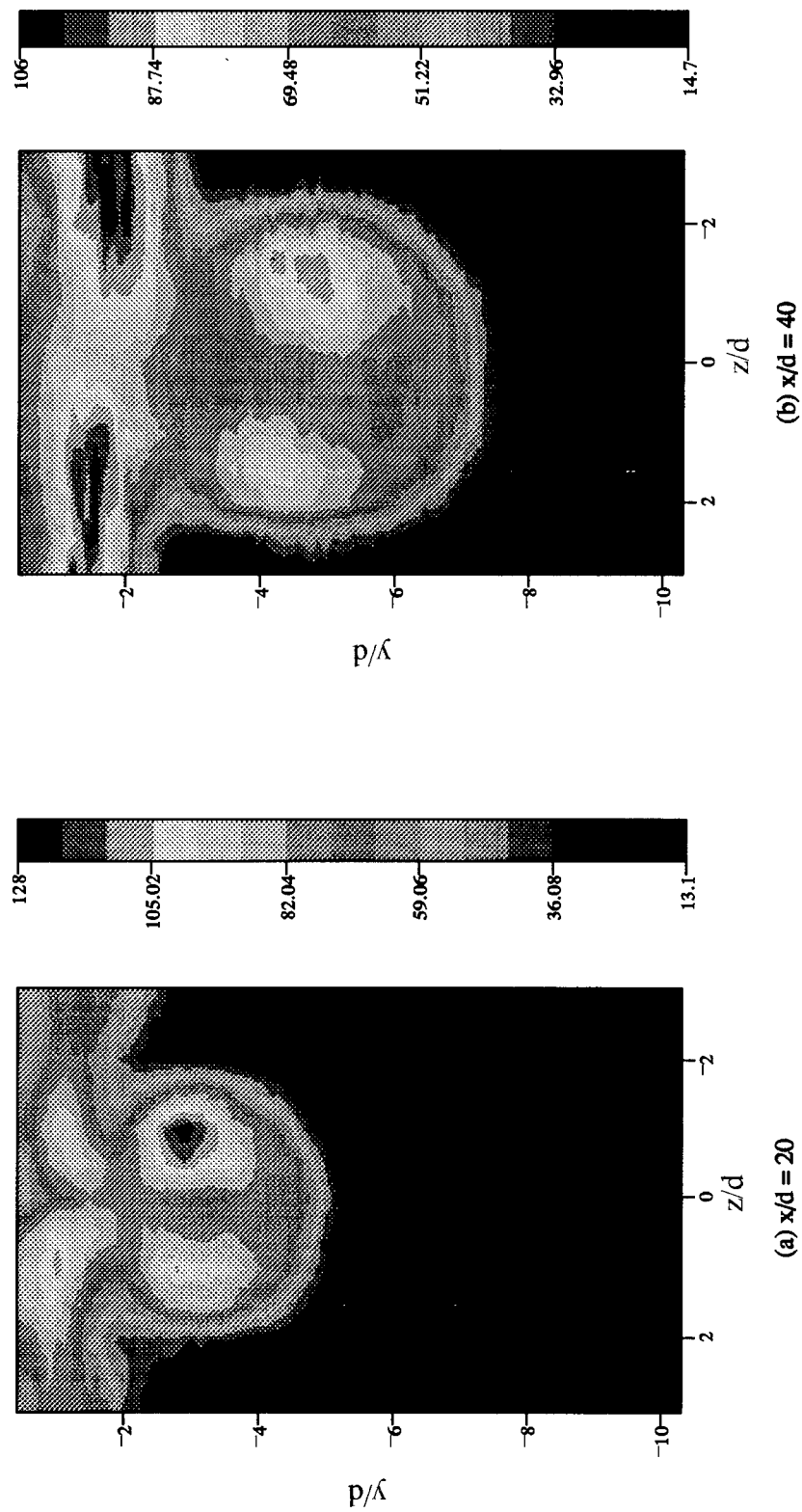
FIGURE 5.29: Separated Turbulence Intensity $[\rho'/\rho]_{rms}$ (uv probe) (x10³)
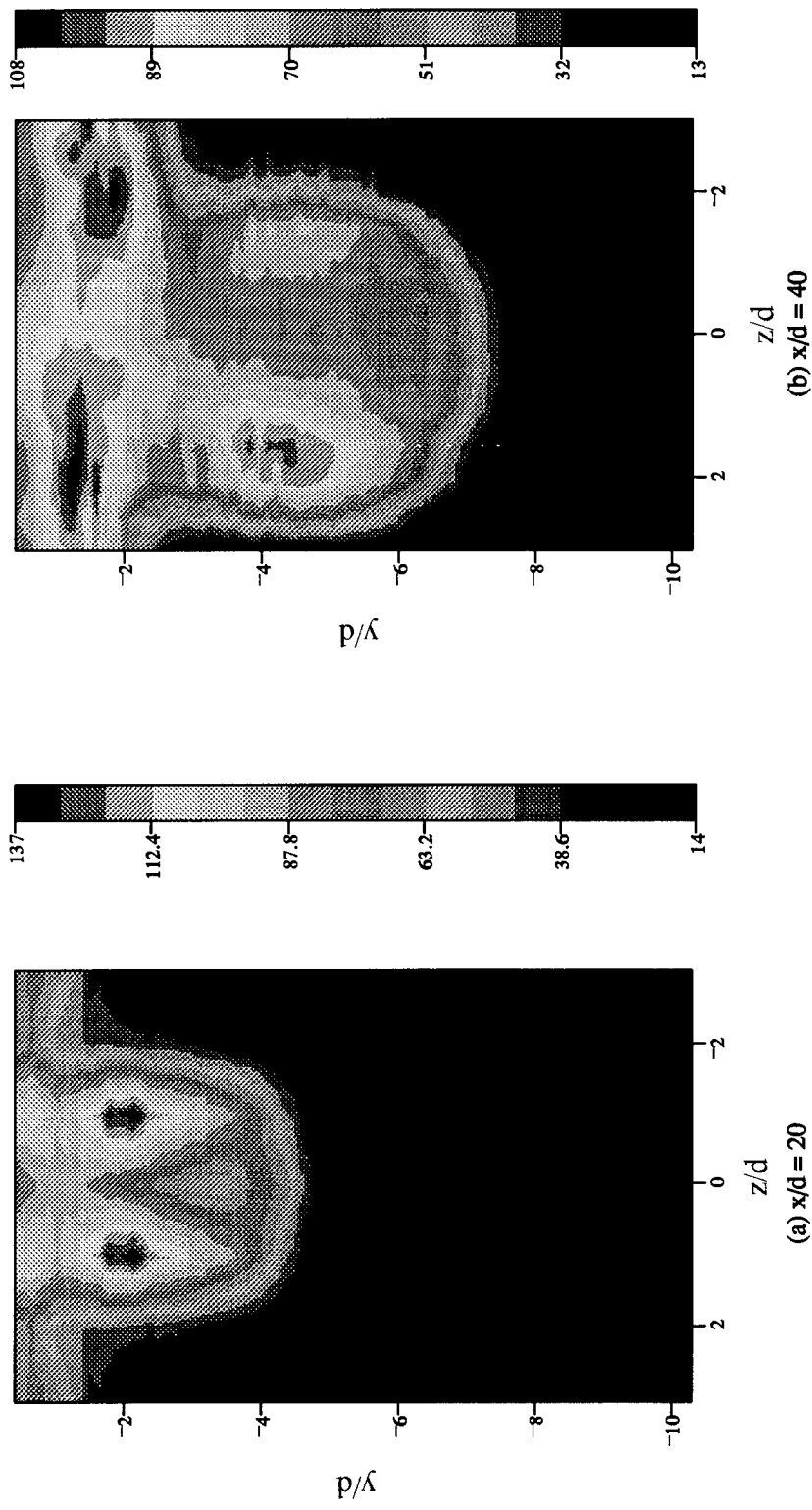
FIGURE 5.30: Separated Turbulence Intensity $[\rho'/\rho]_{rms}$ (uw probe) (x10^3)
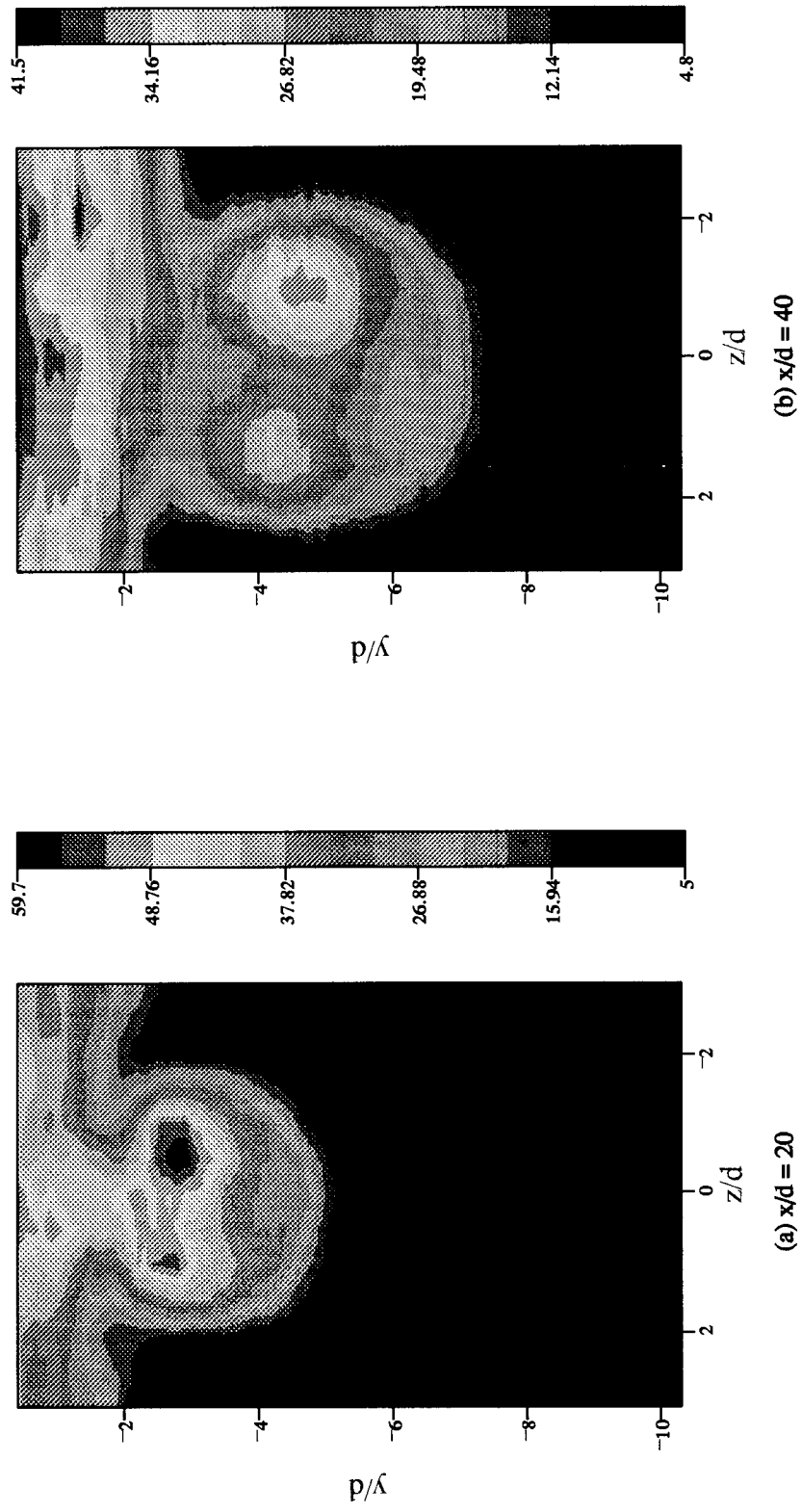
FIGURE 5.31: Separated Turbulence Intensity $[u'/u]_{rms}$ (uv probe) $(\times 10^3)$

(a) x/d = 20

(b) x/d = 40
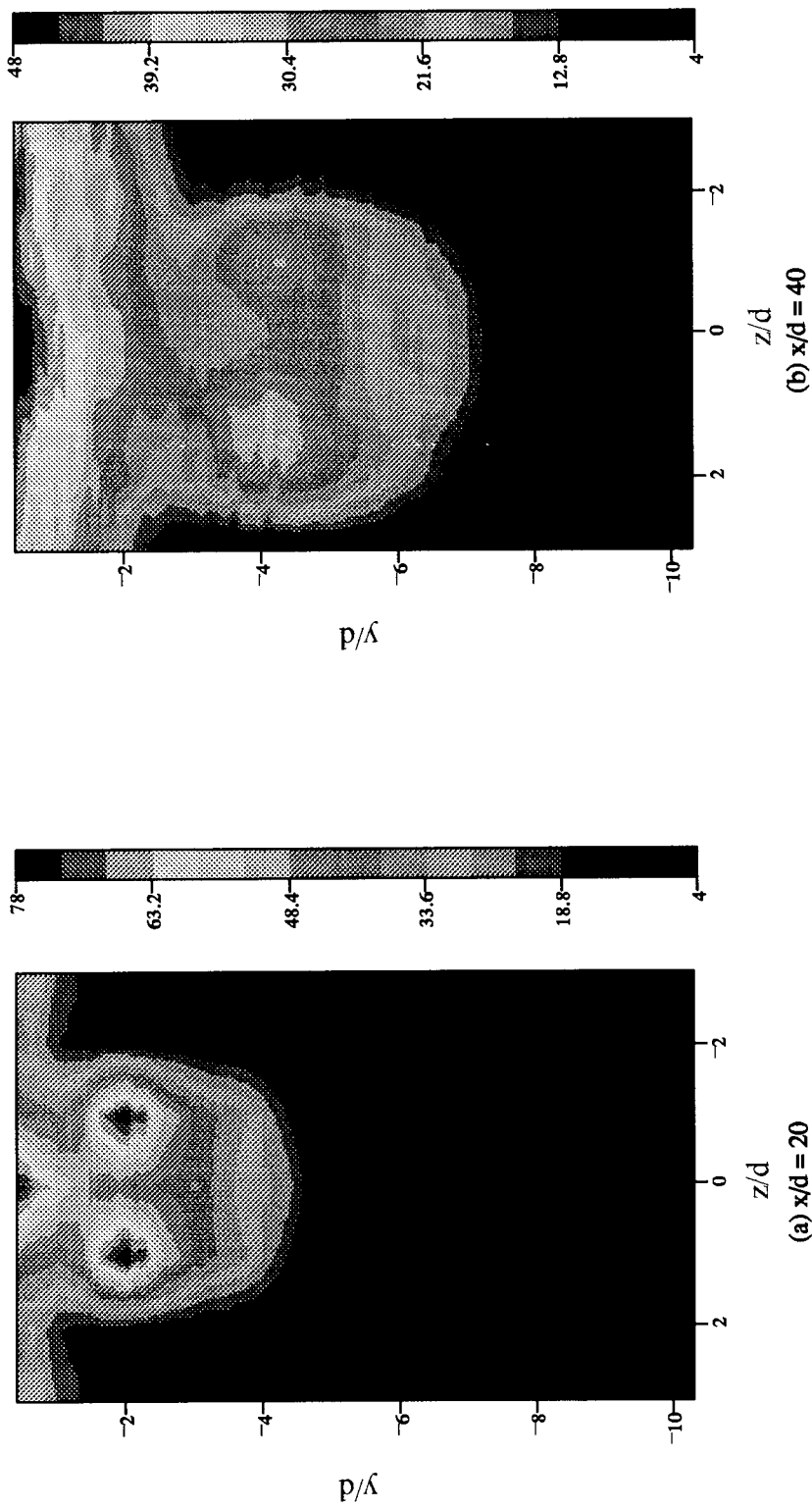
FIGURE 5.32: Separated Turbulence Intensity $[u'/u]_{rms}$ (uw probe) (x10³)

(a) x/d = 20

(b) x/d = 40
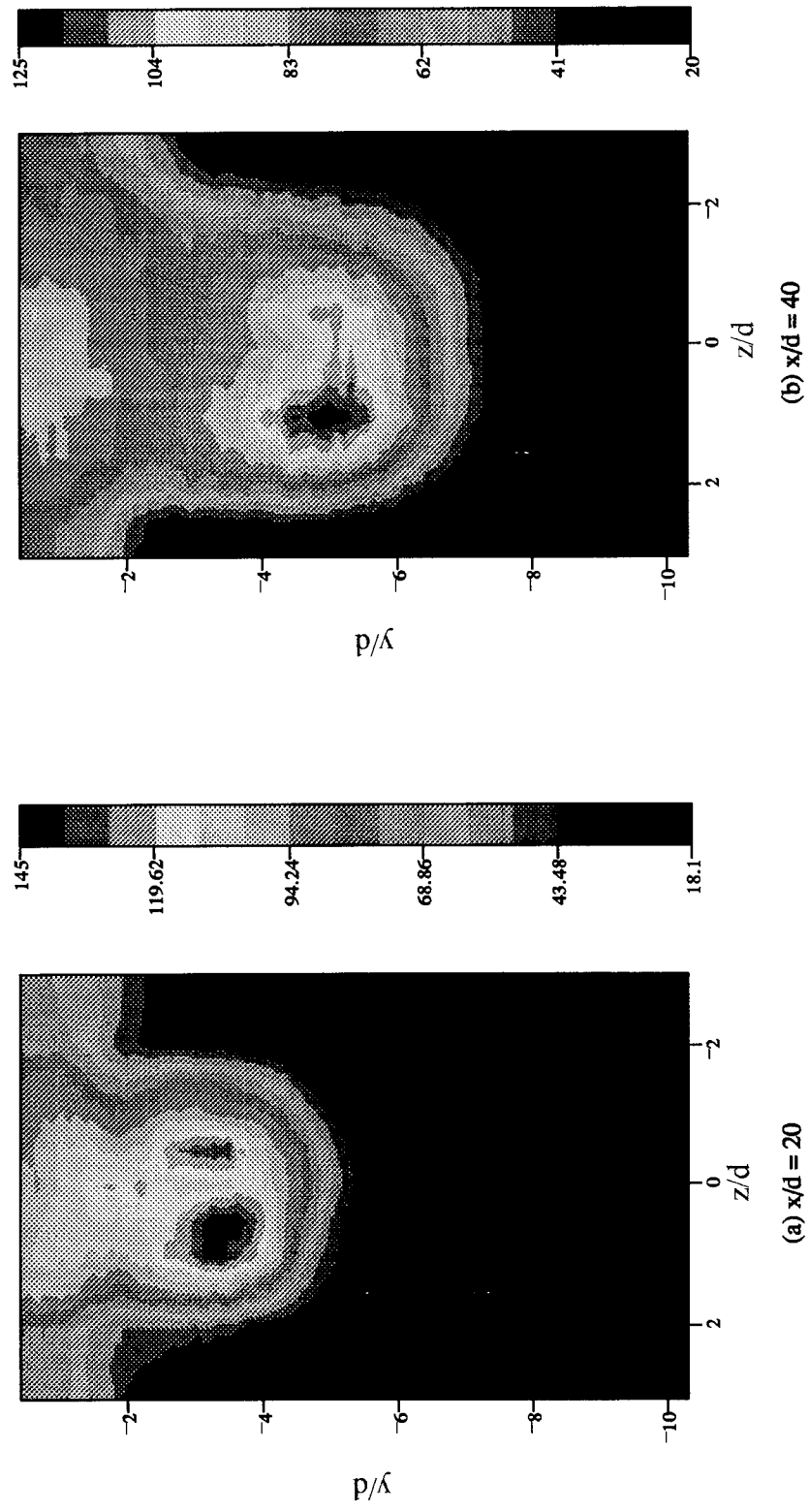
FIGURE 5.33: Separated Turbulence Intensity $[v'/u]_{rms}$ (uv probe) $(x10^3)$
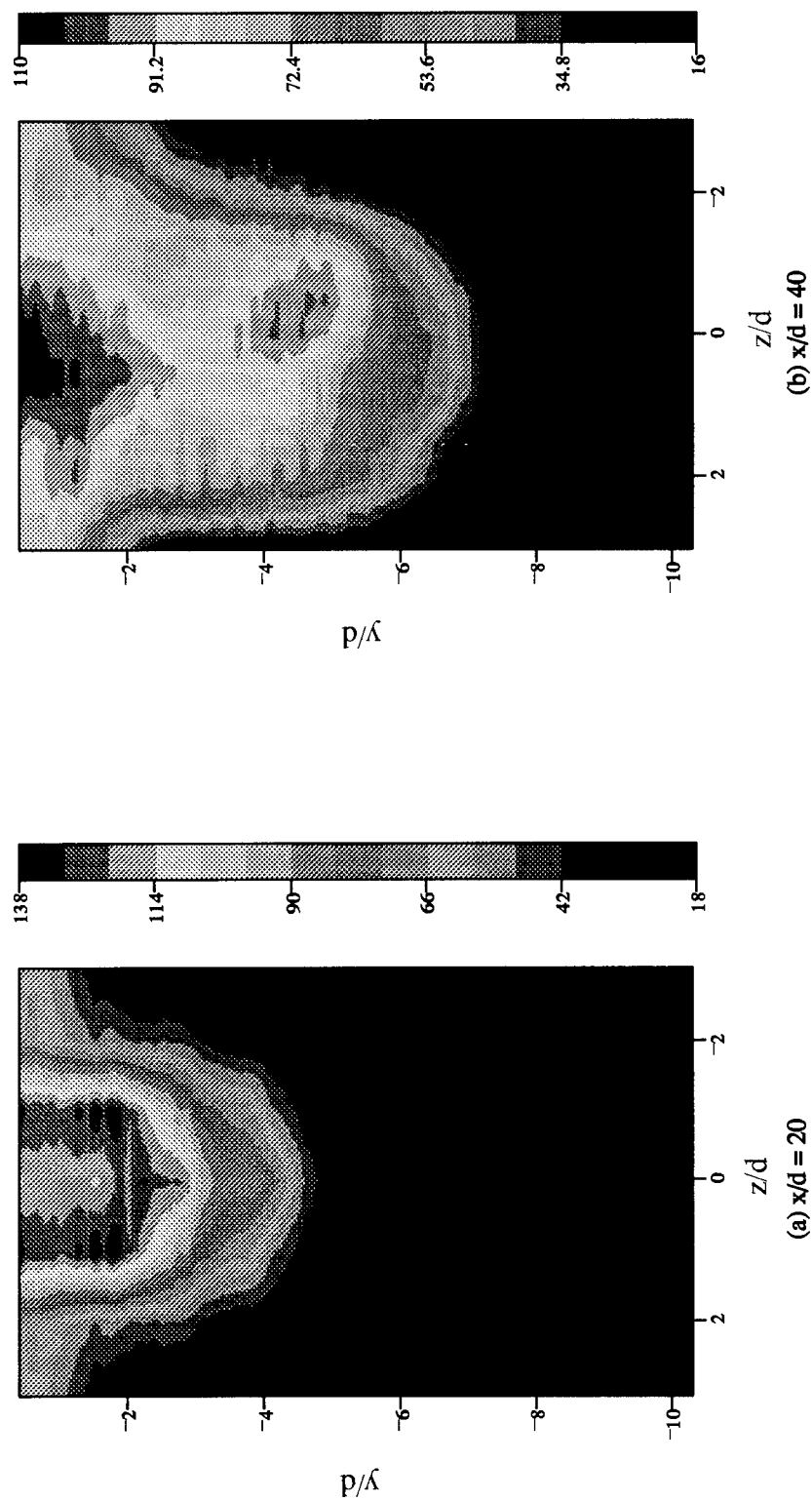
FIGURE 5.34: Separated Turbulence Intensity $[w'/u]_{rms}$ (uw probe) ($\times 10^3$)
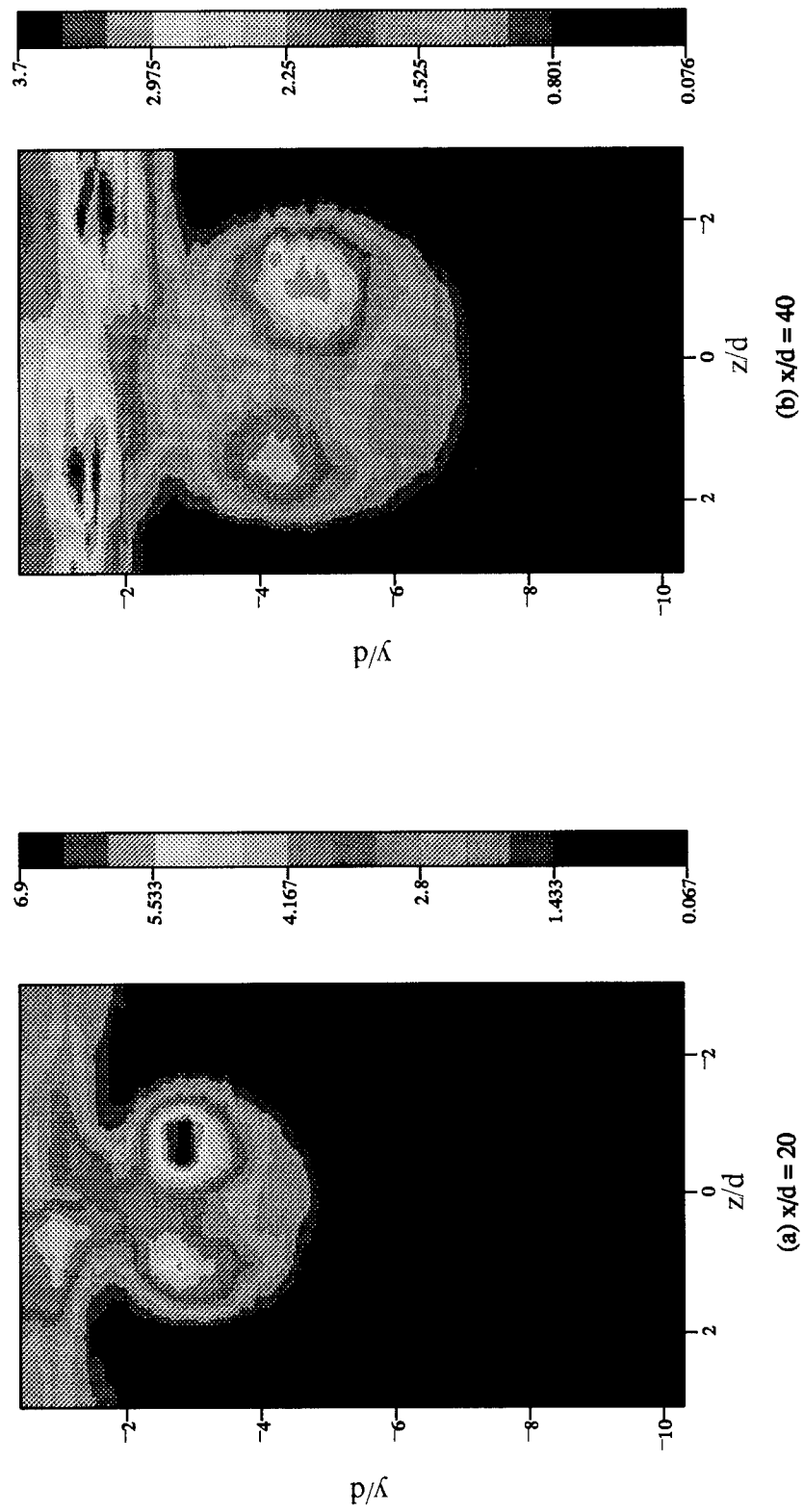
FIGURE 5.35: Velocity-Velocity Correlation [(u'v')/u²] (uv probe) (x10³)
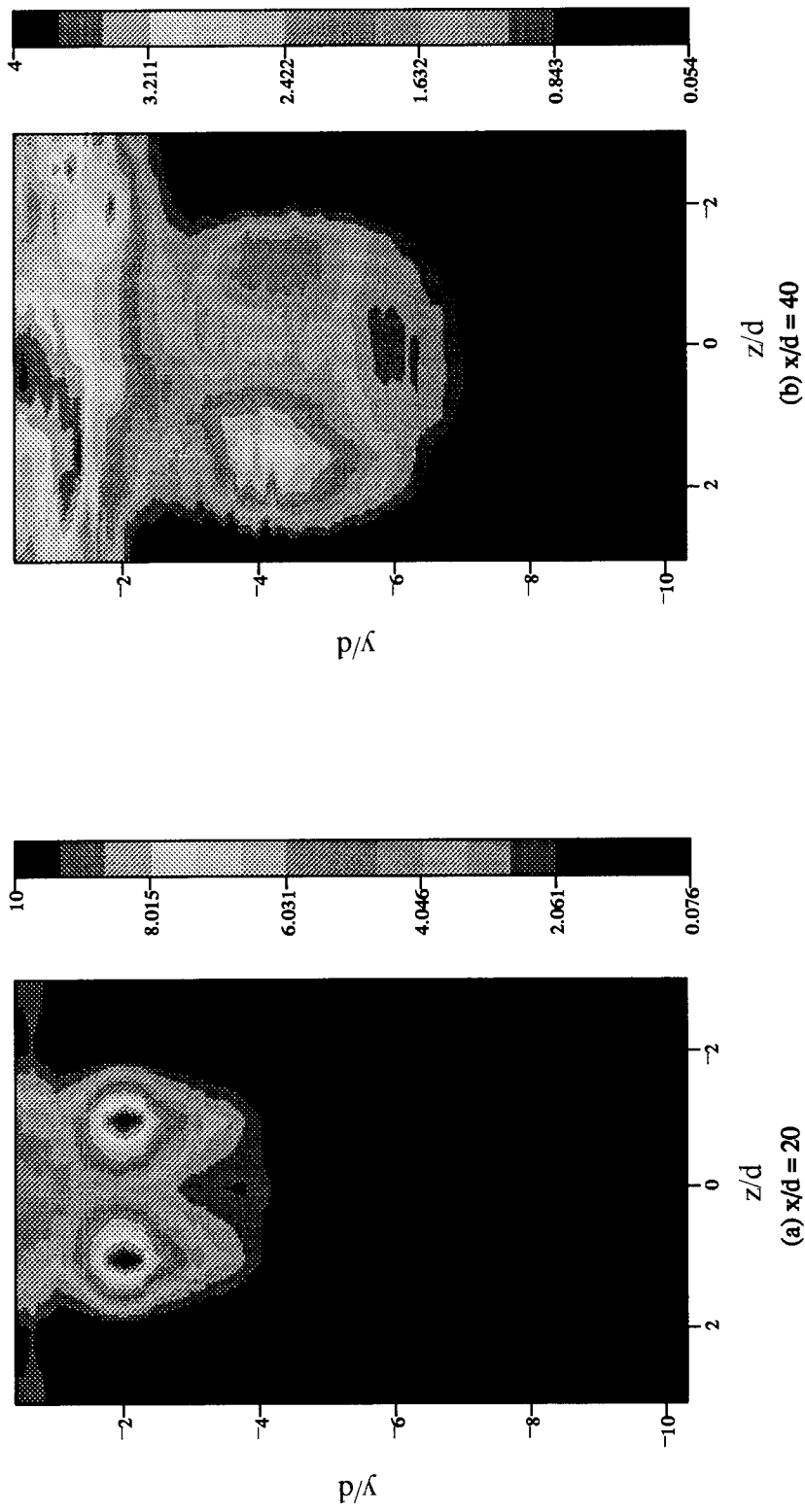
FIGURE 5.36: Velocity-Velocity Correlation [(u'w')/u²] (uw probe) (x10³)
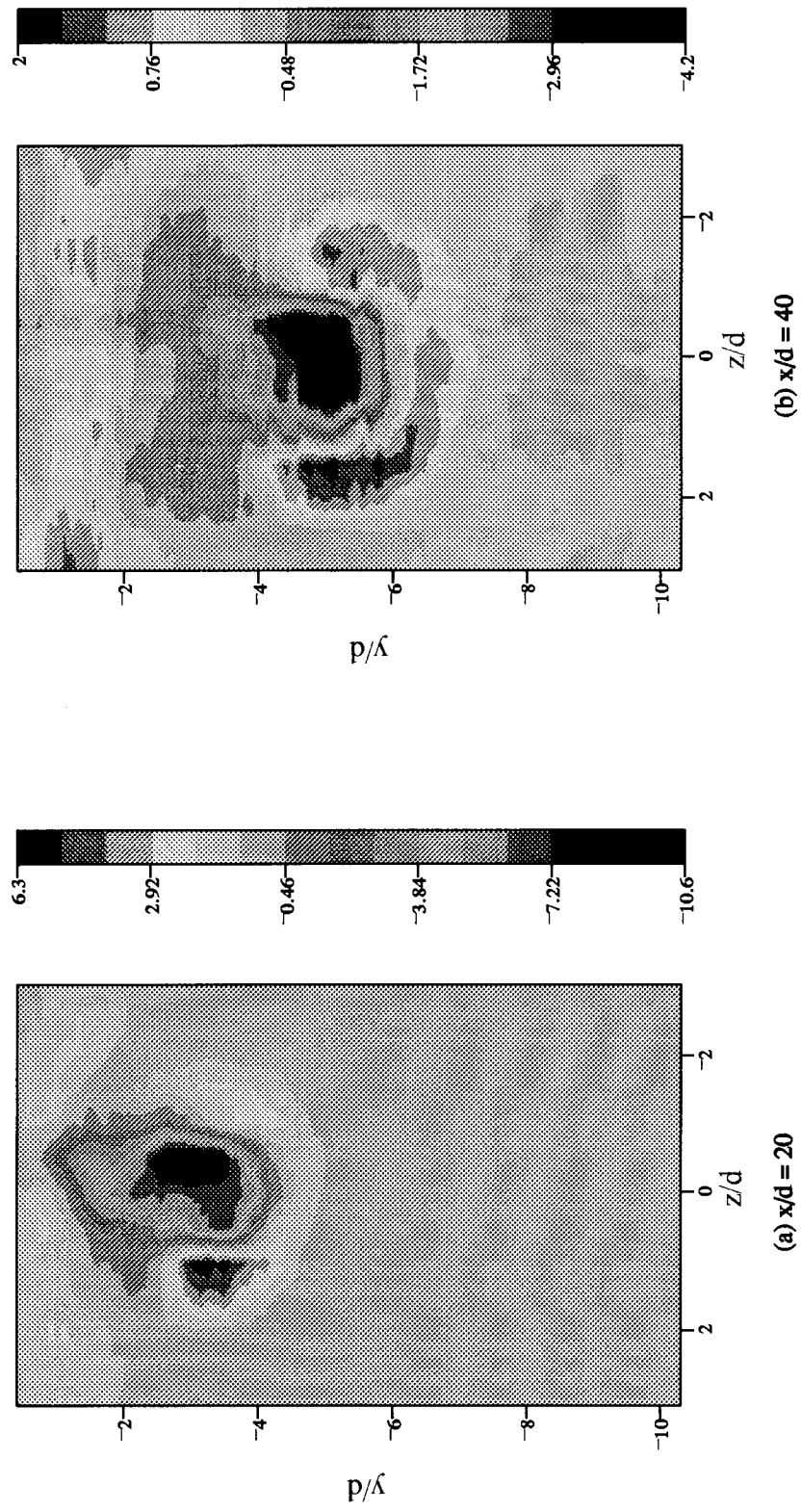
FIGURE 5.37: Density-Velocity Correlation [(ρ'u')/ρu] (uv probe) (x10³)
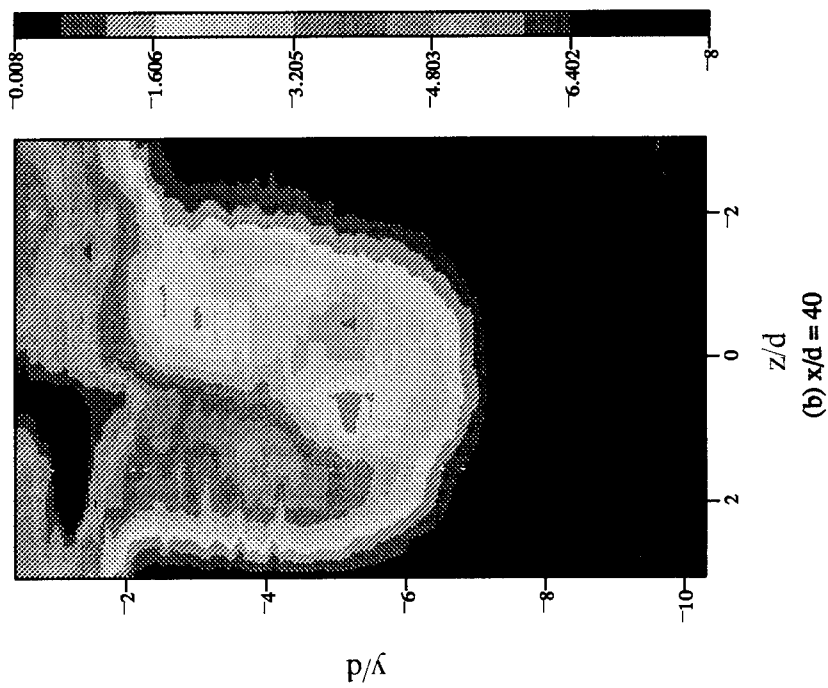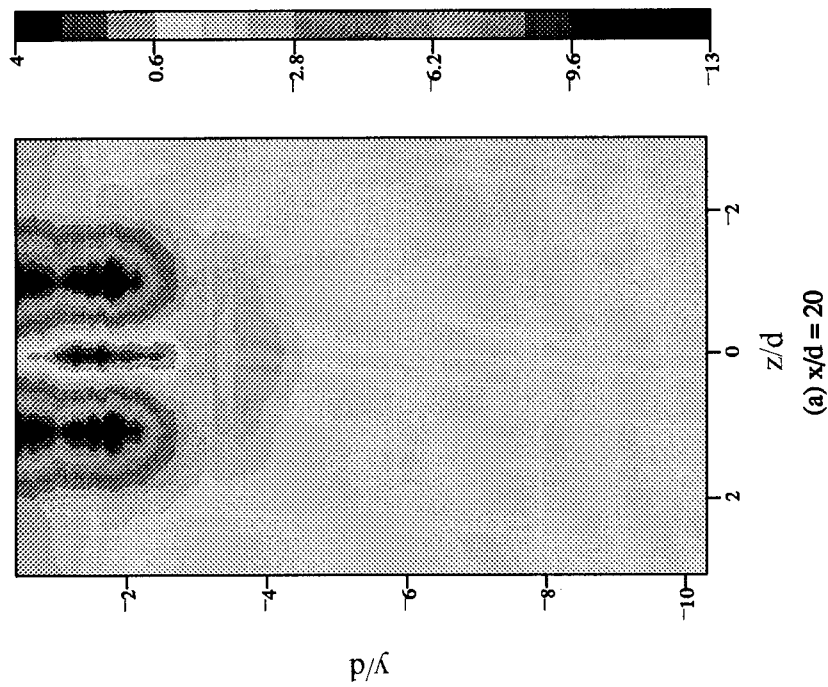
FIGURE 5.38: Density-Velocity Correlation $[(\rho'u')/\overline{\rho u}]$ (uw probe) $(\times 10^3)$
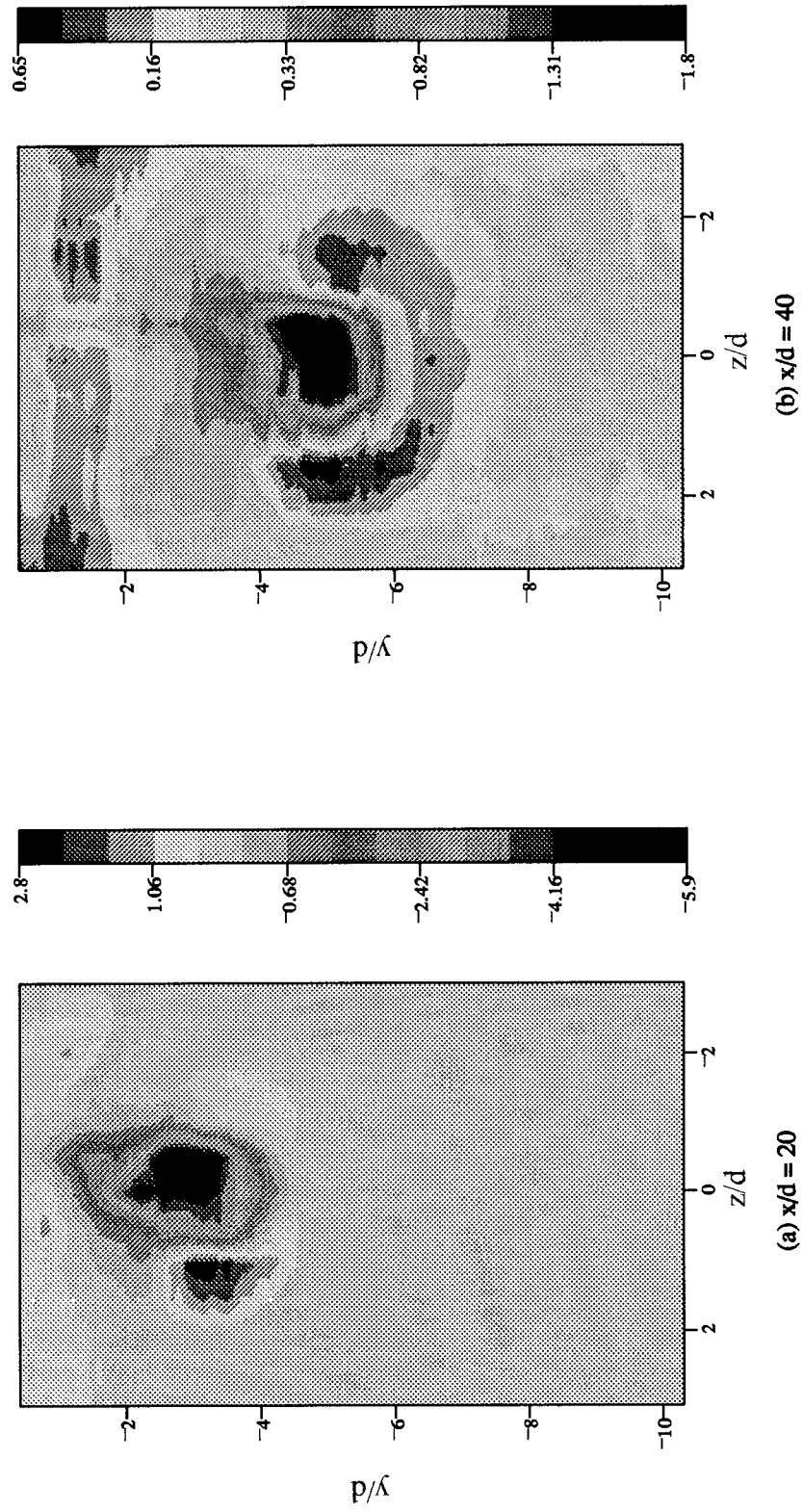
FIGURE 5.39: Density-Velocity Correlation [(ρ'v')/ρu] (uv probe) (x10³)
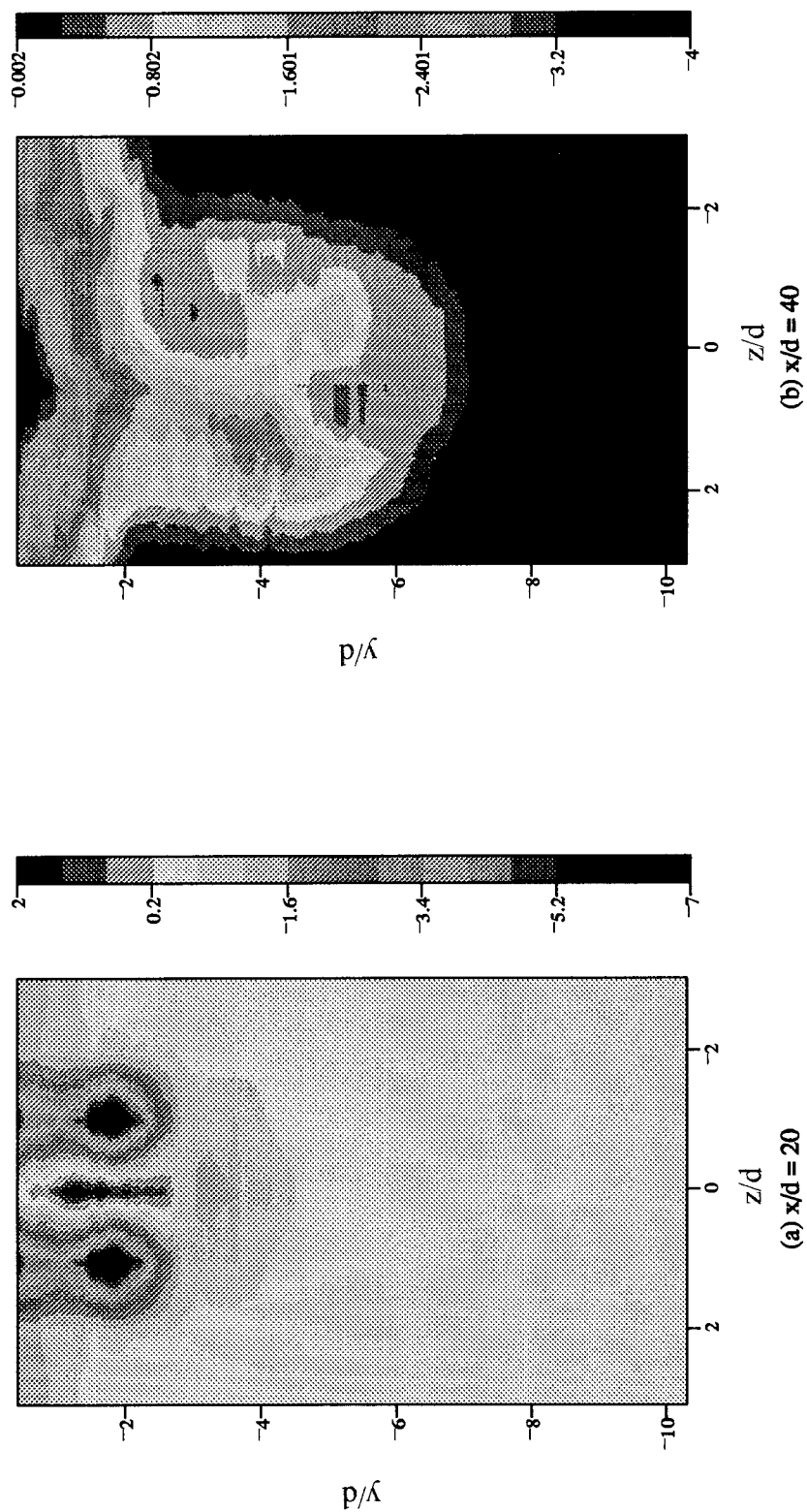
FIGURE 5.40: Density-Velocity Correlation [(ρ'w')/ρu] (uw probe) (x10³)
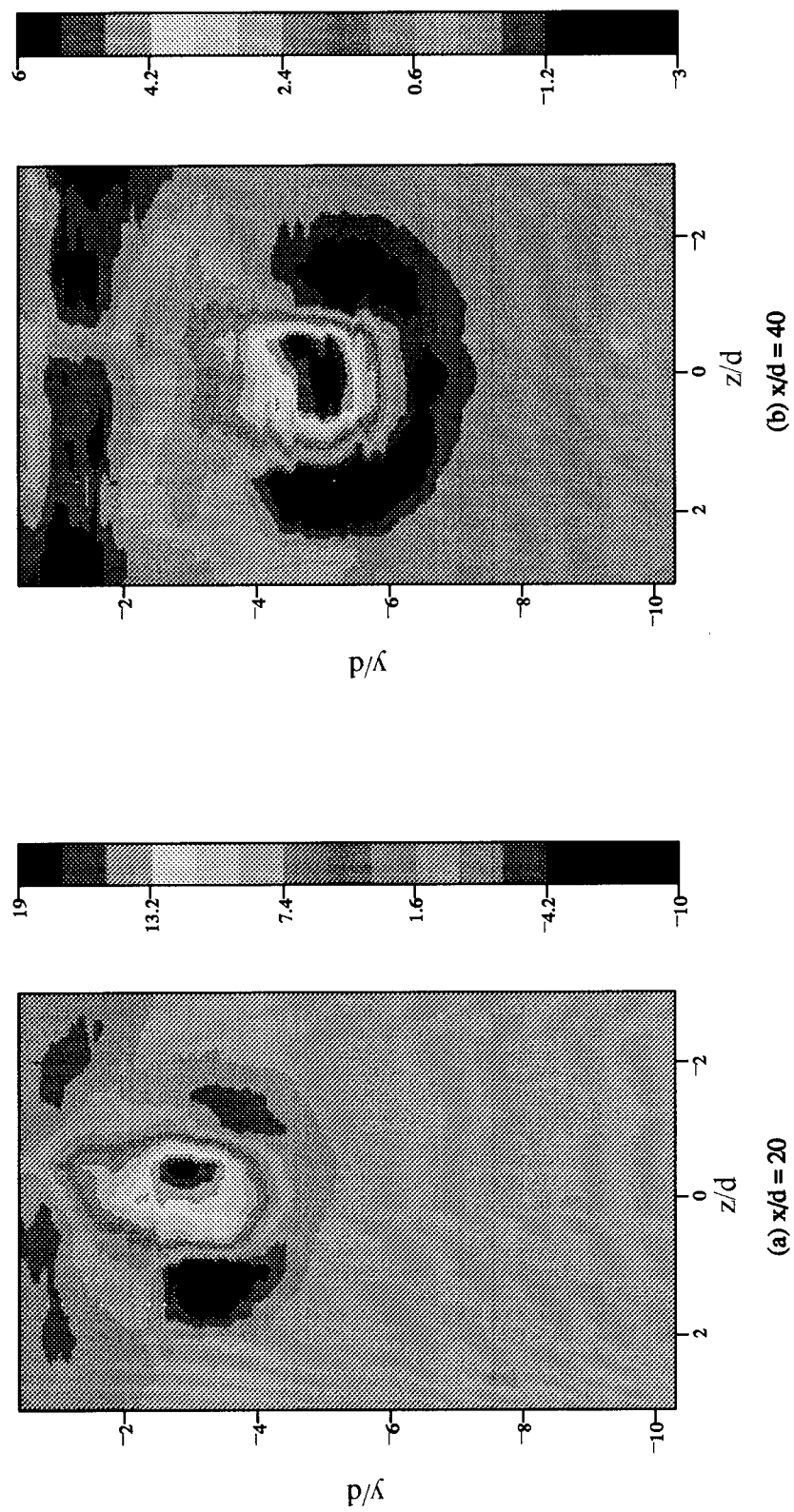
FIGURE 5.41: Transformed Shear $[(\rho u)'(\rho v)'/(\rho u^2)]$ (uv probe) $(\times 10^3)$
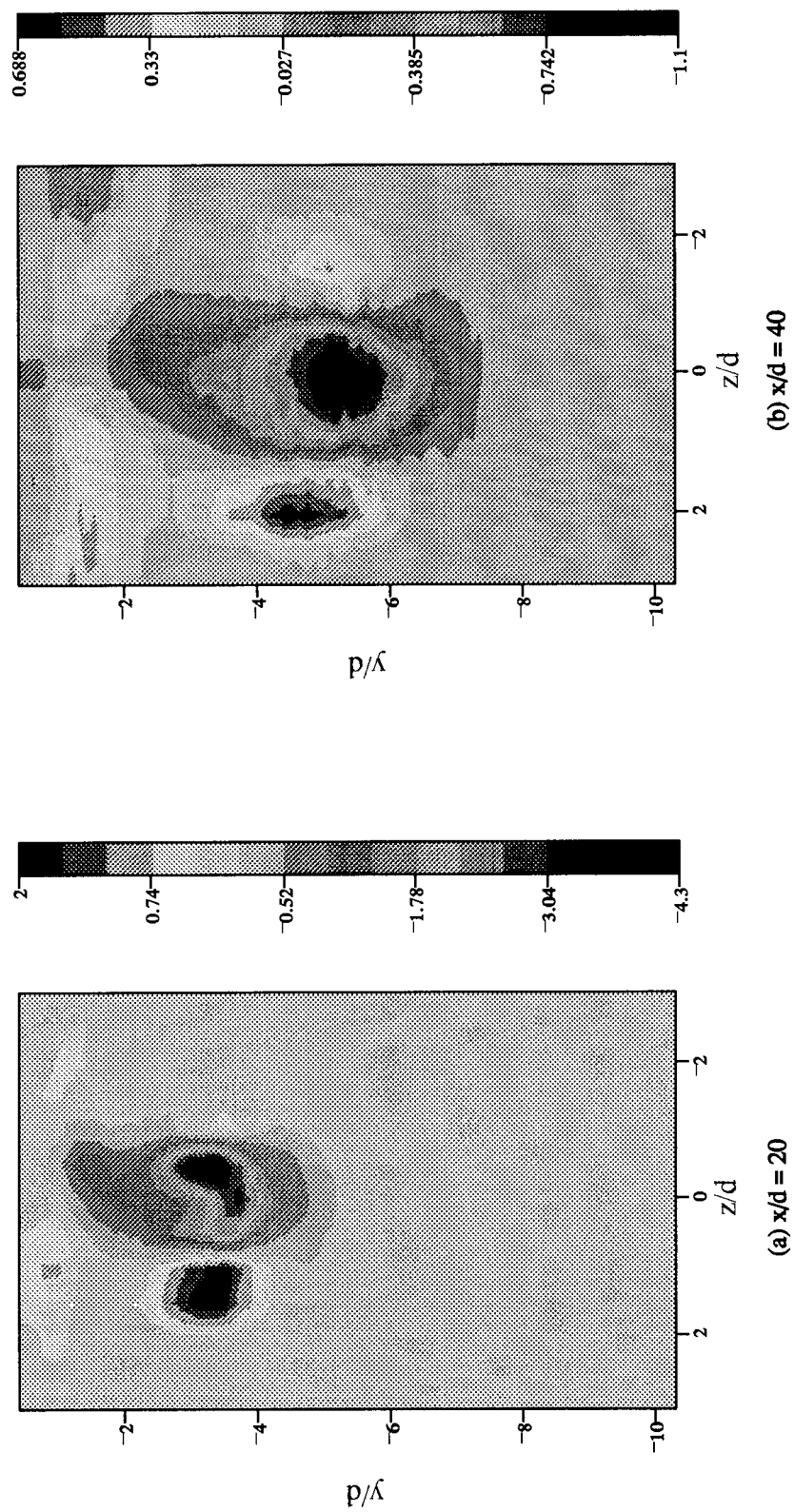
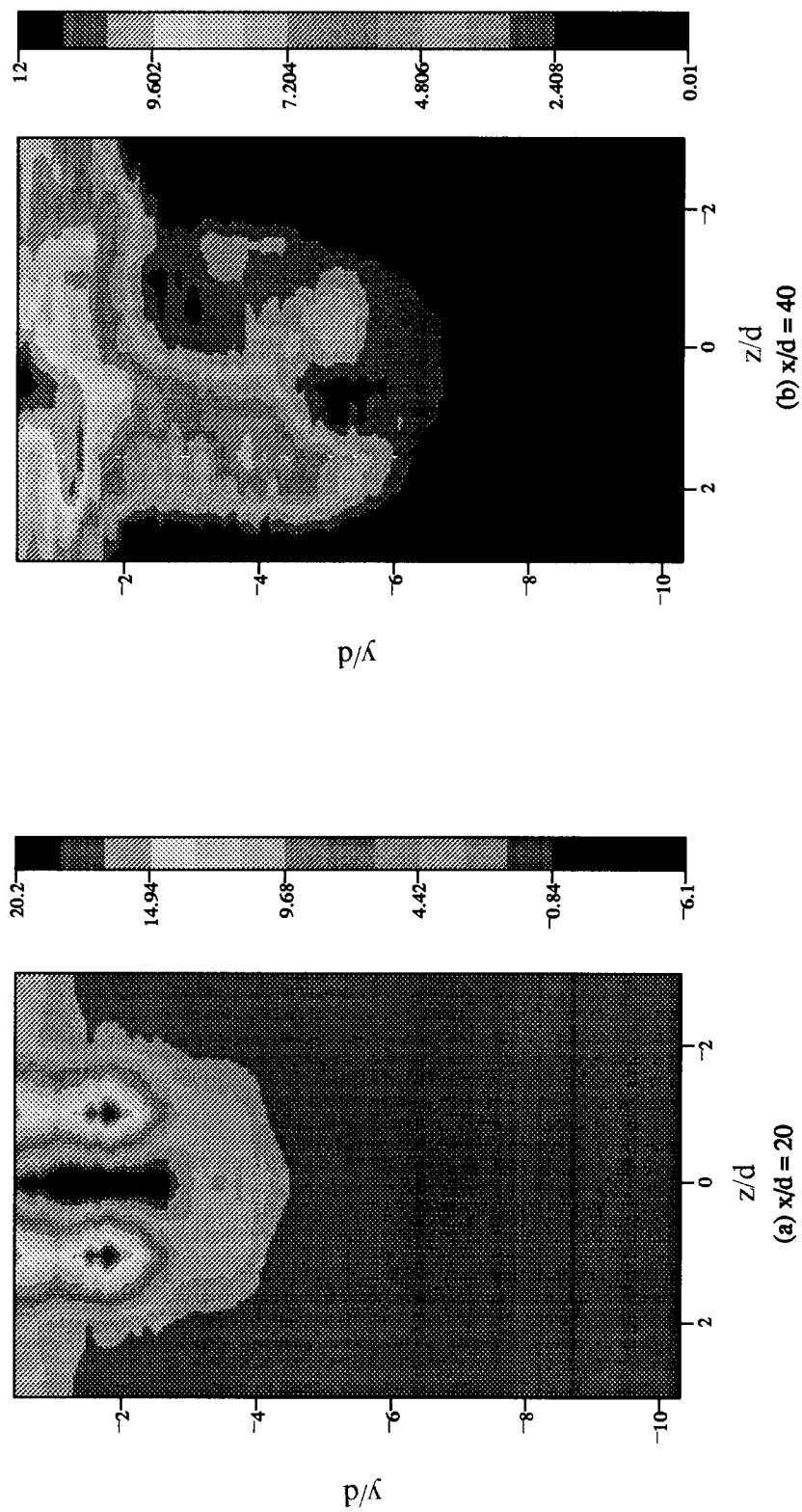FIGURE 5.42: Transformed Shear $[uv(\rho')^2/(\rho u)^2]$ (uv probe) ($\times 10^3$)
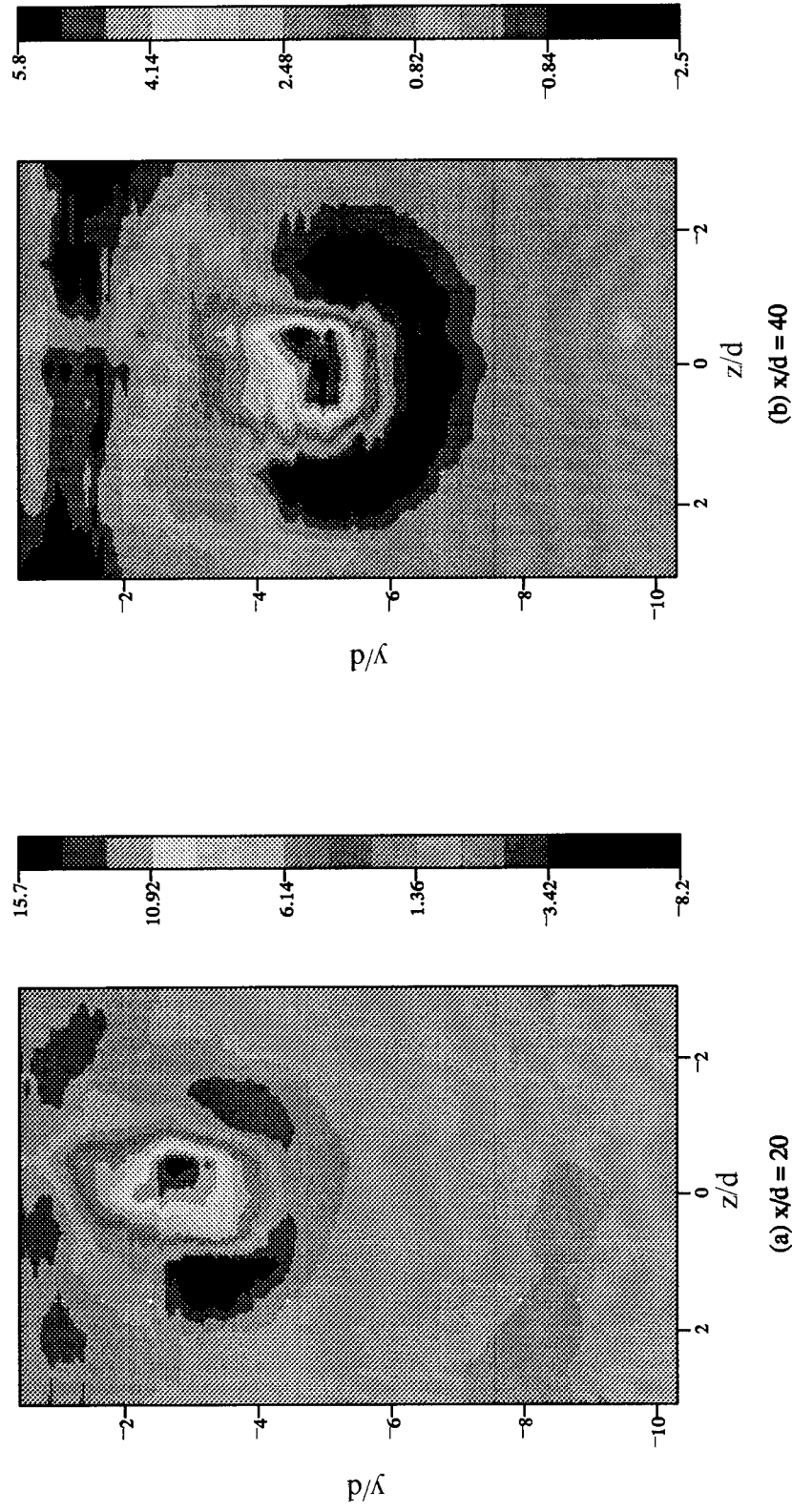
FIGURE 5.43: Transformed Shear [cross-wire shear] (uv probe) (x10³)

80
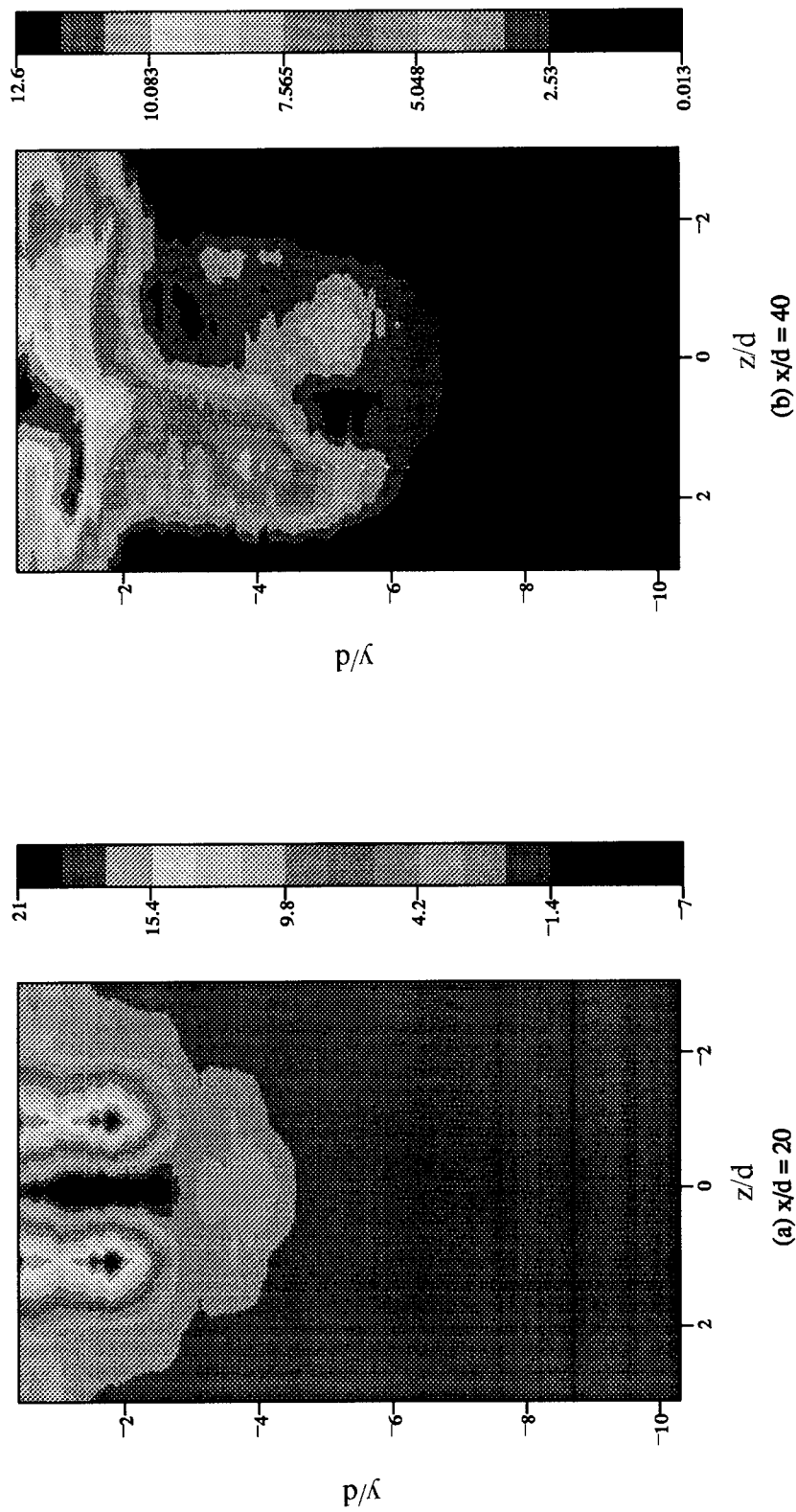
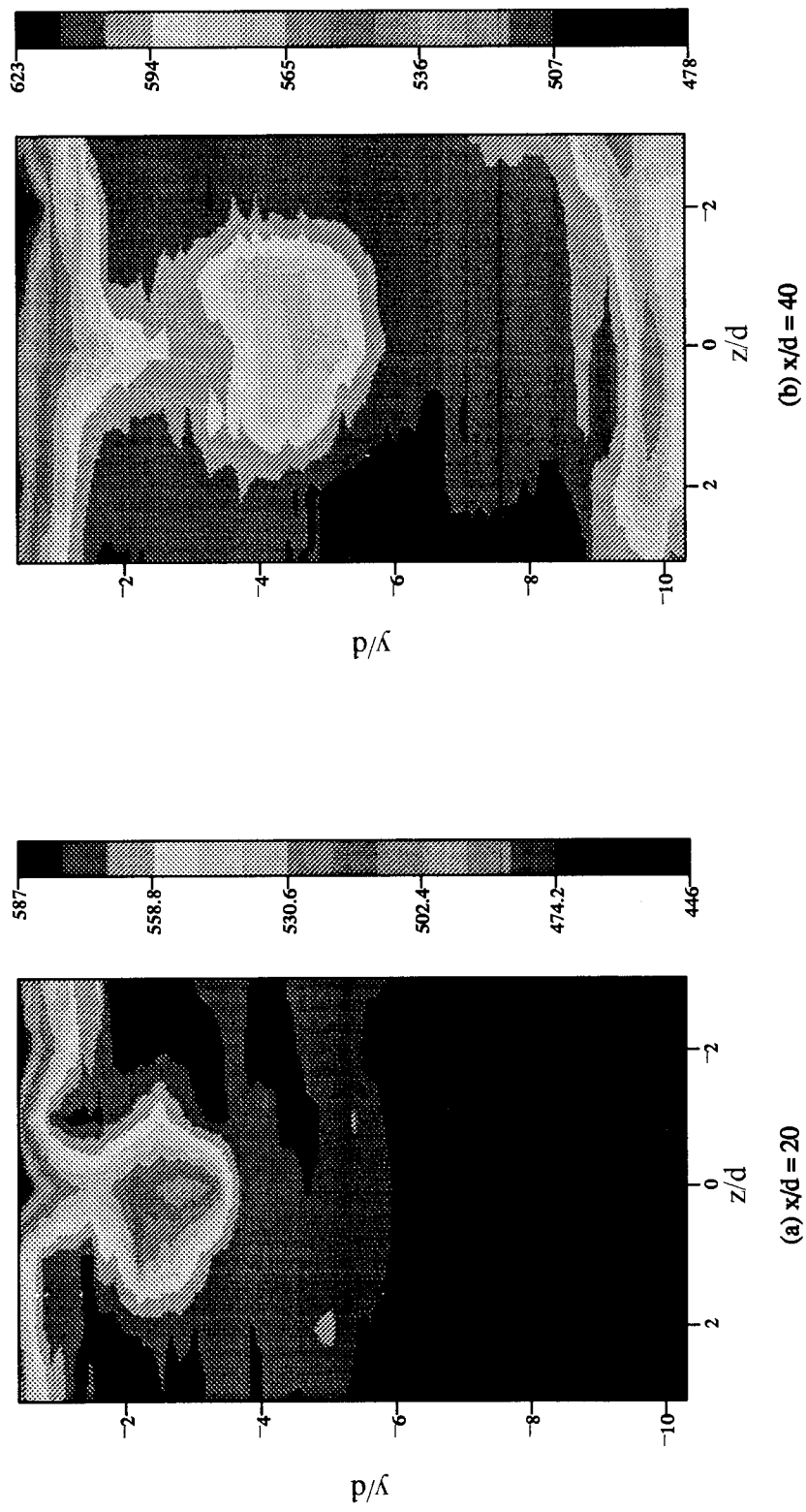FIGURE 5.44: Transformed Shear $[(\rho u)'(\rho w)'/(\rho u)^2]$ (uw probe) $(\times 10^3)$

81
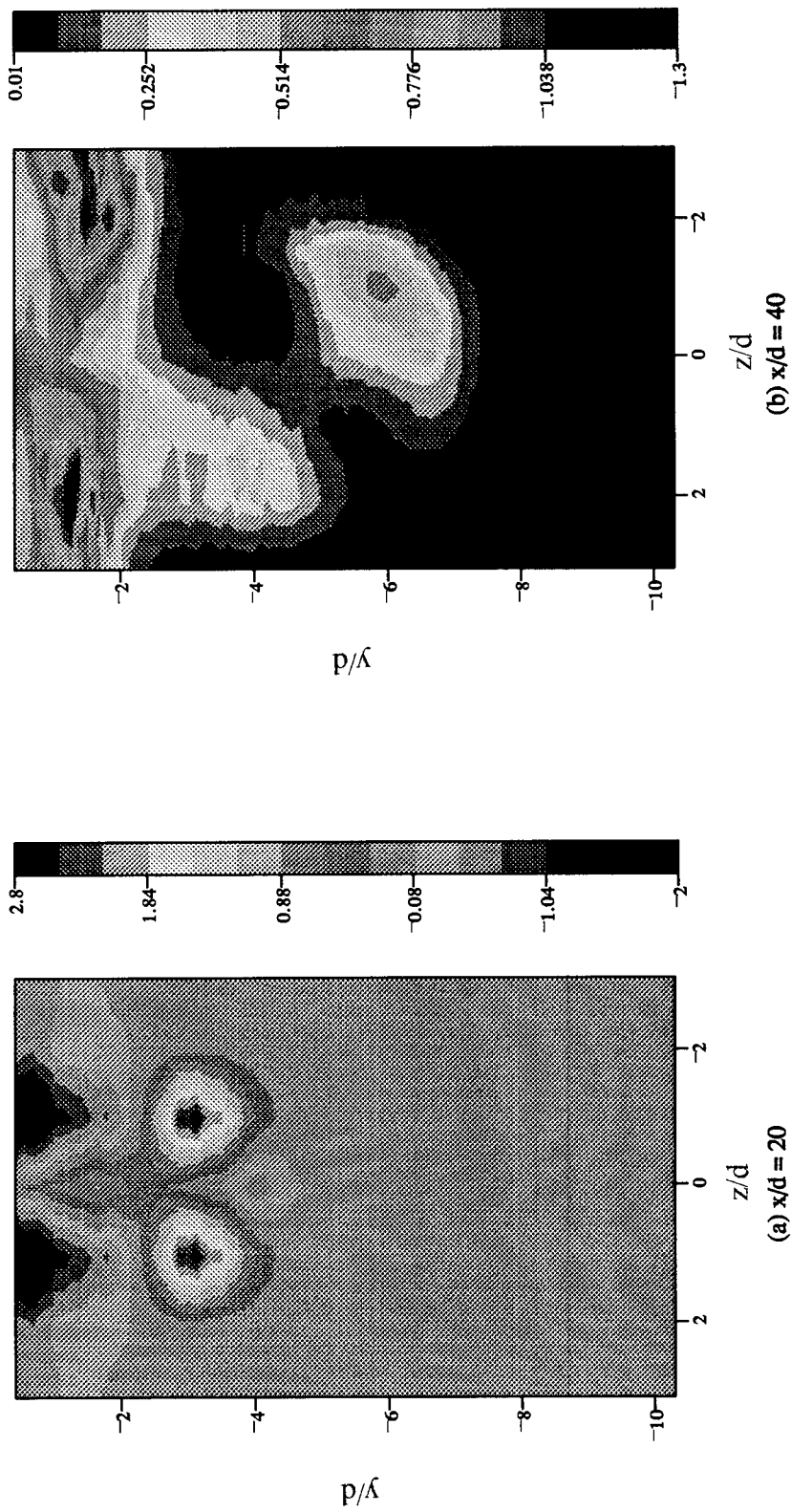
FIGURE 5.45: Transformed Shear $[uw(\rho')^2/(\rho u)^2]$ (uw probe) $(\times 10^3)$

FIGURE 5.46: Transformed Shear [cross-wire shear] (uw probe) (×10³)
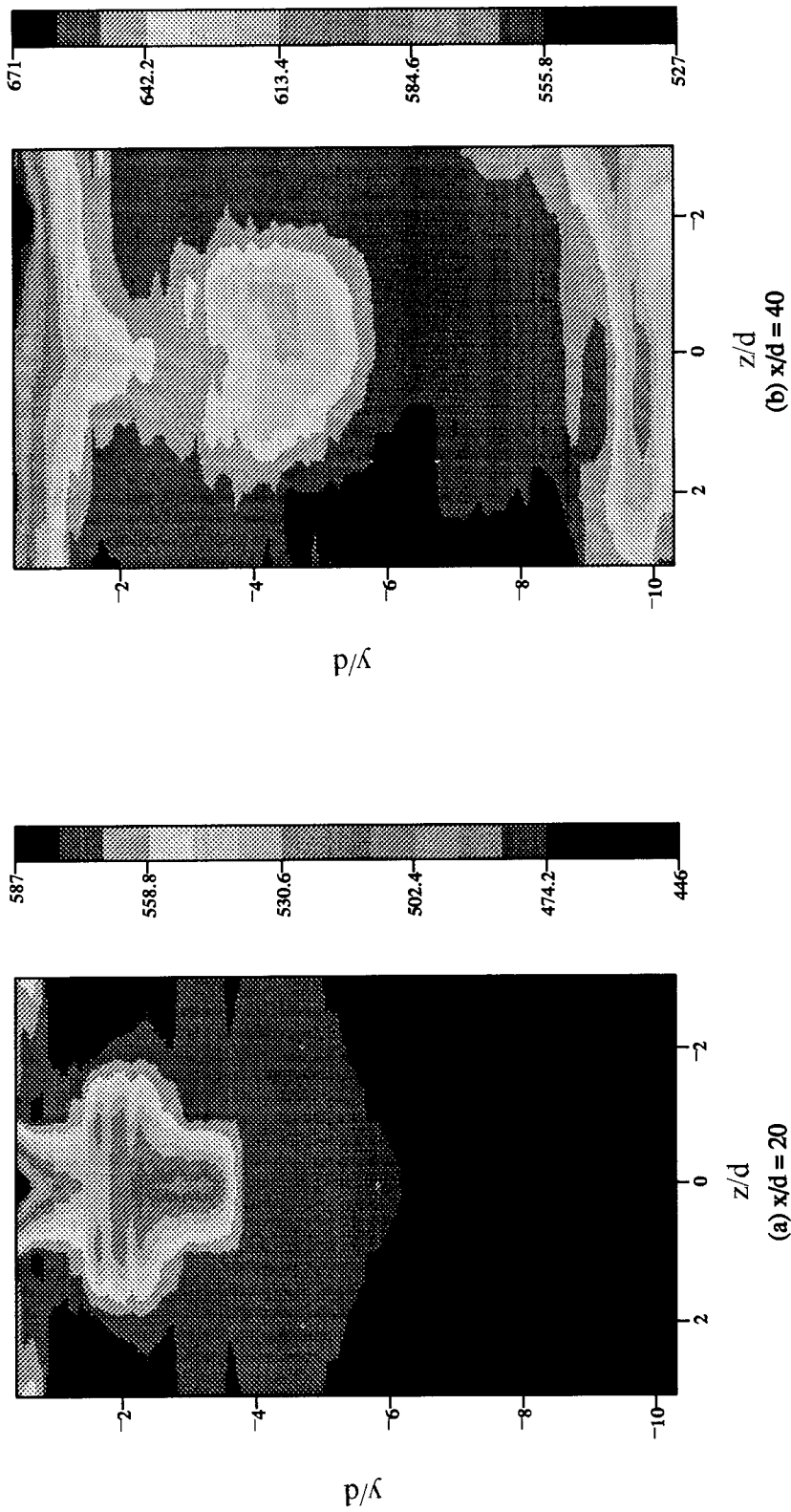
83

FIGURE 5.47: Mean Velocity [U (m/s)] (uv probe)
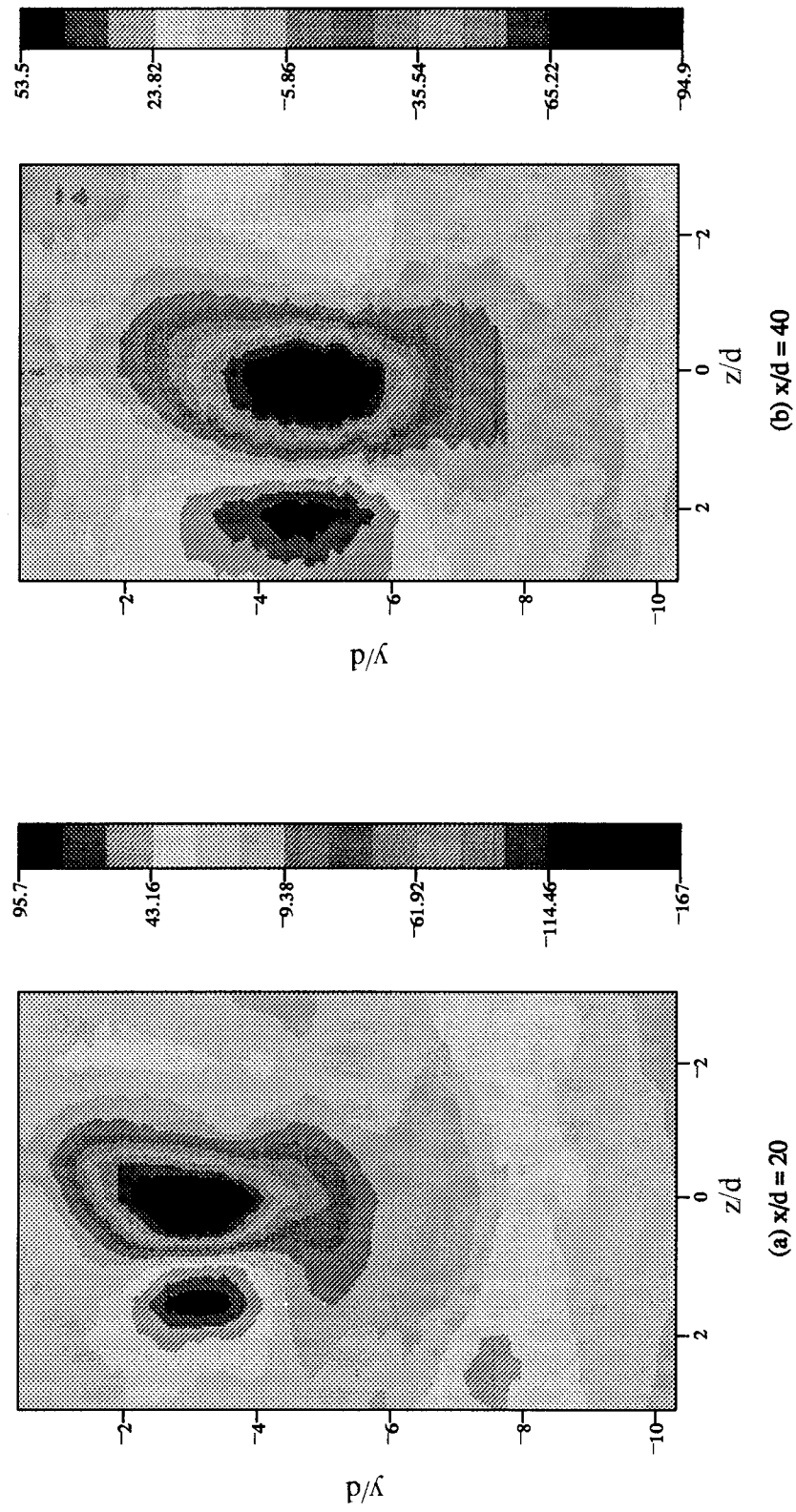
84

FIGURE 5.48: Mean Velocity [U (m/s)] (uw probe)
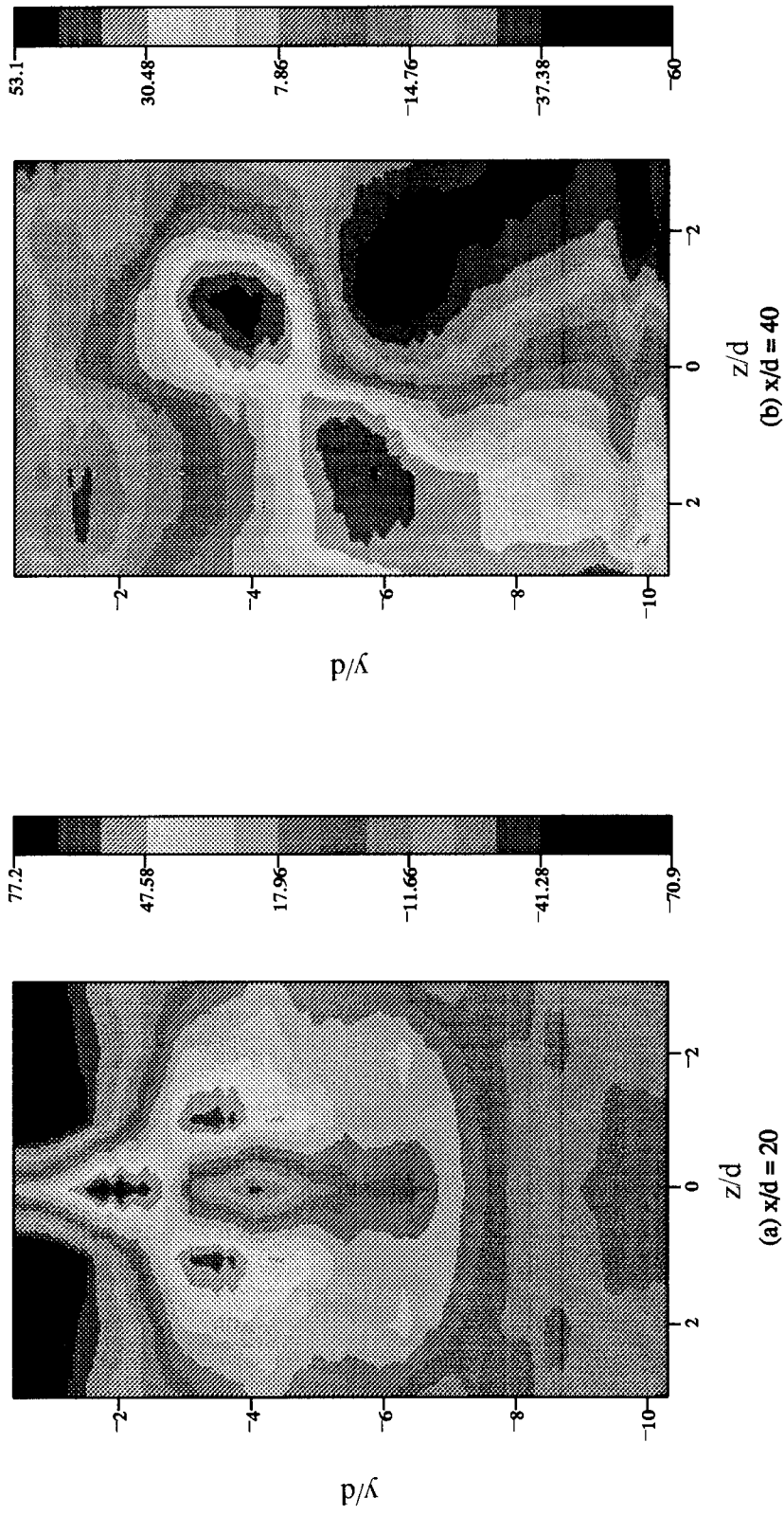
85

FIGURE 5.49: Mean Velocity [V (m/s)] (uv probe)

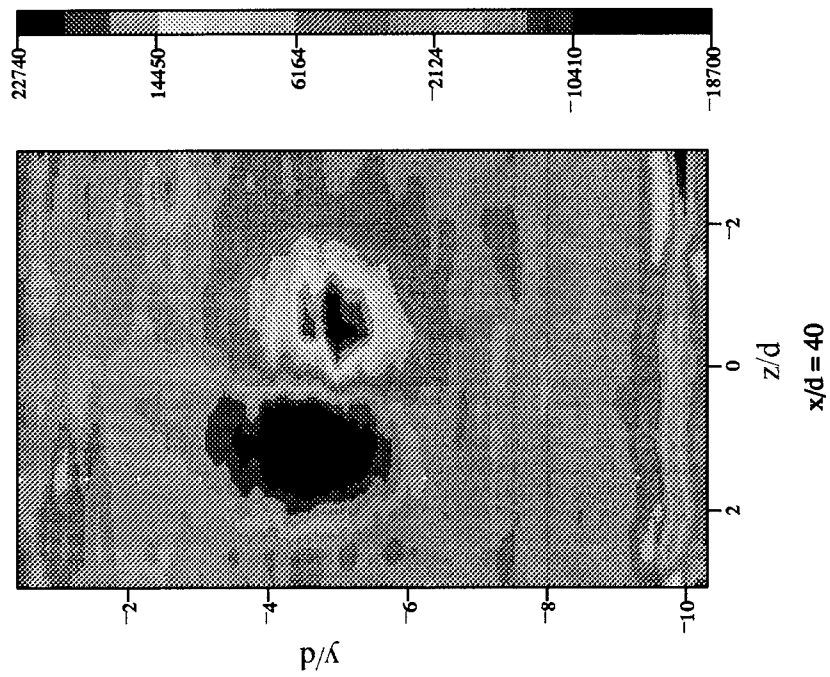FIGURE 5.50: Mean Velocity [W (m/s)] (uw probe)
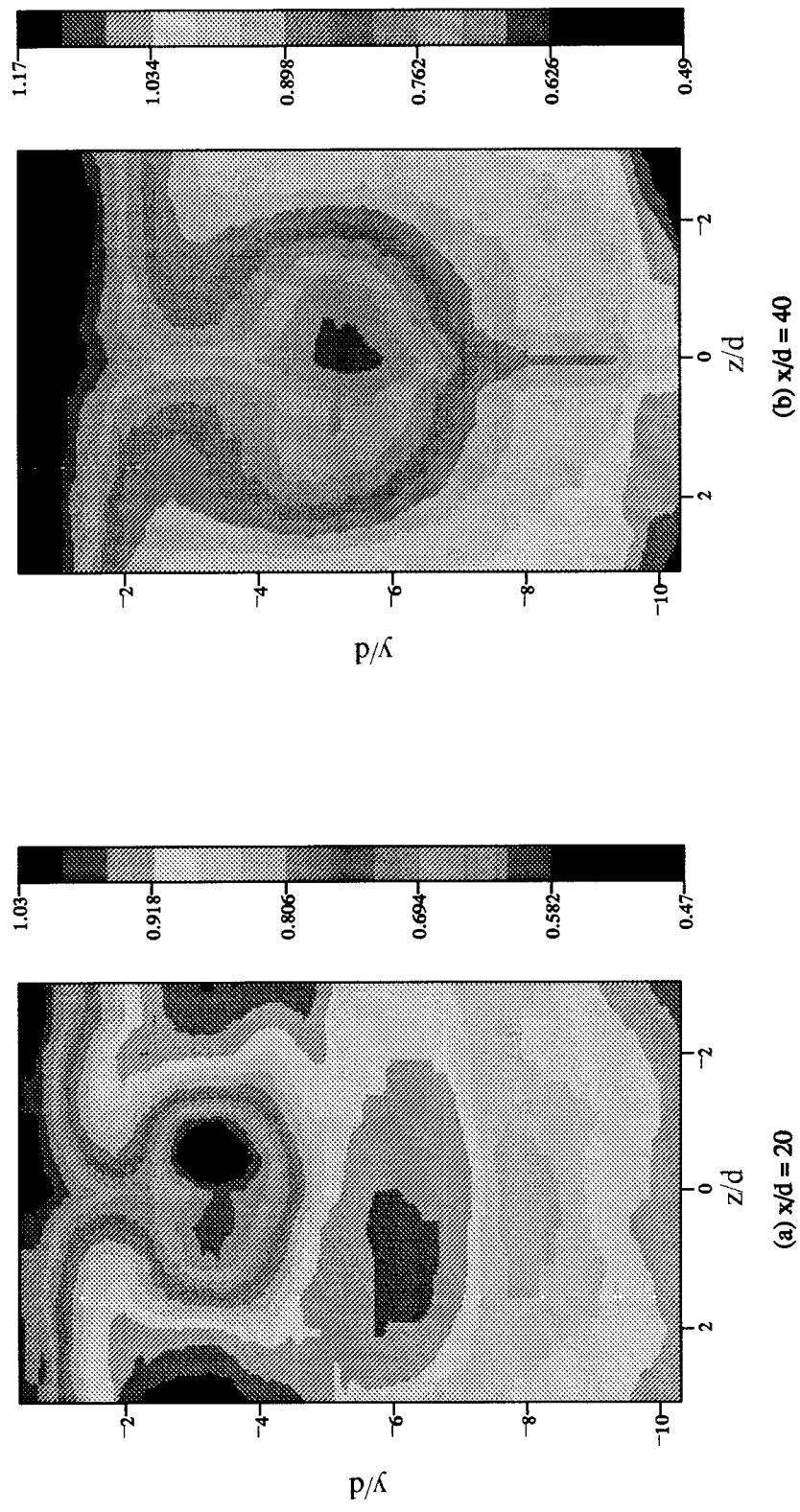
FIGURE 5.51: Vorticity (ω_x) (rad/sec)

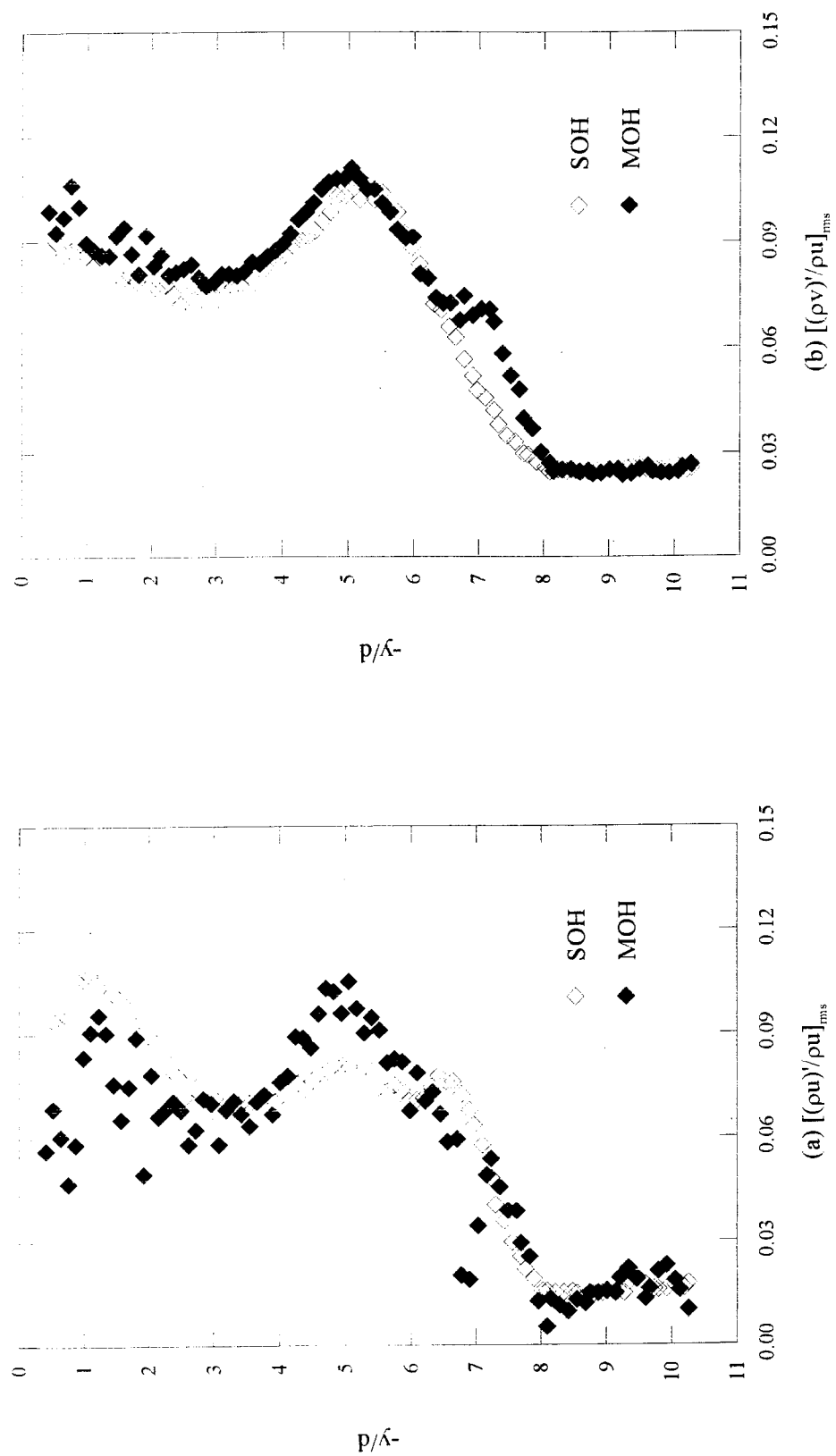FIGURE 5.52: Mean Mass Flux $[(\rho u)/(\rho u)_\infty]$ (uv probe)

FIGURE 5.53: Turbulence Intensity (uv probe)
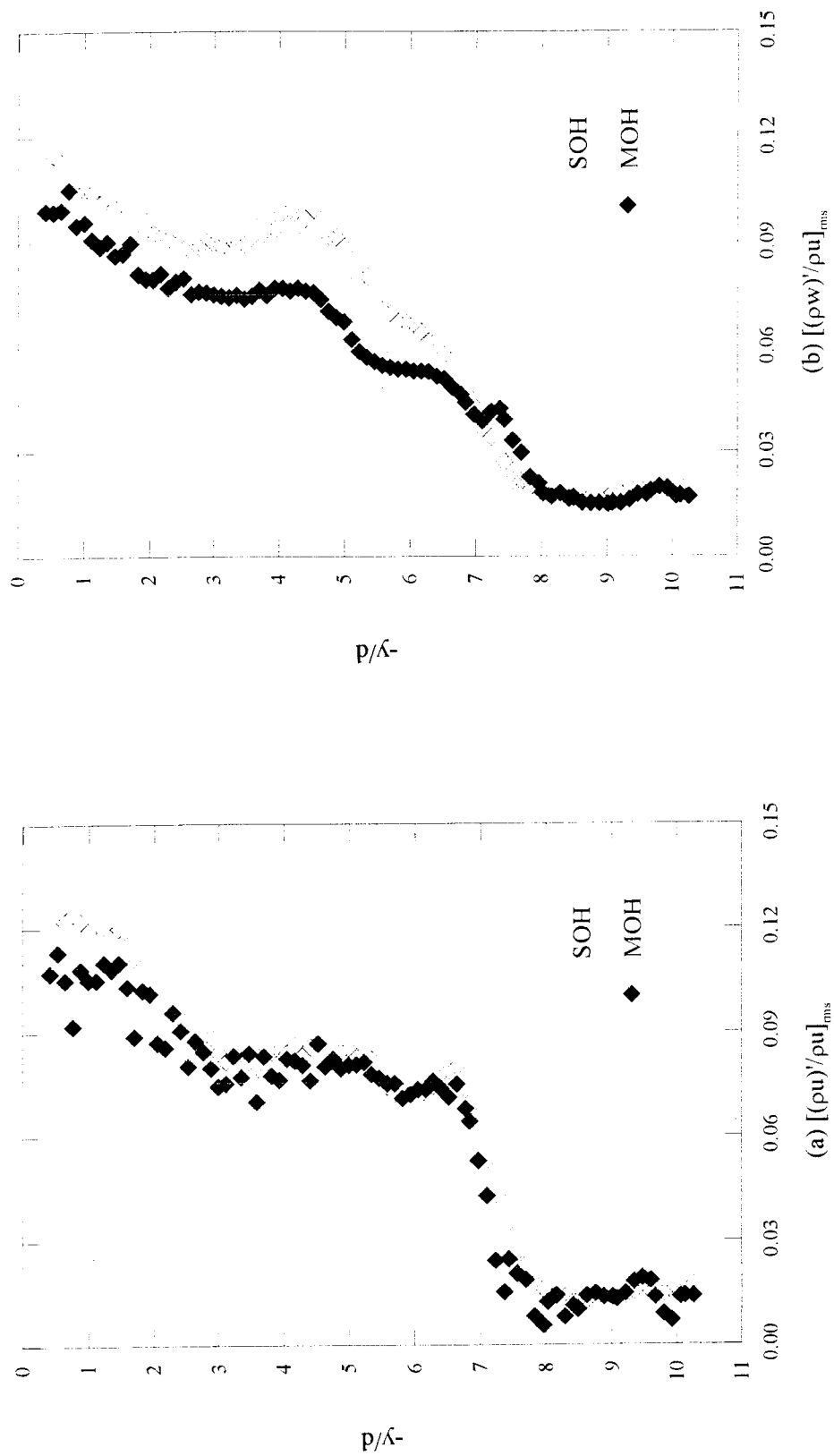
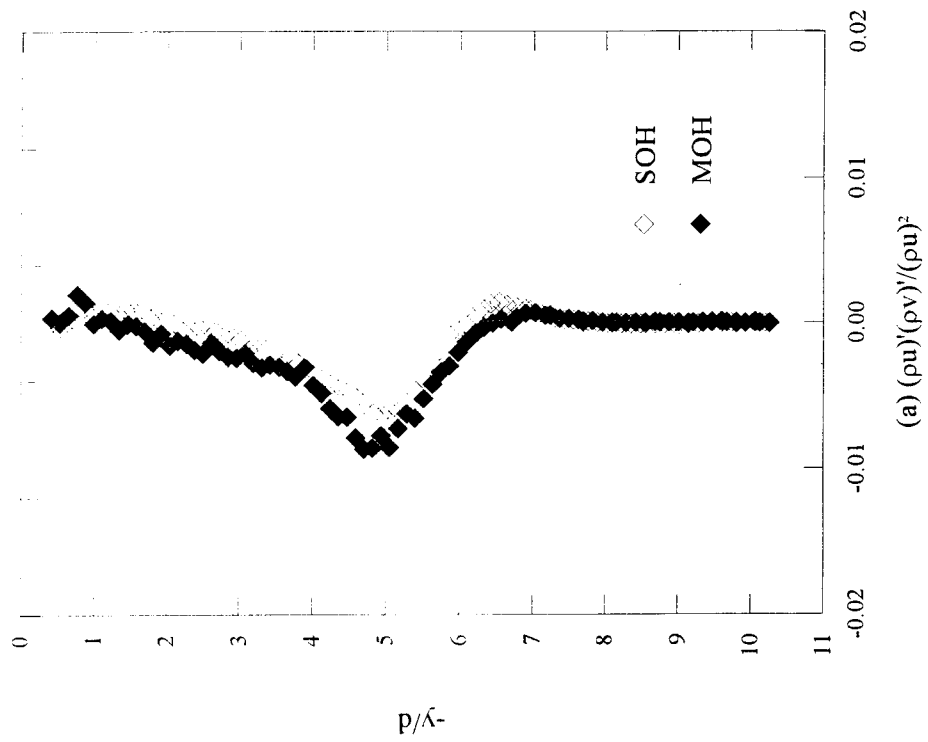FIGURE 5.54: Turbulence Intensity (uw probe)
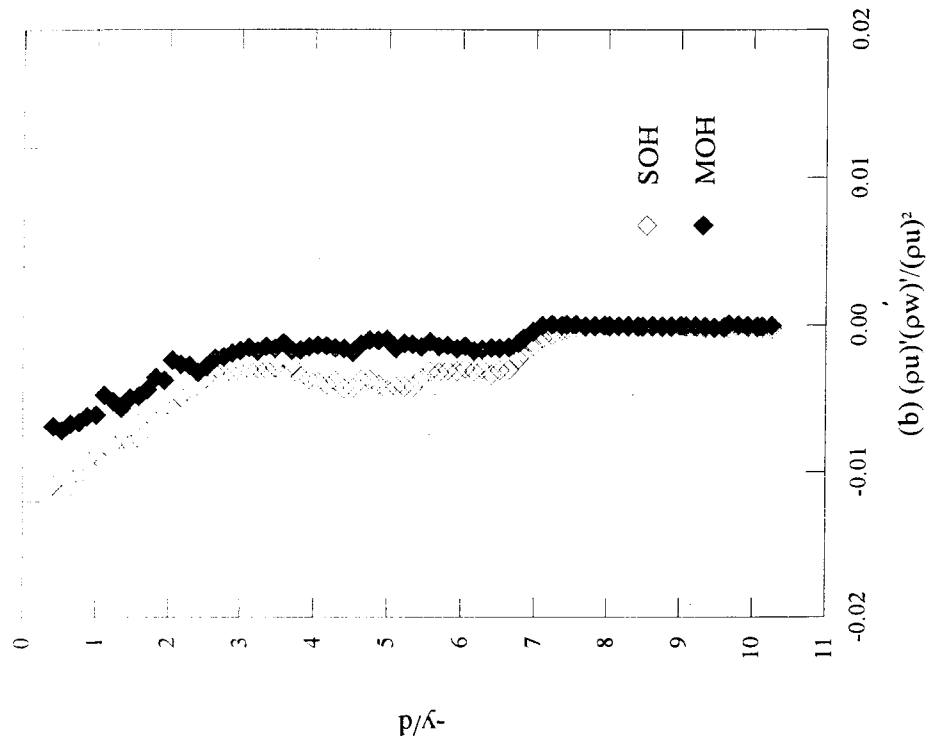
FIGURE 5.55: Shear
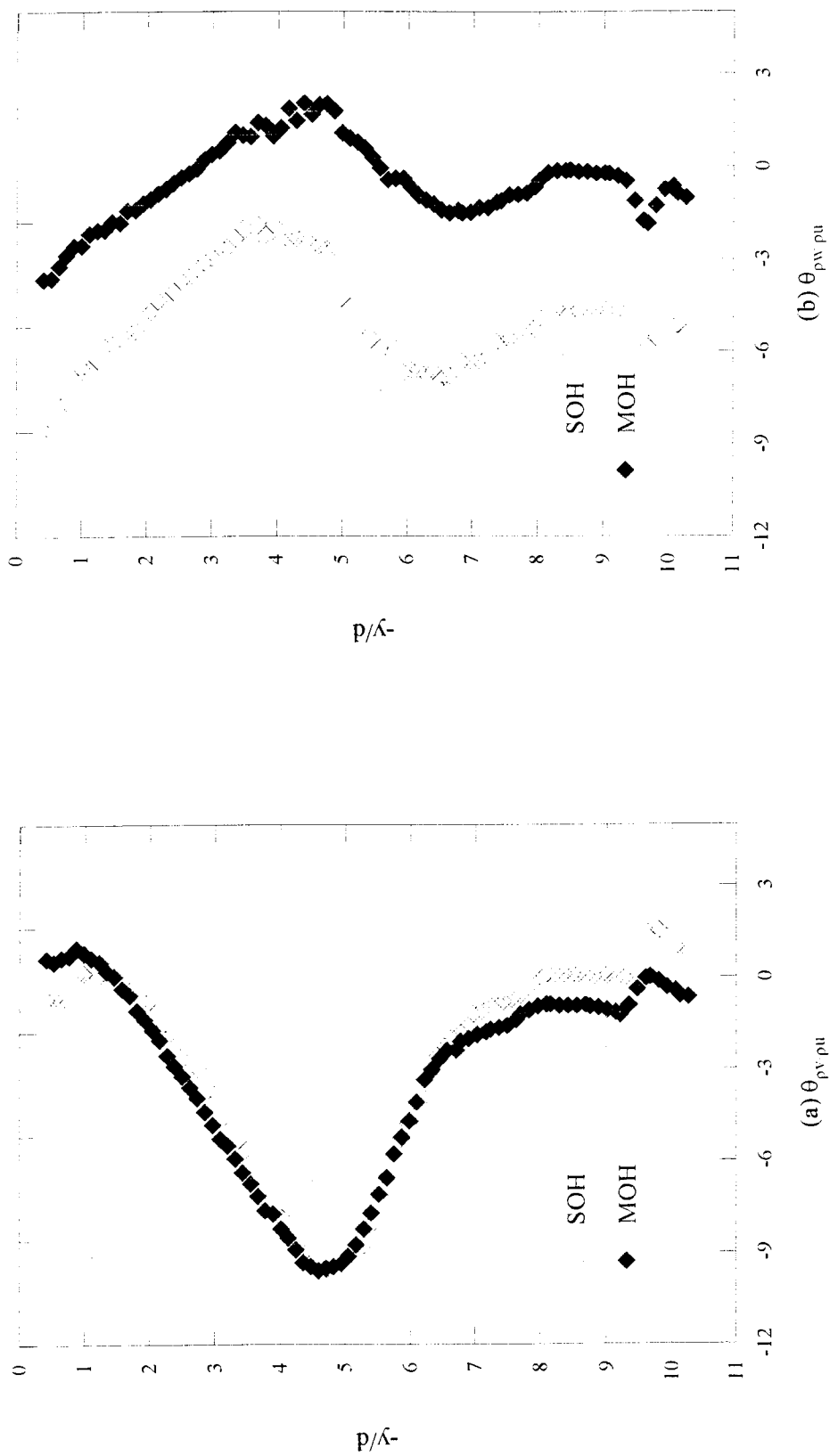
FIGURE 5.56: Flow Angle (θ)
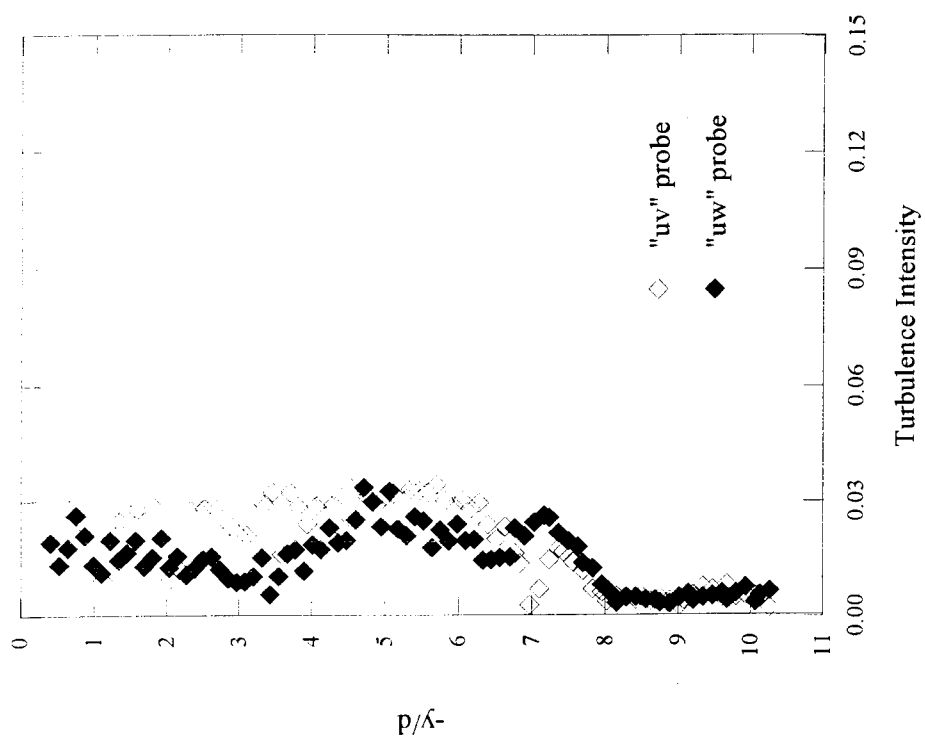
FIGURE 5.57: Turbulence Intensity $[T_t '/T_t]_{rms}$
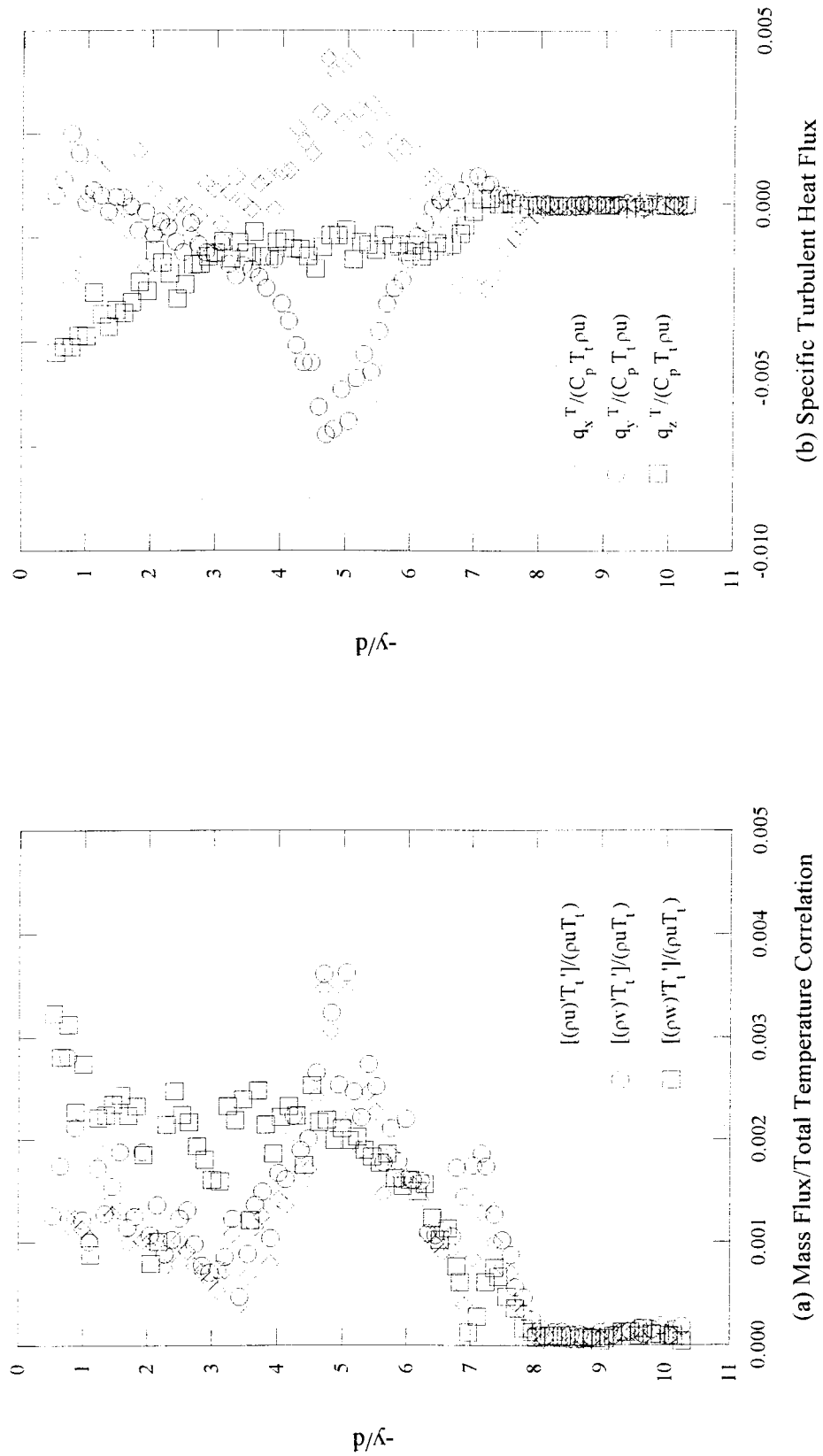
FIGURE 5.58: Mass Flux/Total Temperature and Specific Turbulent Heat Flux
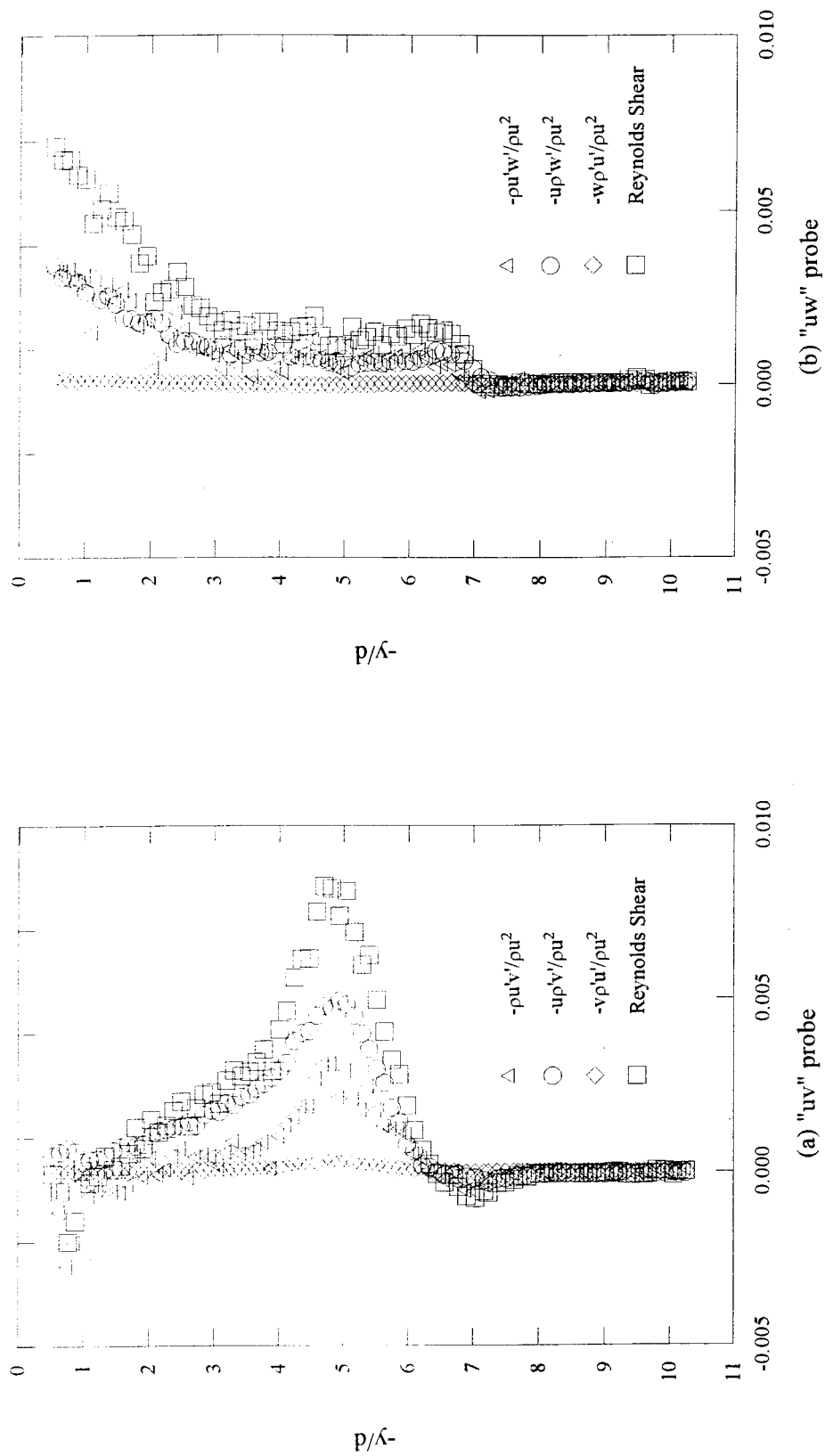
FIGURE 5.59: Reynolds Shear Stress

(b) Favre shear

$(\rho u''v'')/(\rho u^2)$
$(\rho u''w'')/(\rho u^2)$

(a) Favre terms

u''/U
v''/U
w''/U
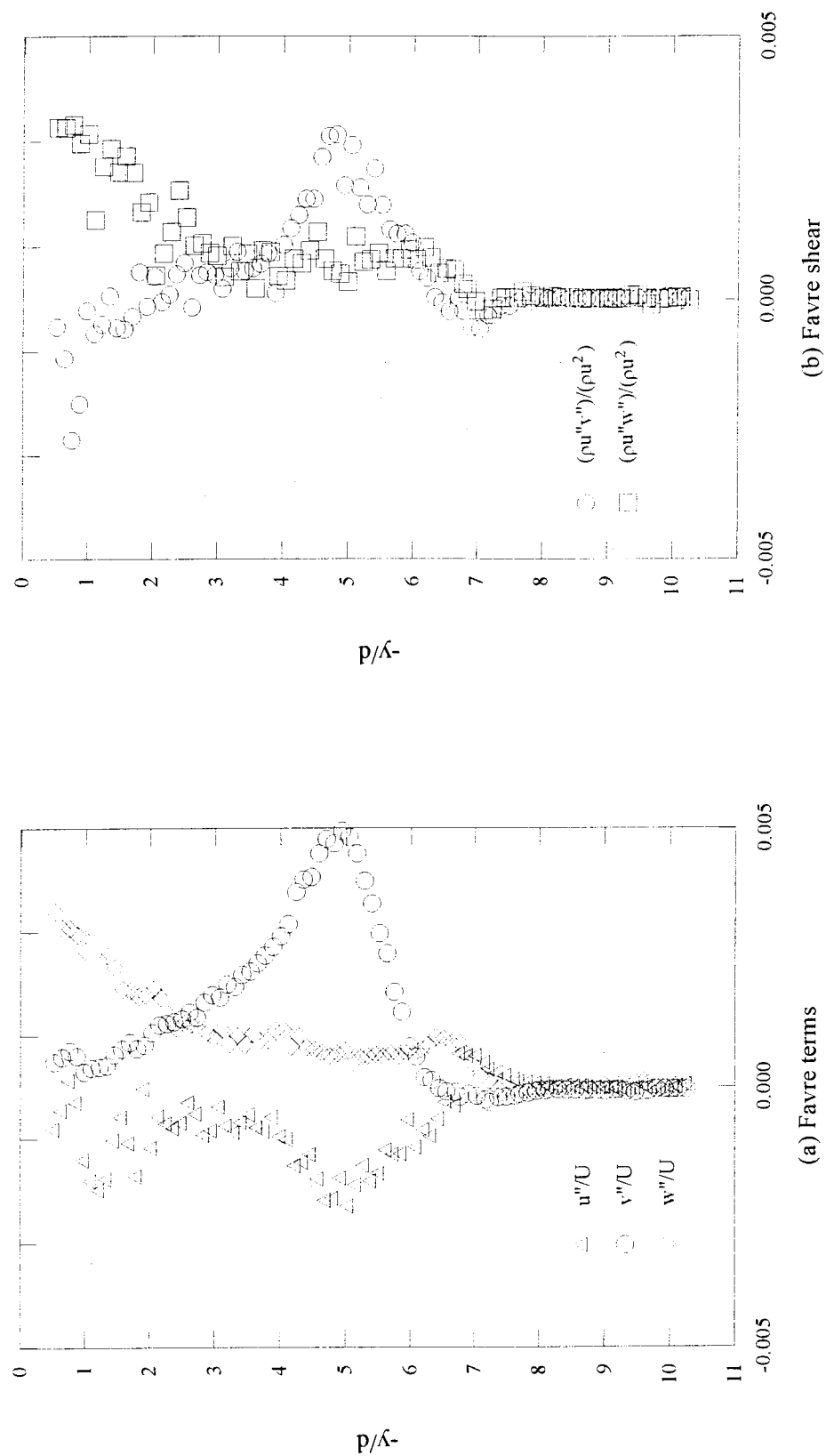
FIGURE 5.60: Favre Variable Data

97
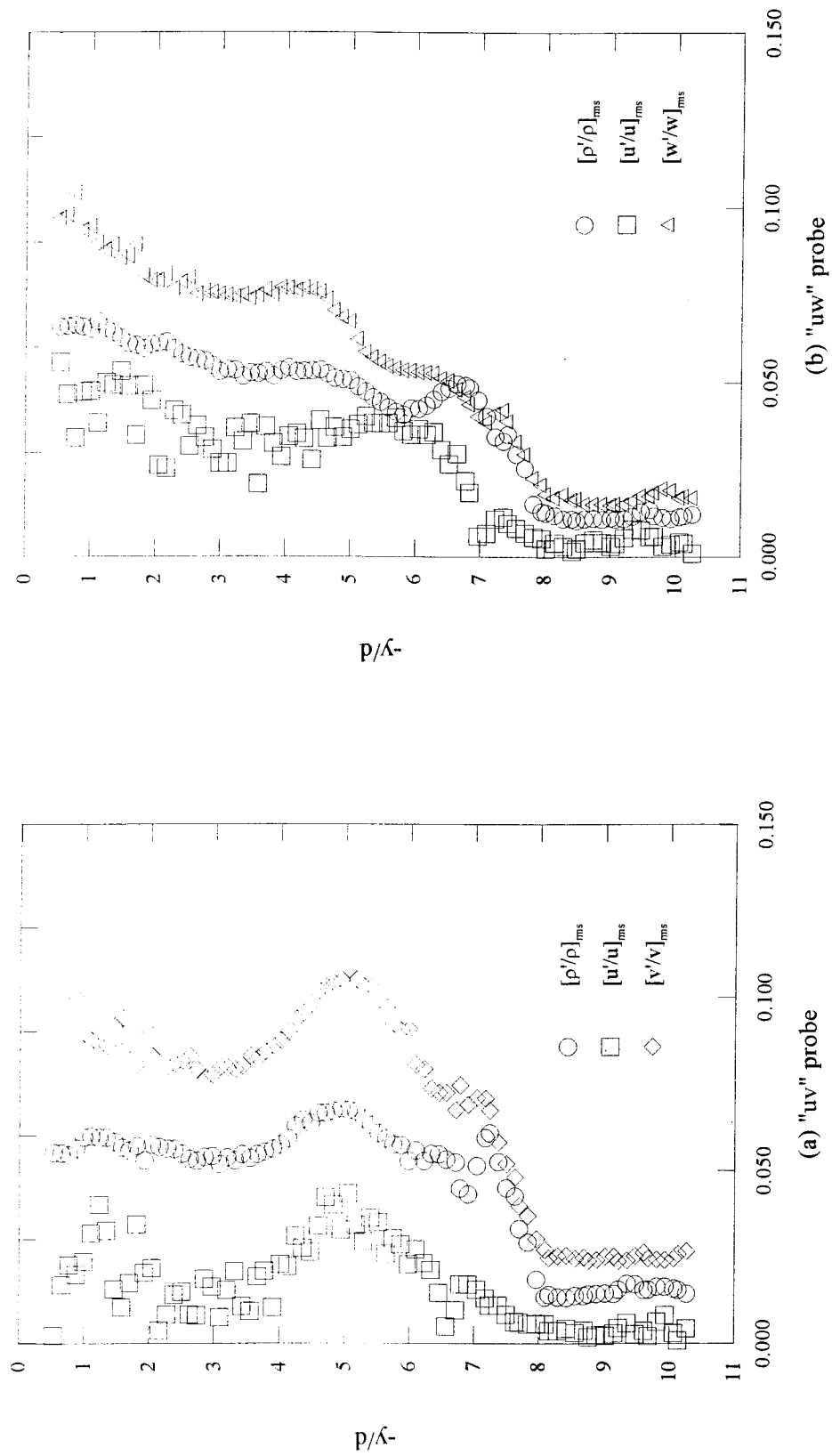
FIGURE 5.61: Separated Turbulence Intensities

(b) Density-velocity correlations

(a) Velocity-velocity correlations

FIGURE 5.62: Velocity-Velocity and Density-Velocity Correlations

VI. Conclusions and Recommendations

6.1 Conclusions

Mean flow data and flow visualization provided insight into mean flow structure and guidance to reduce the extent to which the flowfield was measured with hot-wire probes.

Single overheat anemometry across the flowfield at each station revealed turbulence intensity and turbulent kinetic energy to be better estimates of jet core penetration and jet size than mean flo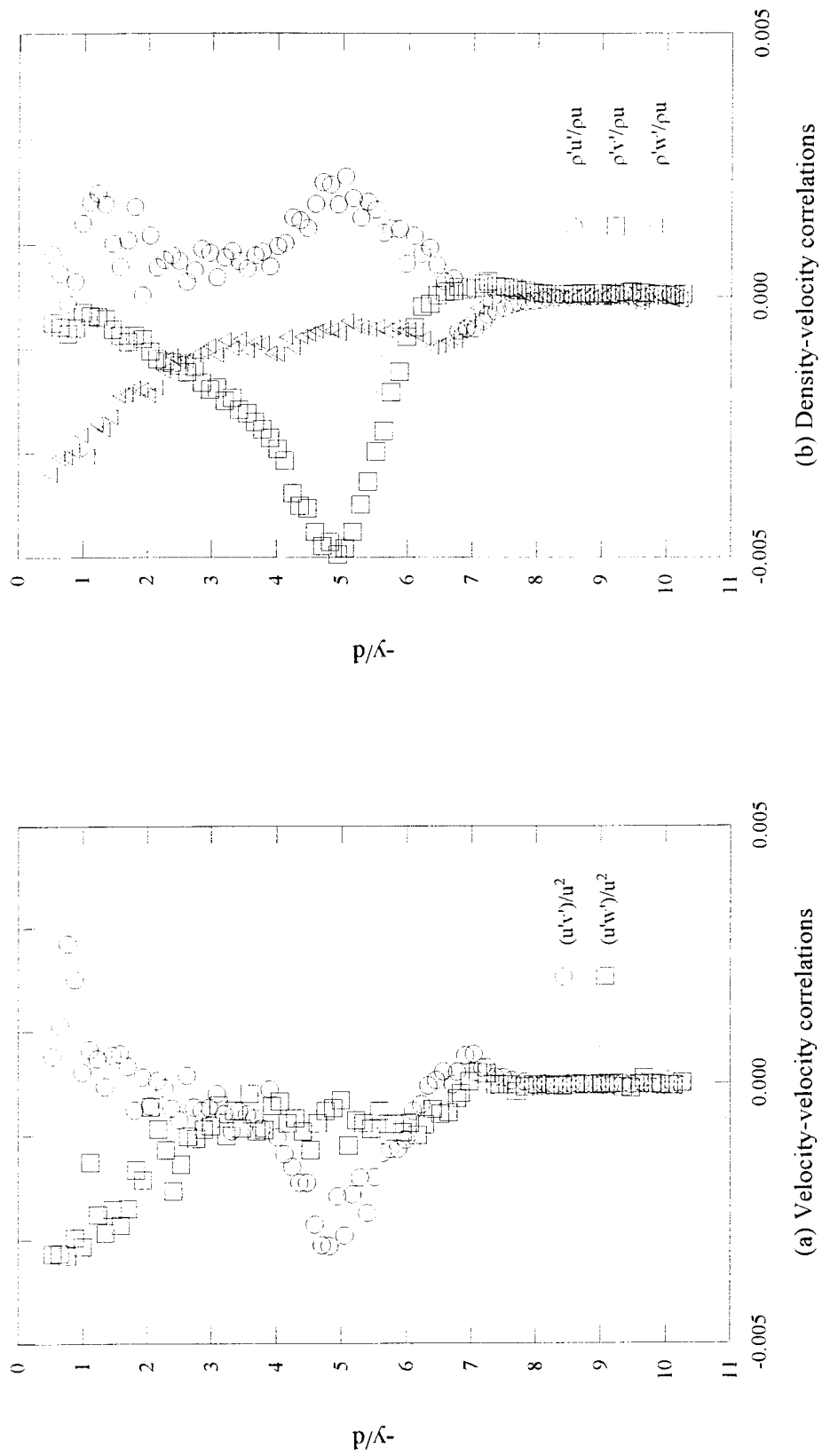w data alone. The single overheat data also confirmed the role compressibility plays in the Reynolds shear in boundary layer and free mixing layer flows. This study determined compressibility to account for approximately 67% of the Reynolds shear stress.

In particular, the data indicate the last two terms of Eqn. (2.14), repeated as Eqn.(6.1), to be insignificant. The second term is very significant, however, and is frequently neglected in turbulence models. It is the second term which comprises virtually all the compressible portion of the total Reynolds shear stress.

$$\tau_{ij}^{T} = -\bar{\rho}\,\overline{u_i'\,u_j'} - \bar{u}_i\,\overline{\rho'\,u_j'} - \bar{u}_j\,\overline{\rho'\,u_i'} - \overline{\rho'\,u_i'\,u_j'} \tag{6.1}$$

The relative importance of the third term, and to a much lesser extent the fourth, is based somewhat on injector parameters. Steeper injection angles or higher injection velocities will increase both terms.

The multiple overheat data validates the $T_t' = 0$ assumption made in the present work. It also indicates the single overheat data to be accurate within approximately 3% of the multiple overheat data. For flowfields with small total temperature fluctuations, single overheat data provides excellent accuracy (within 3%).

6.2 Recommendations for Further Study

The importance of compressible turbulence in supersonic injection cannot be overemphasized. More detailed multiple overheat analysis is needed. In fact, it may be

100

possible to devise a correlation between single and multiple overheat hot-wire data to extend the usefulness of the single overheat method.

Innumerable, useful investigations can be undertaken with the AFIT Mach 3 wind tunnel and low angle injection model. Heated injectant can be used to determine the effect of differences in total temperature on turbulence and mixing (this work is underway as of this writing). Low molecular weight injectants can be used to simulate injection in a hydrogen-fueled SCRAMjet engine. High molecular weight injectant can simulate the conditions found in a chemical oxygen-iodine laser (currently under development at Phillips Lab in Albuquerque, NM).

Better investigative techniques can be used. Seeded flows with laser doppler velocimetry (LDV) may yield new insights. Use of triple-wire probes can reduce tunnel time and increase fidelity of the flow components. In particular, the triple-wire would enable the measurement of the one element of the shear stress tensor not measured here (τ_{yz}^T).

$$
\tau^T = \begin{bmatrix} \tau_{xx}^T & \tau_{xy}^T & \tau_{xz}^T \\ \tau_{yx}^T & \tau_{yy}^T & \tau_{yz}^T \\ \tau_{zx}^T & \tau_{zy}^T & \tau_{zz}^T \end{bmatrix}
\tag{6.2}
$$

Tunnel run time can be increased by addition of extra vacuum tanks. While doubling the vacuum storage would double the mean time between tunnel runs, the useful tunnel time would more than double because the fixed costs of starting the tunnel, allowing it to settle, and triggering the DAS would only have to be paid once.

Finally, to enhance further study and applicability of future data, the shock structure must be more fully understood. This can be accomplished by LDV, vertical schlieren or shadowgraph photography, or by traversing the mean flow probes in horizontal, instead of vertical, sections.

Bibliography

1. Wittliff, C. E., "A Survey of Existing Hypersonic Ground Test Facilities - North America."

2. Anderson, D. A., Tannehill, J. C., and Pletcher, R. H., *Computational Fluid Mechanics and Heat Transfer*, McGraw-Hill, New York, 1984.

3. Wilcox, D. C. *Turbulent Modeling for CFD*, DCW Inc., La Canada, CA, 1993.

4. Settles, G. S., and Dobson, L. J., "Supersonic and Hypersonic Shock/Boundary-Layer Interaction Database," *AIAA Journal*, Vol. 32, No. 7, July 1994.

5. Liou, W. W., and Shih, T. H., "Oh the Basic Equations for the Second-Order Modeling of Compressible Turbulence," NASA TM 105277, October 1991.

6. Bowersox, R. D. W., "Compressible Turbulence in a High-Speed High-Reynolds Number Mixing Layer," PhD Dissertation, Virginia Polytechnic Institute and State University, VA, Department of Aerospace Engineering, September 1992.

7. Fuller, E. J., Mays, R. B., Thomas, R. H., and Schetz, J. A. "Mixing Studies of Helium in Air at High Supersonic Speeds," *AIAA Journal*, Vol. 30, No. 9, September 1992, pp. 2234-2243.

8. Mays, R. B., Thomas, R. H., and Schetz, J. A. "Low Angle Injection Into a Supersonic Flow," AIAA-89-2461.

9. Fuller, E.J., Thomas, R.H., and Schetz, J.A., "Effects of Yaw on Low Angle Injection into a Supersonic Flow," AIAA-91-0014.

10. Shapiro, A. H., *The Dynamics and Thermodynamics of Compressible Flow, Volume II*, Krieger Publishing Company, Malabar, Florida, 1954.

11. Schetz, J. A., *Foundations of Boundary Layer Theory for Momentum, Heat Transfer, and Mass Transfer*, Englewood Cliffs, NJ, 1984.

12. Bowersox, R. D. W., and Schetz, J. A., "Compressible Turbulence Measurements in a High-Speed High-Reynolds-Number Mixing Layer," *AIAA Journal*, Vol. 32, No. 4, pp. 758-764, April 1994.

13. Schetz, J. A., and Billig, F. S., "Penetration of Gaseous Jets Injected into a Supersonic Stream," *Journal of Spacecraft and Rockets*, Vol. 3, No. 11, November 1966, pp. 1658-1665.

14. Billig, F. S., Orth, R. C., and Lasky, M., "A Unified Analysis of Gaseous Jet Penetration," *AIAA Journal*, Vol. 9, No. 6, June 1971, pp. 1048-1058.

15. Schetz, J. A., Hawkins, P. F., and Lehman, H., "Structure of Highly Underexpanded Transverse Jets in a Supersonic Stream," *AIAA Journal*, Vol. 5, No. 5, May 1967, pp. 882-884.

16. Schetz, J. A., Weinraub, R. A., and Mahaffey, Jr., R. E., "Supersonic Transverse Injection into a Supersonic Stream," *AIAA Journal*, Vol. 6, No. 5, May 1968, pp. 933-934.

17. Mays, R. B., Thomas, R. H., and Schetz, J. A., "Low Angle Injection into a Supersonic Flow," AIAA-89-2461, 1989.

18. Fuller, E. J., Thomas, R. H., and Schetz, J. A., "Effects of Yaw on Low Angle Injection into a Supersonic Flow," AIAA-91-0014, 1990.

19. NACA Report 1135, "Equations, Tables, and Charts for Compressible Flow," Ames Research Staff, 1953.

20. *Nicolet Systems Operation*, Nicolet, Madison, WI, 1991.

21. Volluz, R. J., *Handbook of Supersonic Aerodynamics*, Section 20, "Wind tunnel Instrumentation and Operations," NAVORD Report 1988, Vol. 6, 1961.

22. "Hot-Wire/Hot-Film Anemometry," TSI Incorporated, St. Paul, MN, 1988.

23. Kovaszney, L. S. G., "The Hot-Wire Anemometer in Supersonic Flow," *Journal of Aeronautical Science*, Vol. 17, 1950, pp. 565-584.

24. Bowersox, R. D. W., "Thermal Anemometry," in *Handbook of Fluid Dynamics* (Schetz, J. A., and Fuhs, W., eds.), John Wiley & Sons, 1995.

25. Bowersox, R. D. W., "MSHeAR User's Manual," Department of Aeronautics, Air Force Institute of Technology, Wright-Patterson AFB, Ohio, 1994.

26. Kistler, A., "Fluctuation Measurements in a Supersonic Turbulent Boundary Layer," *Physics of Fluids*, 2, 220, 1959.

27. Burden, R. L. and Faires, J. D., *Numerical Analysis*, 5th Ed., PWS Publishing Company, Boston, 1993.

Vita

Gregory Joseph McCann was born April 24, 1968 in Washington, D.C. to Walter P. and Maida A. McCann. He graduated from the Brookstone School in Columbus, Georgia in June 1986. Attending the Georgia Institute of Technology from September 1986 to September 1990, he graduated with honor with a Bachelor of Aerospace Engineering. He began his studies at the Air Force Institute of Technology in September 1992 on a part-time basis and completed his Master's degree in March 1995.

1. AGENCY USE ONLY (Leave blank)	2. REPORT DATE March 1995	3. REPORT TYPE AND DATES COVERED Master's Thesis

4. TITLE AND SUBTITLE

COMPRESSIBLE TURBULENCE MEASUREMENT IN LOW-ANGLE INJECTION INTO A SUPERSONIC FLOW

5. FUNDING NUMBERS

6. AUTHOR(S)

Gregory J. McCann, Captain, USAF

7. PERFORMING ORGANIZATION NAME(S) AND ADDRESS(ES)

Air Force Institute of Technology, WPAFB, OH 45433

8. PERFORMING ORGANIZATION REPORT NUMBER

AFIT/GAE/ENY/95M-03

9. SPONSORING / MONITORING AGENCY NAME(S) AND ADDRESS(ES)

Dr. A. Najad, WL/POPT
Taitech Inc. (Dr. T. Chen)
    3675 Harmeling Drive, Beavercreek, OH 45440
Mr. Gerald W. Roberts, NAIC/TATD

10. SPONSORING / MONITORING AGENCY REPORT NUMBER

11. SUPPLEMENTARY NOTES

12a. DISTRIBUTION / AVAILABILITY STATEMENT

Approved for public release; distribution unlimited

12b. DISTRIBUTION CODE

13. ABSTRACT (Maximum 200 words)

Mean flow and compressible turbulence measurements have been obtained at two stations downstream of low-angle supersonic injection into a Mach 3.0 flow ($Re/m = 15 \times 10^6$). Data were collected using conventional Pitot and cone-static probes, single and multiple overheat cross-wire anemometry, and flow visualization techniques (shadowgraphs and schlierens). A direct measure of total Reynolds shear stress was accomplished using a turbulence transformation of the Reynolds-averaged Navier-Stokes equations. Results show compressibility effects, indicated by density fluctuations, to be large relative to the velocity fluctuations and on the same order in all three components. Compressibility appears to account for as much as 75% of the total Reynolds shear. The results of the present study suggest turbulent compressibility effects are very important for this class of flows.

14. SUBJECT TERMS

Supersonic injection, Low-angle injection, Reynolds-averaged Navier-stokes equations, Turbulence, Compressible turbulence, Free shear layer

15. NUMBER OF PAGES

118

16. PRICE CODE

17. SECURITY CLASSIFICATION OF REPORT Unclassified	18. SECURITY CLASSIFICATION OF THIS PAGE Unclassified	19. SECURITY CLASSIFICATION OF ABSTRACT Unclassified	20. LIMITATION OF ABSTRACT UL